CORA Cork Open Research Archive
Cartlann Taighde Oscailte Chorcaí

Title	Carbon nanotubes as materials in nanotechnology
Authors	Jones, Sarah L. T.
Publication date	2013
Original Citation	Jones, S. L., 2013. Carbon nanotubes as materials in nanotechnology. PhD Thesis, University College Cork.
Type of publication	Doctoral thesis
Rights	© 2013, Sarah L. Jones - http://creativecommons.org/licenses/by-nc-nd/3.0/
Download date	2026-11-06 18:32:18
Item downloaded from	https://hdl.handle.net/10468/1286



UCC
University College Cork, Ireland
Coláiste na hOllscoile Corcaigh

Carbon Nanotubes as Materials in Nanotechnology

Sarah Louise Jones



NATIONAL UNIVERSITY OF IRELAND, CORK
College of Science, Engineering & Food Science
Department of Chemistry
Tyndall National Institute

Thesis submitted for the degree of Doctor of Philosophy

August 2013

Supervisor: Prof. James C. Greer
Head of Department: Prof. Michael A. Morris

Contents

List of Figures . . . iv
List of Tables . . . vi
Acknowledgements . . . viii
Dissemination . . . ix
Abstract . . . xi

1 Introduction **1**
1.1 Thesis Outline . . . 2

2 Background **4**
2.1 Graphitic Carbon . . . 4
2.2 CNT structure and chirality . . . 5
2.3 CNT electronic properties . . . 7
2.4 Chemical Vapour Deposition CNT Growth . . . 10
2.4.1 The Vapour-Liquid-Solid Mechanism . . . 10
2.4.2 *In situ* Microscopy of CNT Growth . . . 11
2.5 Computational Studies of CNT Growth . . . 13
2.5.1 Classical Molecular Dynamics . . . 13
2.5.2 DFTB and DFT Molecular Dynamics . . . 15
2.5.3 DFT studies . . . 17
2.6 Doped CNTs . . . 19
2.6.1 Substitutional Doping of CNTs . . . 20
2.6.2 Endohedral Doping of CNTs . . . 22
2.7 Defects in CNTs . . . 24
2.8 CNT-Metal Contacts . . . 26
2.9 Motivation for this Work . . . 30
2.10 References . . . 32

3 Computational Methods **43**
3.1 The Schrödinger Equation . . . 43
3.2 The Born-Oppenheimer Approximation . . . 44
3.3 Geometry Optimisation Techinques . . . 45
3.4 The Variational Principle . . . 48
3.5 Density Functional Theory . . . 48
3.5.1 Hohenberg-Kohn Theorems . . . 49
3.5.2 The Kohn-Sham Approach . . . 50
3.5.3 Approximations to E_{xc} . . . 52
3.6 Basis Sets . . . 54
3.6.1 Plane Waves . . . 54
3.6.2 Localised orbitals . . . 55
3.7 Pseudopotentials and PAW . . . 57
3.8 Electron Localisation Function . . . 58
3.9 Non-Equilbrium Green's Function Method . . . 60
3.10 References . . . 63

4 Nitrogen Doped Carbon Nanotube Growth Mechanism 65
4.1 Introduction . . . 65
4.2 Methods . . . 67
4.3 Simulated Structures . . . 68
4.4 Binding Energies . . . 70
4.5 Analysis of the Growth Mechanism . . . 73
4.6 Conclusion . . . 76
4.7 References . . . 77

5 Aluminium-Carbon Nanotube Interface Electronic Properties: The Effect of Dopants 80
5.1 Introduction . . . 80
5.2 Methods . . . 82
5.3 Electronic Structure of the CNT leads . . . 84
5.4 Al-CNT Interfaces . . . 87
5.5 Conclusion . . . 96
5.6 References . . . 97

6 Effect of Structure on Electronic Properties of the Iron-Carbon Nanotube Interface 101
6.1 Introduction . . . 101
6.2 Methods . . . 101
6.3 Model Systems . . . 103
6.3.1 Iron Nanowire . . . 103
6.3.2 FeNW-(5,0)-CNT Interface . . . 107
6.4 Fe-(10,0)-CNT Interface . . . 110
6.5 Conclusion . . . 114
6.6 References . . . 115

7 Divacancies in Carbon Nanotubes and their Influence on Electron Scattering 116
7.1 Introduction . . . 116
7.2 Methods . . . 118
7.2.1 Electronic Structure Calculations . . . 118
7.2.2 Calculation of Transport Properties . . . 119
7.2.3 Estimation of Mean Free Path . . . 120
7.3 Defective CNT Structures . . . 122
7.3.1 Defects in Zig-Zag CNTs . . . 122
7.3.2 Defects in Armchair CNTs . . . 124
7.3.3 Defects in Graphene . . . 126
7.4 Defect Formation Energies . . . 127
7.5 Electronic Transport Properties . . . 130
7.6 Conclusion . . . 137
7.7 References . . . 139

8 Conclusion 143
8.1 References . . . 146

A Appendix A **147**
A.1 Acronyms 147

List of Figures

2.1 Comparison of graphitic carbon structures. 5
2.2 (a) A graphene sheet showing the relationship between CNT structure, chirality and electronic properties 6
2.3 Band structure for graphene 8
2.4 Electonic structure of graphene and CNTs 9
2.5 CNT growth as it occurs in MD simulation 14
2.6 TEM and tunneling spectra of N-doped CNT 21
2.7 TEM images of defects in graphene 25
2.8 Schottky barrier for n-type semiconductor 26
2.9 Band diagrams for metal-CNT contacts 28

3.1 Schematic of Steepest Descent method 47
3.2 Schematic of the system studied within NEGF method 61

4.1 Structures of the CNT/Nanoparticle complexes 68
4.2 0.7 ELF isosurfaces 69
4.3 Energy levels showing the relative stabilities of the complexes and dissociated products 72
4.4 Schematic of the CNT growth process 74
4.5 TEM images of N-doped bamboo-structured CNTs 75

5.1 Optimised (16,0)-CNT Lead structures 85
5.2 Band Structures of the (16,0)-CNTs 86
5.3 Transmission of the doped CNTs 87
5.4 Structure of the pristine Al-CNT Interface 88
5.5 DOS and Mulliken Charge of pristine Al-CNT Interface 89
5.6 Transmission of end contact between pristine CNT and Al . . . 90
5.7 Comparison NEGF and interpolation IV curves and transmission 91
5.8 Transmission of the pristine and doped Al-CNT interfaces . . . 92
5.9 Current-Voltage graph of the pristine and doped Al-CNT interfaces 94
5.10 Linear Response Current-Voltage Graph 95

6.1 Structure of the FeNW 103
6.2 Band structure of open shell Fe-Lead 104
6.3 DOS of the closed shell Fe-lead and FeNW 105
6.4 DOS of the open shell Fe-Lead and Fe-NW 106
6.5 Structure of the (5,0)-FeNW scattering region 107
6.6 DOS of the (5,0)-FeNW system 108
6.7 Transmission of the (5,0)-FeNW system 109
6.8 IV curve for the (5,0)-FeNW 110
6.9 Structure of the (10,0)-Fe scattering regions 111
6.10 Transmission of the (10,0)-FeNW systems 112
6.11 Linear Response IV curve for Bdoped-CNT Fe interface 113

7.1 Transmission and band structure of the (10,0)-CNT for single and double zeta basis sets 119
7.2 Defects in zig-zag CNTs 123
7.3 Defects in armchair CNTs 125
7.4 LDOS of the 555777 defect in (30,30)-CNT 130
7.5 Transmission spectra for zigzag CNTs 131
7.6 Transmission spectra for armchair CNTs 132
7.7 Mean free path as a function of defect separation 134
7.8 Defect resistance as a function of CNT diameter 136

List of Tables

4.1 Total energies of the cobalt nanoparticle/CNT complexes 71

5.1 Basis sets used for geometry optimisations and NEGF calculations 83

7.1 Formation energies of defects in zig-zag CNTs and graphene . . 128
7.2 Formation energies of defects in armchair CNTs 128
7.3 Proportionality constant between localisation length (ξ) and the distance between defects (l_d) 135

I, Sarah Louise Jones, certify that this thesis is my own work and I have not obtained a degree in this university or elsewhere on the basis of the work submitted in this thesis.

Sarah Louise Jones

Acknowledgements

I would like to give special thanks Prof. Jim Greer and Dr. Andreas Larsson for giving me the opportunity to do this research and for the guidance and helpful discussions during my PhD. I would like to thank my thesis committee, Dr. James Rohan and Prof. Martyn Pemble, for the feedback and suggestions during my reviews. I would also like to thank Dr. Giorgos Fagas and Dr. Peter Larsson for their advice on TIMES and VASP calculations. A big thank you to everyone in the Electronics Theory Group for all the discussions and advice, as a well as contributing to a pleasant working environment. I also want to thank the Tyndall lunch crew past and present for the good times, cake and making each day that bit more enjoyable. A particular thank you to Dr. Irene Yeriskin for listening, commiserating and all the pep talks along the way.

I would like to thank Gabriel Greene and Dr. Jakub Baran for their efforts and discussions on joint work. A thank you to Dr. Lida Ansari for the use of her linear response code. I also wish to thank my experimental collaborators Dr. Justin O'Byrne, Dr. Zhonglai Li, Dr. Peter Fleming. Prof. Michael Morris and Prof. Justin Holmes. I would like to thank the Irish Centre for High End Computing and Science Foundation Ireland for provision of computational facilities and acknowledge financial support from the Irish Research Council for Science, Engineering and Technology. I also thank the Intel Corporation for their support of this work.

Finally, I wish to thank my family for all their support and encouragement throughout my education.

Dissemination

Papers

1. J.P. O'Byrne, Z. Li, **S.L.T. Jones**, P.G. Fleming, J.A. Larsson, M.A. Morris and J.D. Holmes. Nitrogen-Doped Carbon Nanotubes: Growth, Mechanism and Structure. *ChemPhysChem*, 12:2995-3001, 2011.

2. **S.L.T. Jones** and J.C. Greer. Formation of Contacts between Doped Carbon Nanotubes and Aluminum Electrodes. Submitted to *Journal of Applied Physics*.

3. G. Greene-Diniz, **S.L.T. Jones**, G. Fagas, M. Haverty, C. Martinez-Lacambra, S. Shankar and J.C. Greer. Divacancies in Carbon Nanotubes and their Influence on Electron Scattering. Submitted to *Journal of Physics: Condensed Matter*.

4. **S.L.T. Jones**, G. Greene-Diniz, M. Haverty, C. Martinez-Lacambra, S. Shankar and J.C. Greer. Effect of Structure on Electronic Properties of the Iron-Carbon Nanotube Interface. In preparation.

Conference Presentations

1. "Simulation of Growth and Electron Transport Properties of Nitrogen-Doped Carbon Nanotubes" **S.L.T. Jones**, L. Ansari, G. Greene-Diniz, B. Feldman, J.A. Larsson, G. Fagas, J.C. Greer, C. Martinez-Lacambra, D. Nikonov, S. Park, M.G. Haverty and S. Shankar. Intel European Research and Innovation Conference, October 2010, Leixlip, Ireland.

2. "*Ab initio* Study of CNT-metal contact characteristics" **S.L.T. Jones** and J.C. Greer, Nano and Giga Challenges in Electronics, Photonics and Renewable Energy, September 2011, Moscow, Russia.

3. "The Effect of Vacancy Defects on Electron Scattering in Carbon Nanotubes" **S.L.T. Jones**, G. Greene-Diniz, G. Fagas, M. Haverty, C. Martinez-Lacambra, S. Shankar and J.C. Greer. Trends in Nanotechnology, September 2012, Madrid, Spain.

Abstract

Carbon nanotubes (CNTs) are hollow tubes of sp^2-hybridised carbon with diameters of the order of nanometres. Due to their unique physical properties, which include ballistic transport and high mechanical strength, they are of significant interest for technological applications. The electronic properties of CNTs are of particular interest for use as gas sensors, interconnect materials in the semiconductor industry and as the channel material in CNT based field-effect transistors. The primary difficulty associated with the use of CNTs in electronic applications is the inability to control electronic properties at the growth stage; as grown CNTs consist of a mixture of metallic and semi-conducting CNTs. Doping has the potential to solve this problem and is a focus of this thesis. Nitrogen-doped CNTs typically have defective structures; the usual hollow CNT structure is replaced by a series of compartments. Through density functional theory (DFT) calculations and experimental results, we propose an explanation for the defective structures obtained, based on the stronger binding of N to the growth catalyst in comparison to C. In real electronic devices, CNTs need to be contacted to metal, we generate the current-voltage (IV) characteristics of metal-contacted CNTs considering both the effect of dopants and the structure of the interface region on electronic properties. We find that substitutionally doped CNTs produce Ohmic contacts and that scattering at the interface is strongly influenced by structure. In addition, we consider the effect of the common vacancy defects on the electronic properties of large diameter CNTs. Defects increase scattering in the CNT, with the greatest scattering occurring for the largest defect (555777). We validate the independent scattering approximation for small diameter CNTs, which enables mean free paths in large diameter CNTs to be calculated, with a smaller mean free paths found for larger defects.

Chapter 1

Introduction

Carbon nanotubes (CNTs) have been a focus of extensive research since their discovery by Iijima in 1991. Particularly unique are the electronic properties of CNTs, which have attracted the attention of the semiconductor industry as the challenges imposed by aggressive device scaling are now encountering the physical limits of conventional designs and materials. As a result there is a growing interest in "exotic" materials, amongst them CNTs. CNTs behave as metals or semiconductors, depending on their precise structure. Metallic CNTs have a high current carrying capacity and exhibit ballistic conductance; they can carry large currents with low heating. Copper metal is currently used in the semiconductor industry as an interconnect material, however such interconnects fail at small dimensions due to current-induced electromigration (*i.e.* the current is sufficient to move the atoms of the copper interconnect, forming voids in the material). Metallic CNTs have the potential to solve this problem.

Possibly, the greatest challenge which is preventing use of CNTs in many promising applications is the difficulty in generating CNTs with particular electronic properties. As-grown CNTs have diverse electronic properties, with metallic and semiconducting CNTs grown alongside one another. Many prospective CNT applications (*e.g.* interconnects discussed above, transistor channels, gas sensors etc.) require CNTs with specific properties to be reliably produced. De-

spite the extensive efforts of the past two decades, such controlled production of CNTs has not been achieved and indeed a clear path towards such control remains elusive.

In this thesis we are primarily concerned with challenges relating to controlling CNT electronic properties, with special focus placed on doping CNTs, but the effect of defects is also considered. This work uses *ab initio* computational methods to study a diverse range of topics concerned with doped and defective CNTs. We seek to explain the reasons behind the defective structures often seen for doped CNTs, to assess the impact of dopants and structure on the electronic properties of metal-contacted CNTs and also to evaluate the effect of defects, which even in high quality CNTs are unavoidable. Computational methods are particularly useful in this type of work because the atomic level structural control offered enables specific aspects of doping and defects in CNTs to be studied in isolation and in a controlled manner not possible experimentally with current techniques.

1.1 Thesis Outline

This thesis is organised as follows:

Chapter 2 offers an overview of the literature related to CNTs. Following brief sections consisting of a general introduction to the field, this chapter continues with a more detailed discussion of topics particularly relevant to the work of this thesis including CNT growth, doping, defects and metal-CNT contacts.

Chapter 3 provides a brief introduction to the theoretical methods used throughout this work including details of the density functional theory (DFT) and the non-equilibirum Green's function (NEGF) methods. Descriptions of the calculations performed in this work are placed with their respective results and it is intended that this chapter may act as a further explanation of our methodology

as required.

Chapter 4 discusses our studies of the catalytic growth of nitrogen-doped CNTs. Through consideration of theoretical and experimental results we propose an explanation for the origin of the defective structure typically observed for nitrogen doped CNTs.

Chapter 5 describes our investigation of the effects of doping on the electronic properties of CNTs which have been contacted to an Al electrode. The electronic properties of the isolated doped CNTs are first considered, followed by a discussion of transmission and current-voltage curves for the Al-CNT interface structures. We consider both substitutional and endohedral dopants, from which we assess the suitablility of both dopant types to controlling CNT electronic properties.

Chapter 6 is our study of the relationship between contact structure and the electronic properties of iron-CNT end contacts. Two distinct contact structures are considered and we investigate how the structure impacts on charge transfer and electron transmission.

Chapter 7 is concerned with our study of the properties of vacancy defects in CNTs. Formation energies of defects are reported for a range of defects in armchair and zig-zag CNTs. We study the transmission properties of these defects and validate the independent scattering approximation which enables us to study the mean free paths of large diameter, defective CNTs.

Chapter 8 summarises the work of this thesis and concludes based on these results. Suggestions for future avenues of research informed by this work are given.

Chapter 2

Background

2.1 Graphitic Carbon

The family of graphitic carbon consists of graphene, fullerenes, carbon nanotubes (CNTs) and graphite. Graphene is a two-dimensional material consisting of a monolayer of carbon atoms in a honey-comb lattice and may be considered as the parent structure from which the three other graphitic structures may be generated (Figure 2.1). While graphene was studied theoretically for many years, it was thought that as a strictly 2D crystal it could not exist until its isolation from graphite in 2004 by Geim and Novoselov [1]. Buckminsterfullerene was discovered in 1985 by Smalley, Kroto, Curl and co-workers [2], while CNTs were discovered by Iijima in 1991 as a by-product of arc discharge fullerene production [3]. CNTs with a single carbon layer - single-walled CNTs (SWNTs) - were first reported in 1993 [4, 5].

Nanoscale graphitic carbons (*i.e.* fullerenes, CNTs and graphene) have generated much interest in the research community due to their unusual and in many ways unique physical properties [7, 8]. In particular, both graphene and CNTs have received much attention for use in nanoelectronics. Nanoelectronics applications of CNTs have been demonstrated in research laboratories (*e.g.* CNT applications to non-volatile memory [9, 10], interconnects [11, 12] and transistor

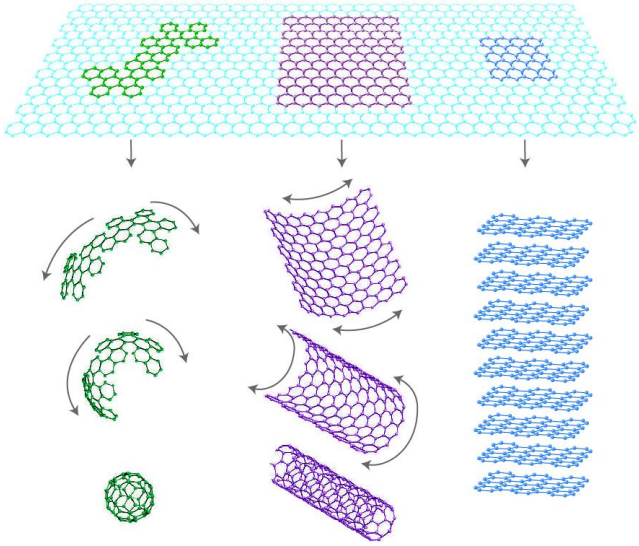


Figure 2.1: Comparison of graphitic carbon structures. Graphene can be rolled to give fullerenes, wrapped to produce CNTs and stacked to generate the graphite structure. Figure taken from ref. [6].

channels [13]), however widespread adoption of CNTs in technology has yet to be realised, the reasons for which will be explained in the following sections. CNTs are also ideally suited to the production of strong, light-weight materials [14] due to their extraordinary mechanical strength [15–18]. The thermal transport abilities of CNTs are directional and surpassed only by diamond [19], which could be applied to thermal interface materials (TIMs) for cooling of hot-spots in microelectronics applications [20] while the high aspect ratio of CNTs has been applied for use in field-emitters [21–23].

2.2 CNT structure and chirality

SWNTs have been produced with diameters as small as 0.4 nm [24], while more typical diameters are of the order of 1-4 nm. At larger diameters, SWNTs are expected to be unstable [25], in any case, larger diameter CNTs are usually multi-walled CNTs (MWNTs), which simply consist of a nested array of SWNTs, with intertube separation comparable to bulk graphite [26]. CNTs with lengths up

to 4 cm have been generated [27]. Conceptually, a SWNT is formed when a graphene sheet is rolled until the two ends meet to form a closed cylinder (as illustrated in Figure 2.1). Depending on the orientation in which the sheet is rolled, SWNTs with many different structures may be generated; this is the origin of CNT chirality.

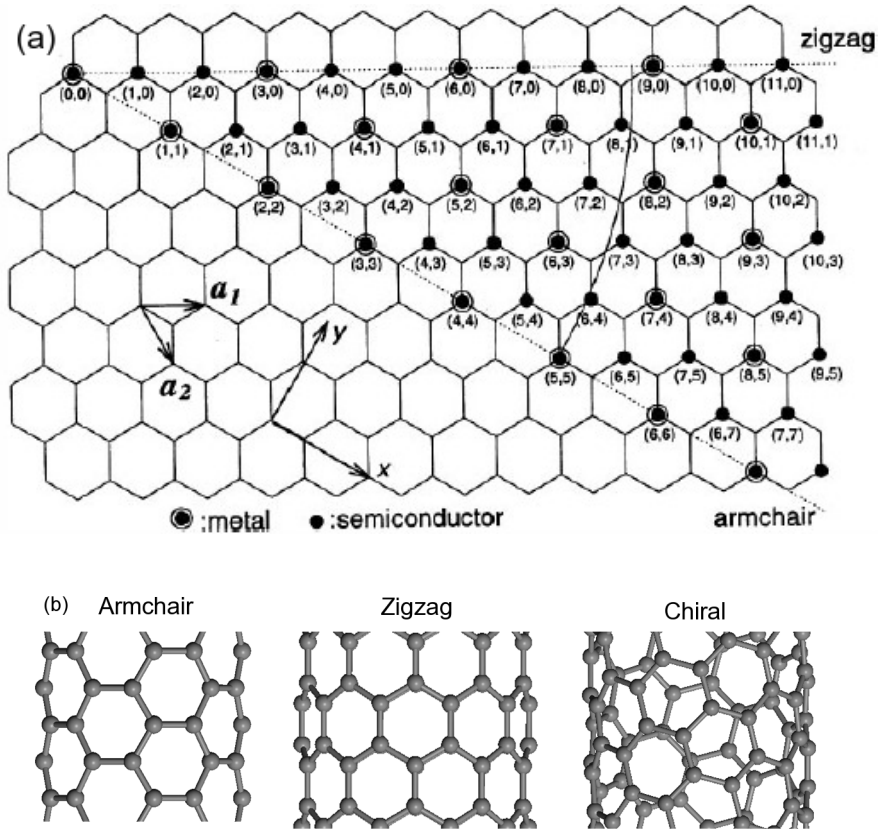


Figure 2.2: A graphene sheet showing the relationship between CNT structure, chirality and electronic properties. Figure taken from ref. [28]. (b) Armchair, zigzag and chiral CNT structures.

A SWNT can be defined by its chiral vector $\mathbf{C}_h$,

$$\mathbf{C}_h = n\mathbf{a}_1 + m\mathbf{a}_2 \equiv (n, m),$$

where (n, m) is often called the chiral number or chiral index of a SWNT. The chiral vector $\mathbf{C}_h$, makes an angle θ, the chiral angle, with the zigzag direction (see Figure 2.2). SWNTs may be classified as one of three chiralities which relate to the way in which the hypothetical graphene sheet producing the SWNT is rolled

and is defined by the chiral angle and index. The chiral angle θ is related to the chiral vector,

$$\theta = \tan^{-1}\left[\frac{\sqrt{3}m}{m+2n}\right].$$

SWNTs with $\theta = 0°$ have chiral index $(n, 0)$ and are zigzag while armchair SWNTs correspond to those with $\theta = 30°$ and have index (n, n). All other SWNTs (*i.e.* those with $0 < \theta < 30°$ and index (n, m) where $n \neq m \neq 0$) are referred to as chiral.

2.3 CNT electronic properties

Unsurprisingly in light of their structural similarities, the electronic properties of CNTs and graphene are intimately related. Each carbon atom in graphene has two 1s electrons, three $2sp^2$ electrons and one $2p_z$ electron. The bonds in the plane of the sheet are formed by the three $2sp^2$ electrons, with the $2p_z$ orbital perpendicular to the graphene sheet. The $2p_z$ orbitals hybridise to form a delocalised network on the surface of graphene. The valence (π) and conduction (π^*) bands of graphene meet at six points (Figure 2.3), as a result graphene may be considered as a semi-metal or zero-gap semiconductor.

The electronic properties of CNTs are defined by their chiralities. The curvature induced by rolling the graphene sheet into a tube alters the electronic properties, even opening a band gap for certain chiralities. All armchair tubes are metallic, while zig-zag and chiral tubes may be semi-metallic, metallic or semiconductors depending on their chiral vector. Tubes with $(m - n)$ a multiple of three are metallic or semi-metallic (depending on tube diameter), all other SWNTs are semiconductors. Due to their quasi one dimensional structure, electronic transport in CNTs occurs ballistically, which enables them to carry high currents with almost no heating [29, 30]. This has resulted in interest in the use of CNTs as a replacement for metal interconnects in complementary metal-oxide

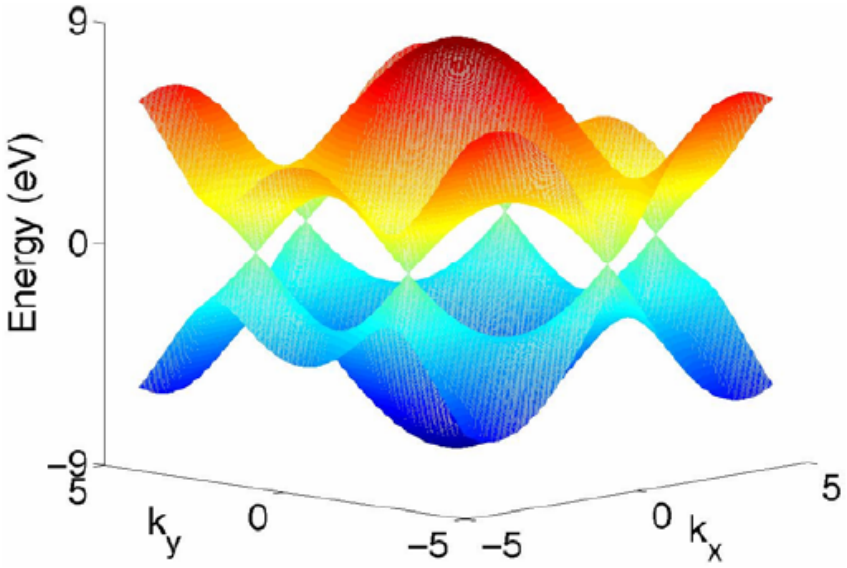


Figure 2.3: Band structure for graphene. Figure taken from ref. [26].

semiconductor (CMOS) technology, which fail due to current-induced electromigration when the wire diameter becomes small. It has also been demonstrated that SWNTs may act as superconductors at low temperatures [31].

The reasons behind the sensitivity of the CNT electronic properties to the chiral index are best understood from a band structure perspective [32]. Near the Fermi level, the electronic structure of graphene is given by an occupied π orbital and unoccupied π^* orbital. These two bands, which have linear dispersion near the K point in the Brillouin zone, meet at the Fermi energy. The valence and conduction bands meet at six points on the corner of the Brillouin zone (see Figure 2.3). The ideal graphene Fermi surface has three corner K points alternating with three corner K′ points. The formation of a SWNT imposes periodic boundary conditions in the circumferential direction which allows only a certain set of graphene states (labelled by the crystal momentum k), which depend on both the diameter and helicity of the SWNT. The allowed set of k-states for three CNT chiralities are shown in Figure 2.4. If the allowed k-states include the K (or K′) point of the graphene Fermi surface, the CNT is metallic, in all other cases it is a semiconductor with band gap inversely proportional to

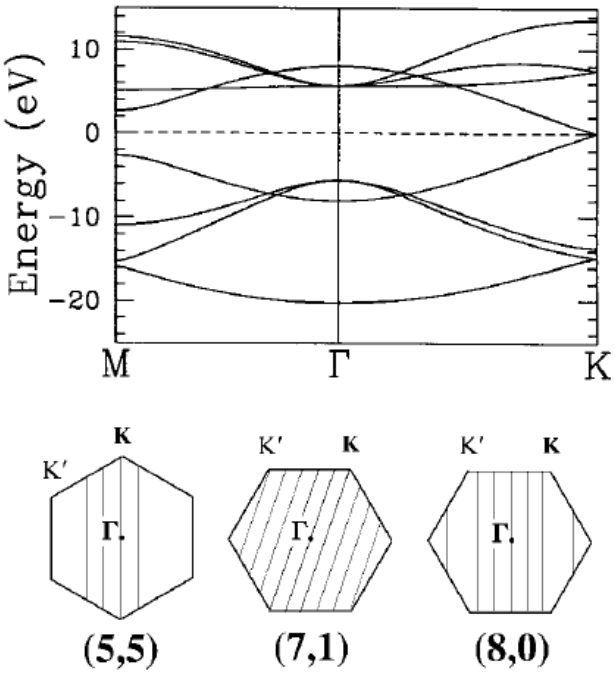


Figure 2.4: *(Top)* Electronic structure of graphene showing high symmetry points. *(Bottom)* Allowed $\vec{k}$-vectors of (*5,5*), (*7,1*) and (*8,0*) tubes (metallic, metallic and semiconducting respectively). Figure taken from ref. [32].

the diameter.

From an applications perspective, the range of CNT electronic properties makes CNTs an exciting material - however for many electronics applications CNTs with specific electronic characteristics are essential (*e.g.* metallic CNTs for interconnects [11, 12], semiconducting CNTs for transistor channels [13]). The difficulties in selectively growing CNTs with a desired chirality (and hence controllable electronic characteristics) and post-synthesis separation [33, 34] are technologically preventing the incorporation of CNTs in nanoelectronics technology. This research focuses on exploring doping as a means of controlling the electronic properties of CNTs, while retaining their advantages as a uniform nanoscale material.

2.4 Chemical Vapour Deposition CNT Growth

A variety of methods are used to produce CNTs (for a detailed discussion of these methods, see ref. [28]). The first CNTs were generated by Iijima in an arc-discharge fullerene reactor [3] using graphite electrodes. SWNTs can be produced when a metal is added to the electrodes [4, 5]. The chemical vapour deposition (CVD) production of CNTs is similar to the general CVD process, except that the use of a metal catalyst is essential, for that reason the process is often referred to as catalytic CVD (CCVD). Typically, a hydrocarbon (*e.g.* methane) flows into a heated furnace at a controlled rate where it is decomposed by a metal catalyst (commonly Fe, Ni or Co) which has been deposited on a substrate (*e.g.* silicon, silica) and CNT growth results. Research into CNT growth has focused on CVD growth, because it allows for large scale production of CNTs [35] at low cost.

2.4.1 The Vapour-Liquid-Solid Mechanism

The growth of CNTs is most commonly considered to take place via a modified vapour-liquid-solid (VLS) mechanism [36], the well-established production method of nanowires [37]. In this mechanism, a catalyst droplet forms on the surface of a substrate. The molten catalyst accepts material from the vapour, which causes it to become supersaturated. Precipitation of dissolved material (in this case carbon) causes the nanotube to grow, with the size of the molten catalyst droplet controlling the size of the nanotube grown. This mechanism explains experimental observations such as the molten morphology often exhibited by the metal catalyst nanoparticles after growth and also the correlation of metal nanoparticle size and tube diameter [38, 39]. One of the main arguments against the VLS mechanism was that typical growth temperatures are far lower than the bulk melting points of the metal catalysts (*e.g.* bulk Ni has a melting point of 1453°C but growth of CNTs takes place at less than 800°C). However metal

nanoparticles melt at a temperature much lower than the bulk, an example of a size effect; the nanoparticles are so small the interfacial energy makes a significant contribution to the total energy and this may cause a depression in melting point [40].

While the VLS mechanism is widely accepted as the catalytic growth mechanism of CNTs, there is still some debate over the precise details of this process. There is a lack of consensus over whether the VLS mechanism takes place in a "tip growth" or "root growth" fashion. In the tip growth process, first described by Baker and co-workers for carbon filaments [41], a temperature gradient is set up in the catalyst particle which is steepest in regions next to the support. Carbon diffuses down the thermal gradient and is deposited between the catalyst and support. This precipitation causes build up of carbon which forces the metal particle away from the substrate. In the context of CNTs, a NT grows as the particle is lifted off the surface. The root growth process is broadly similar, except that the metal particle remains on the substrate and the growing nanotube grows upwards from the catalyst as the incorporated carbon segregates towards the surface [42]. This distinction between tip and root growth becomes important when "cloning" CNTs [43], which involves regrowth of CNTs of a specific chirality.

2.4.2 *In situ* Microscopy of CNT Growth

Time resolved, high resolution *in situ* transmission electron microscopy (TEM) offers a unique glimpse of the growth of CNTs as it happens. A number of such studies have appeared in recent years, offering greater understanding of the CNT growth mechanism and the role of the transition metal catalyst in CCVD growth.

As mentioned previously, there is a strong correlation between nanoparticle size and CNT diameter, so it is unsurprising that the nanoparticle size and shape during growth has been investigated extensively in *in situ* studies. On small diameter nanoparticle catalysts (Ni < 6 nm), SWNTs grow, while "nanocages" have

been observed on larger particles [44]. The size of the nanoparticle under growth conditions also affects its shape; smaller nanoparticles are observed to be highly elongated, while larger ones tend to be pear shaped [45]. A similar behaviour of the nanoparticle catalyst is seen across *in situ* TEM studies of growth [44–47]. Typically, the nanoparticle is spherical when growth initiates. The nanoparticle elongates as the graphene sheets form, this reshaping aids the alignment of the graphene into a tubular structure. The elongation continues (an aspect ratio of 4 has been observed [45]) until binding to the CNT wall no longer compensates for the increased surface energy and it suddenly relaxes back to a spherical shape. This elongation/contraction repeats periodically as the nanotube grows. In all cases catalyst step-edges play an important role in the nucleation and growth of CNTs.

In the case of MWNTs, the individual cylinders have been observed to grow at the same rate [47], which suggests that the density of carbon must be homogeneous at the ends of the cylinders, a requirement most likely achieved by diffusion of carbon through the catalyst rather than along the surface. Bamboo CNT growth has been observed (instead of the typicall hollow CNT structure, the structure consists of repeated short compartments), suggesting that surface diffusion of carbon adatoms is important [46].

There is still disagreement in the literature as to the nature of the nanoparticle catalyst during growth, that is, whether the catalyst is metallic or metal carbide. While some studies conclude that the Ni catalyst is metallic based on the lattice spacing of 0.2 nm [45, 48], which corresponds to Ni (111), this assertion has been questioned, given this reflection is also present in Ni_3(101), Ni_2O_3(200), NiO(112) and graphite(101) [49]. Equally, there is disagreement in the case of Fe. A combination of TEM and XPS data has suggested that the catalyst particle is crystalline with a layer of surface carbide [48], there is also conflicting evidence that the catalyst is cementite, Fe_3C [47]. Possibly, the composition of the catalyst

fluctuates during growth.

While *in situ* microscopy during CNT growth offers a unique view of the CNT growth process, many questions relating to the CNT growth process remain beyond its purview due to the insufficient spatial and temporal resolution of the technique. These questions include such fundamental aspects of CNT growth as what happens at the catalyst before the CNT growth initiates and how exactly the CNT chirality becomes fixed. It also cannot explain why some metals work as catalysts for CNT growth and others do not. In this thesis, we explore one aspect of CNT growth that experimental techniques can not fully explain - why bamboo CNT growth is favoured over typical SWNT/MWNT growth under certain growth conditions.

2.5 Computational Studies of CNT Growth

Computational modelling offers a unique insight into the growth of CNTs at the atomic level, enabling the understanding of CNT growth to be enhanced. Studies in this area are concerned with explaining the role of the transition metal catalyst in CVD growth and also investigating why some metals are successful catalysts and predicting which metals may potentially act as catalysts for CNT growth. Two approaches are taken in the literature to model various aspects of CNT growth, *ab initio* static calculations of geometry optimised structures, which typically focus on energy differences between structures, and molecular dynamics (MD) studies which look at how the CNT-nanoparticle system evolves over time.

2.5.1 Classical Molecular Dynamics

Shibuta and Maruyama [50, 51] have modelled CNT growth on Ni clusters. Ni clusters become saturated with carbon and hexagonal carbon networks form within the cluster. Cap structures appear on the catalyst surface, with the cluster

surface acting as a template. Some areas on the catalyst surface remain free of carbon, enabling additional carbon atoms to flow into the metal-carbon cluster which then deposit at the cap-cluster interface, leading to CNT growth. CNT growth does not occur in cases where the cluster becomes encapsulated with graphitic carbon.

Ding *et al* have proposed a model for CNT nucleation and growth which expands on the VLS mechanism [52–56]. Similar to the studies of Shibuta and Maruyama, carbon readily penetrates into the metal cluster and this carbon subsequently sequesters, leading to CNT growth. The model is consistent with observed experimental results such as the temperature dependence of CNT growth and also the correlation between nanoparticle and nanotube diameter [38, 39]. As this model is based on the VLS mechanism, the supersaturation of the metal catalyst with carbon is essential to successful growth. The nucleation and early growth of a CNT is most conveniently discussed in three stages related to the degree of saturation of the catalyst with respect to carbon (see Figure 2.5).

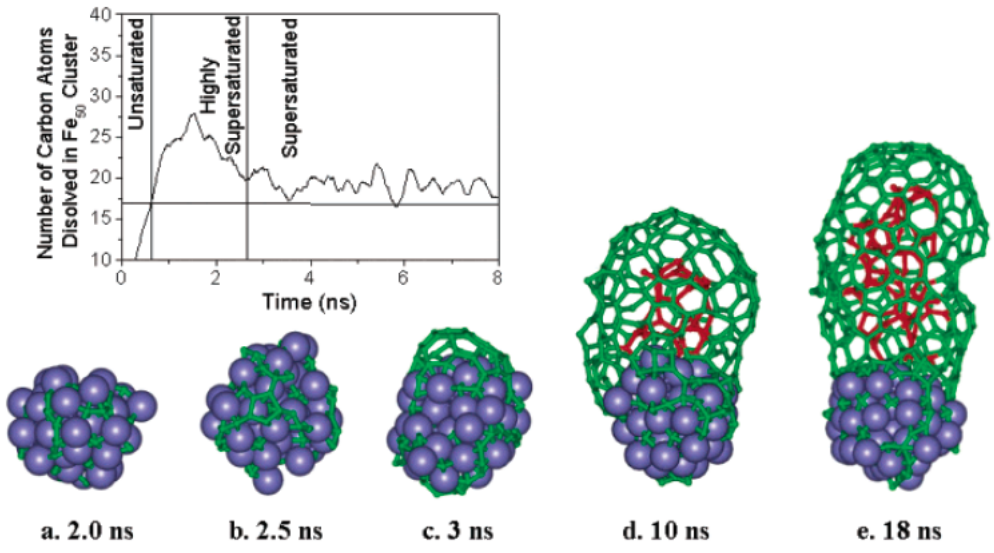


Figure 2.5: CNT growth as occurs in MD simulations. In this case the metal cluster (purple) is Fe_{50} (diameter 1 nm) and the temperature was 1000 K. Figure taken from ref. [52].

In the first stage the metal-carbon cluster is not fully saturated and all carbon

atoms are dissolved in the cluster. The rate of increase of dissolved carbon atoms is equal to the rate of carbon atom insertion into the cluster. The second stage is key for the nucleation of the CNT. The metal-carbon cluster becomes supersaturated with carbon, but the amount of dissolved carbon continues to rise until the cluster becomes highly supersaturated. Carbon precipitates on the surface of the cluster as polygons and strings, which may act as a nucleation site for further carbon precipitation forming graphitic islands. Large islands form by growth or coalescence of smaller islands. The graphitic islands forms a cap, which is pushed further from the catalyst surface as more carbon precipitates and the CNT grows.

2.5.2 DFTB and DFT Molecular Dynamics

As series of extensive density functional tight binding (DFTB) MD simulations of CNT growth have been undertaken by groups at Kyoto University and Nagoya University [57–64]. Inspired by the experiments carried out by Smalley's group which involved increasing the length of a seed nanotube while maintaining diameter and chirality [43], Ohta *et al* simulated regrowth of a hydrogen passivated CNT catalysed by an iron nanoparticle catalyst using DFTB [57, 58]. Regrowth of the CNT fragment was initiated primarily via polyyne chains, which approached the metal-stabilised dangling bonds of the CNT forming 5, 6 and 7 member polygons and thus extended the CNT sidewall. The classical MD studies of Ding, similarly found carbon "strings" (*i.e.* chains of carbon atoms) at the catalyst surface to result in CNT growth. The temperature dependence was considered by performing simulations at 1000K, 1500K and 2000K, with the highest growth rate occurring at 1500K. Carbon atoms penetrated the metal cluster, but due to the short simulation times, such embedded carbon did not participate in CNT growth, which contradicts growth observed in classical MD simulations, where carbon from within the catalyst is responsible for CNT growth.

Following on from regrowth, the CNT growth immediately following CNT cap

nucleation was considered for Ni and Fe catalysts [60, 63]. The catalyst surface remained "cleaner" (*i.e.* fewer string on carbon on the catalyst surface) for Ni than in the Fe case, which was attributed to the longer polyyne chains which predominated on the catalyst surface. Poorer growth (*i.e.* less extension along the cap axis) was associated with the presence of individual carbon atoms and short chains at the catalyst. The details of growth differed between the metal catalysts. In the case of Fe, growth clearly took place via root growth at the CNT-Fe interface. Growth of the cap structure was as a result of reactions with polyyne chains at the rim in addition to incorporation of carbon which diffused along the Fe surface. Ni catalysed growth however, took place via polyyne extension followed by ring collapse close to the cap. A higher growth rate was obtained with Ni clusters, however more defective CNTs were obtained. The large number of defects may be as a result of the short simulations and consequent very high rate of carbon addition. Under experimental conditions, such defects are most likely annealed.

Growth of preformed $(5, 5)$-caps on larger M_{55} clusters (M = Ni, Fe) was also simulated [62]. CNT growth was typified by two distinct behaviours. In some cases, the cap lifted off the cluster surface and elongation of the carbon structure occurred, while in other cases the cluster was encapsulated and elongation inhibited, which was also seen to prevent growth in classical MD simulations. Encapsulation of the cluster occurred more frequently for Fe than for Ni, though this may be a result of the initial structures, which were chosen at random. In the case of Fe, surface C consisted mostly of individual carbon atoms or small moieties, while for Ni clusters surface C was mostly in chains. Carbon penetration into the cluster was limited for Fe and did not occur at all for Ni, this behaviour differs significantly from that previously reported in classical MD studies where dissolved carbon was deemed essential for CNT growth [50–54]. As with the previously discussed studies, CNT growth was strongly associated with polyyne

chains at the catalyst. Analysis of the structure (*i.e.* calculation of the Berry parameter [65]) suggests that the Fe and Ni catalysts remain solid, at least in the early stages of nanotube growth.

Nucleation of CNT on a bare metal cluster was also simulated [59]. C_2 was captured by the iron cluster without dissociation and polymerised on the cluster surface forming polyyne chains. The iron cluster became less organised as more Fe-C bonds formed but C atom penetration into the cluster was rare. The polyyne chains formed on the cluster surface came together forming branched chains. The polyyne chains came together on the surface by diffusion, forming polygons and eventually a CNT cap.

Raty *et al* considered the growth of CNTs from Fe and Au nanoparticles through *ab initio* DFT simulations [66]. Individual C atoms diffused rapidly over the nanoparticle surface until they connected with other C atoms, forming dimers and chains, eventually producing an sp^2 bonded graphene sheet covering the exposed catalyst surface (with pentagon and heptagons to accommodate surface curvature). The cap was held on the surface of the nanoparticle by covalent bonds involving under-coordinated carbon atoms. In the case of Au nanoparticle the binding of carbon was sufficiently weak that dimers readily left the surface and consequently a cap could not form. This result highlights the importance of strength of the metal-carbon bond in the catalysis of CNTs.

2.5.3 DFT studies

With the success of the Fe catalyst versus the Au catalyst being attributed to the stronger metal-carbon bond of the former in the Raty study [66], this phenomenon has been investigated further in DFT calculations for a variety of transition metals [67, 68]. Fe, Co and Ni clusters were chosen, since they are widely used to successfully grow CNTs, in addition Cu, Pd and Au systems were modelled since they are capable of decomposing carbon feedstock gas but are not commonly

employed as catalysts in CCVD growth of CNTs. It was confirmed that the M-C bond strengths of the widely used catalysts are stronger for the metals studied. To understand the reasons that the M-C bond strength is so important to successful CNT growth, the process of dissociating a SWNT from the catalyst and forming a cap was considered. It was found that in the case of Fe, Co and Ni, large positive enthalpies are obtained for these reactions due to their strong M-C bonds, consequently inhibiting cap closure. Au and Cu clusters did not have sufficiently strong M-C bonds to prevent closure, while Pd was found to be borderline with a slightly positive enthalpy of reaction.

Bimetallic catalysts may also catalyse CNT growth, for example Cu/Mo nanoparticles successfully catalyse bamboo CNT growth, and have been modelled in terms of adhesion strengths [69]. For an all Cu cluster, the binding energy of each carbon atom was calculated to be less than that of the carbon dangling bond; an all Cu nanoparticle would thus not be expected to catalyse CNT growth. In the all Mo cluster case, the binding energy was significantly larger than the dangling bond energy, however Mo catalysts fail to produce CNTs. This failure is probably due to Mo-C bond formation being favoured over C-C bond formation, thus preventing CNT growth. Some bimetallic catalyst structures were found to have carbon binding energies comparable to the carbon dangling bond energy, depending on the cluster composition, thus Cu/Mo catalysts can support CNT growth. A similar result has been found in the case of Cu/W and Pd/Mo nanocomposite catalysts [70].

The relative stabilities of possible CNT nucleation structures on Ni clusters have been studied by means of DFT and TBMC (tight-binding Monte Carlo) simulations [71]. A carbon island has a higher chemical potential than an isolated carbon atom on the surface of the Ni cluster, such an island may only form when the surface has a large coverage of carbon. Caps of $(5, 5)$ and $(10, 0)$ tubes have a lower chemical potential than an island; such caps can form spontaneously once

an island is formed. Formation of a cap also inhibits further island formation by lowering the concentration of carbon atoms on the cluster surface. Since the same island enables formation of both caps with different chiralities and the conversion of an island to a cap is spontaneous, this study suggests it is not possible to control CNT chirality. In any case, the difference in chemical potentials between edge atoms for the different chiralities was found to be comparable to the thermal energy at growth conditions and so it may not be possible to control SWNT chirality via cluster engineering, at least in the case of $(10, 0)$ and $(5, 5)$ CNTs. The relationship between tube chirality, cap structure and catalyst structure has also been considered in detail [72–74].

Computational studies of CNT growth typically relate to the CVD production of CNTs, since only this method enables production at industrial levels. The catalyst support is neglected in all studies (due to computational limitations) and so it is unsurprising that these studies either assume or support a root-growth mechanism of CNT growth, though given that the *in situ* microscopy studies also support a root-growth mechanism, the assumption of root-growth is not without basis. Much as found by *in situ* microscopy studies, the MD studies support the basic VLS model of CNT growth, while also increasing understanding of initial CNT growth which *in situ* techniques lack the resolution to observe. DFT studies which explore the energetics of the catalyst CNT-interface also greatly enhance the understanding of the CNT growth process beyond the limits of current experimental techniques.

2.6 Doped CNTs

Doping of carbon nanotubes can be conveniently divided into four different classes, endohedral, exohedral, intercalation and substitutional doping. Endohedral doping involves encapsulating nanostructures in the hollow cavity of the

nanotube, while in exohedral doping nanostructures are adsorbed on the CNT surface. Intercalation may be applied to nanotube bundles and involves inserting molecules between the nanotubes in the bundles [75]. Substitutional doping consists of replacing carbon atoms with other elements (*e.g.* N or B). Substitutional and endohedral doping are discussed in more detail in this section, as they are a central focus of this work.

2.6.1 Substitutional Doping of CNTs

The first reports of nitrogen and boron doped carbon nanotubes appear in the literature as early as 1994 in the form of BCN (boron-carbon-nitrogen) tubes, which were produced by the arc discharge method. This doping was achieved by placing a mixture of elemental B and graphite in the anode, with a pure graphite cathode and performing the arc discharge in a nitrogen atmosphere [76]. The doping levels of the CNTs were low relative to later studies (typically $<$ 2%). Doping of CNTs has also been achieved by heat treatment of SWNTs with B_2O_3 in a nitrogen atmosphere [77, 78]. This method also had the side effect of increasing the diameter of the CNT (from 1.4 nm to 2.1-3.2 nm). This diameter increase is caused by coagulation of NTs to eliminate dangling bonds which were introduced by the doping process. Such diameter increase has also been observed to occur under electron irradiation in CCVD produced SWNTs [79].

Direct substitution of nitrogen into the CNT (*i.e.* the replacement of carbon by equal amounts of N) is not the only way to include N in the CNT, pyridine-like environments may also form. In the pyridine-like configuration, a carbon atom vacancy is formed leaving a two coordinate N. Substitutional doping by N typically leads to the formation of "bamboo" MWCNTs [79–87]. In contrast, even the very earliest reports of boron doped CNTs suggest that it directly substitutes C in the CNT and the typical CNT structures (*i.e.* SWNT/MWNT) are maintained on doping [77, 88].

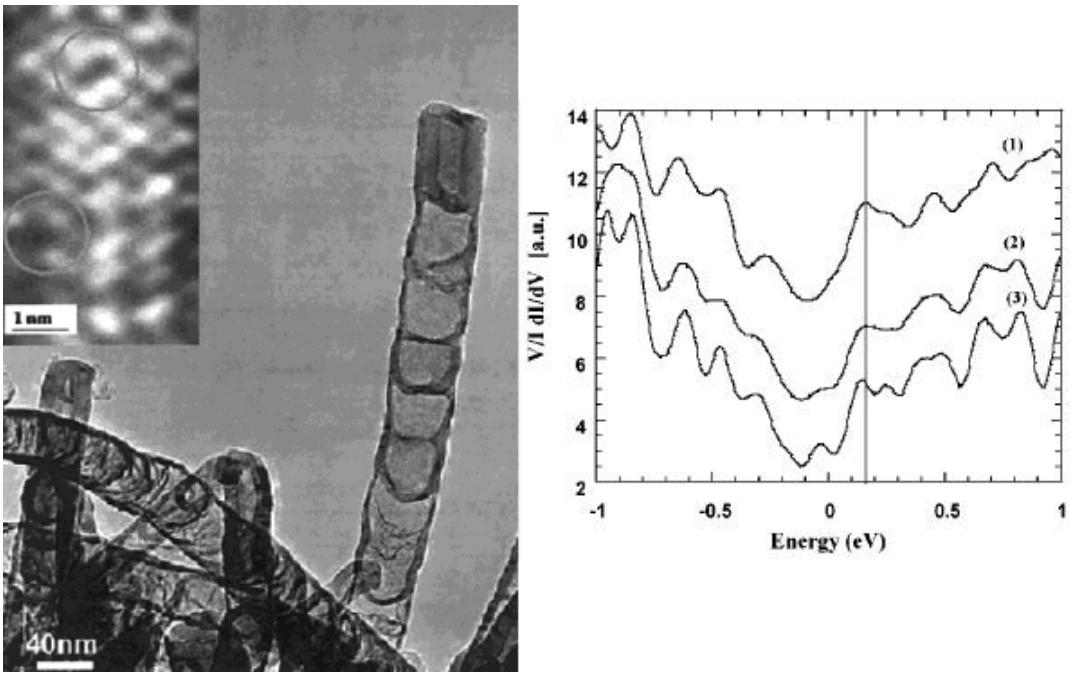


Figure 2.6: Left: TEM of bamboo MWNTs produced by CCVD. Inset: STM image of CNT showing holes in the lattice. Right: Tunnelling spectra taken from three locations close to holes showing the peak at 0.18 eV in each case. Figures taken from ref. [80].

The effect which substitutional doping has on the electronic properties of CNTs is of great interest, since doping may offer a possibility of controlling CNT electronic properties, bypassing the issue of chirality control. CCVD growth using nitrogen/boron containing carbon sources (or commonly used carbon sources with a nitrogen/boron source) is the most widely used route towards substitutional doping of N and B into the carbon network [79–87, 89]. STM imaging shows that there are large holes (up to 0.7 nm in diameter, see the left panel of Figure 2.6) in the walls of N-doped CNTs, which are likely caused by the presence of pyridine-like environments [80]. While the tunnelling spectra of undoped CNTs and N-CNTs are similar, there are important differences, which impact significantly on their ultimate electronic properties. In the spectra of N-CNTs, an extra electronic feature is seen at 0.18 eV on otherwise symmetric spectra (right panel of Figure 2.6). The presence of electronic states at the Fermi level also indicates that the N-CNTs may be metallic [79]. B-doped CNTs have also been shown to be

metallic at room temperature [90]. Nitrogen doped CNTs with semiconducting chirality in the absence of a substitutional dopant have also been found to be metallic within DFT/NEGF, while incorporation of substitutional nitrogen in an armchair CNT was found to reduce electron transmission [91]. Otherwise semiconducting CNTs have also been found to be metallic on introduction of boron dopants at experimentally relevant concentrations within DFT [92], while substitutional boron dopants in already metallic CNTs were found to shorten the mean free path for electrons [93].

In experiment, very high doping levels are achieved in substitutional doped CNTs. This results in metallic CNT properties irrespective of CNT chirality *i.e.* the "chirality problem" is by-passed, at least when metallic CNTs are required. Difficulties still remain with controlling dopant levels within the CNT and also dopant atom fluctuations within the CNT (*e.g.* outer layers of MWNTs have been reported as being more heavily doped than inner layers [94]). Tube morphology remains a particular problem for nitrogen doped CNTs, with bamboo CNT structures consistently obtained; the reasons why such defective CNTs result when nitrogen dopants are introduced during CNT growth is an issure explored by this thesis.

2.6.2 Endohedral Doping of CNTs

Endohedral doping of CNTs offers many potential advantages over substitutional doping and such dopants are considered alongside substitutional dopants in this work. Encapsulation of organic molecules which have different electron affinities and ionisation potentials offers the possibility for both n- and p-type doping of CNTs depending on the charge transfer properties of the dopant. Endohedral doping also overcomes problems associated with substitutional doping such as control of doping and CNT morphology.

A wide range of molecules have been explored as endohedral dopants of CNTs,

including fullerenes [95], metallocenes [96] and organic molecules [95, 97–101]. Takenobu and coworkers [100] studied a range of organic endohedral dopants. It was determined that the electronic properties of the doped CNTs are strongly influenced by the properties of the encapsulated molecule. Molecules with large electronic affinity (EA) induce p-type doping in CNTs, while encapsulation of those with small ionisation potential (IP) resulted in n-type doping. Importantly from an applications perspective, many endohedral dopants were found to be stable in atmospheric conditions.

Following this work by Takenobu *et al*, many groups sought to investigate the electronic properties of endohedrally doped CNTs in more detail. Unsurprisingly, endohedral dopants which induced n-type doping were found to donate electrons to the CNT, while electrons were donated from the CNT to the dopant for p-type dopants [99]. Thus dopants with small IP donate electrons to the CNT giving n-type doping, while dopants with high electron affinity EA accept electrons from the CNT resulting in p-type CNTs. The electron transfer to (from) the CNT was found to increase with decreasing IP (increasing EA) of the dopant. Significant differences in band structure have been found for different dopants. Dopants which result in n-type doping add a flat band (the dopant highest occupied molecular orbital (HOMO)) close to or overlapping with the bottom of the CNT conduction band, while dopants from which p-type doping arises add a flat band (the dopant lowest unoccupied molecular orbital (LUMO)) overlapping with the top of the CNT valence band [99]. In most cases, the "intercalation energy" (*i.e.* binding energy) of dopants (intercalation energy = complex energy - energy of CNT - energy of dopant) which were found to be air stable by Takenobu was negative (*i.e.* under ambient conditions dopants would not be expected to escape), while it was positive for dopants which were not air stable. Thus it may be possible to determine the likely air stability of a doped CNT before synthesis by correlation to calculated binding energies.

2.7 Defects in CNTs

CNTs contain defects which are introduced during the growth process or may be introduced during post-processing (for example by ion irradiation [102] or acid treatment [103]).The average mean free path (the average distance an electron travels before being scattered) has been reported as ~ 1 μm for CVD grown CNTs [104] and indeed high quality CNTs have been found to have approximately one defect every 4 μm, although defects were found to cluster together, meaning average defect separation was much shorter [103]. Many different types of defects have been reported in carbon nanotubes including vacancy defects, Stone-Wales defects [105] and adsorption of adatoms as interstitials. This section is primarily concerned with vacancy defects, where one or more atoms in the CNT lattice are missing.

Experimentally it is challenging to identify defects in CNTs. TEM enables atom resolution imaging and so unambiguous identification of defects is possible (Figure 2.7 shows defects in graphene membranes), but is time consuming and impractical for large scale analysis of CNT quality required for industrial level production. Raman spectroscopy is widely used to quantify CNT crystallinity [106], but gives no information on defect location or identity while selective electrochemical deposition can be used to locate defects it is also unable to identify their atomic structure [103].

In monovacancies, a single atom is missing at the defect site, whereas in divacancies there are two missing atoms. Reconstruction at the defect site typically leads to formation of a 5- and 9-membered ring for monovacancies, exemplified for graphene in the right panel of Figure 2.7. The situation for divacancies is more complex, with two possible reconstructions. In the 585 divacancy defect, the structure at the defect relaxes to an 8-membered ring bordered by two 5-membered rings whereas in the 555777 divacancy defect the CNT rearranges resulting in a circular motif of alternating 5- and 7-membered rings.

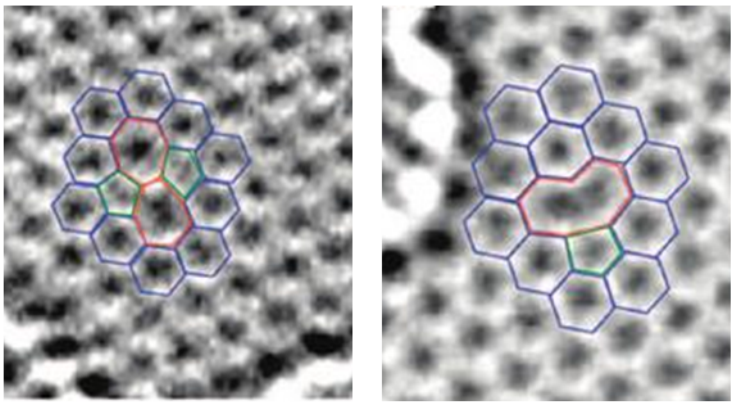


Figure 2.7: TEM images of defects in graphene. Left: Stone-Wales defect, with heptagons outlined in red and pentagons in green. Right: Reconstructed monovacancy, 9-membered ring outlined in red and pentagon in green. Figure taken from ref. [107].

As a result of the difficulties in identifying defects in CNTs, much research in CNT defects has been theoretical and includes studies on mechanical (*e.g.* [108–110]) and electronic properties (*e.g.* [111–114]) with results much as could be anticipated, *i.e.* defects reduce mechanical strength and conductivity. The formation of a divacancy has consistently been found to be more stable than two monovacancies [111, 113], and 585 divancancies are reported as being more stable than 555777 divacancies in CNTs [111], whereas the 555777 defect is more stable in graphene [115]. Due to computational limitations most theoretical studies of CNTs focus on small diameter CNTs which have high curvature. Graphene is the limiting zero-curvature case and so in sufficiently large CNTs the 555777 defect must become more stable than the 585. This has been estimated to occur for CNT diameters greater than approximately 40 Å [111].

At this time, theoretical studies are the only realistic method to study the properties of specific defects due to the difficulties in identifying defects *in situ*. *Ab initio* studies are confined to low diameter/high curvature CNTs. In this thesis, we extend this work to larger diameter CNTs and thus can explore the effects of defects on electronic properties at technologically relevant diameters and also can confirm the relative stability of defects in such CNTs.

2.8 CNT-Metal Contacts

Much interest in CNTs has been related to their electronic properties, discussed in Section 2.3. For these properties to be harnessed in real electronic devices, CNTs must be contacted to metal. The nature of the metal-CNT contact is not well understood, and indeed experiments have often produced seemingly contradictory results, but gradually a picture of what happens at such a contact has begun to emerge. In this section experiment and theory will be briefly discussed to outline the metal-CNT contact as it is currently understood.

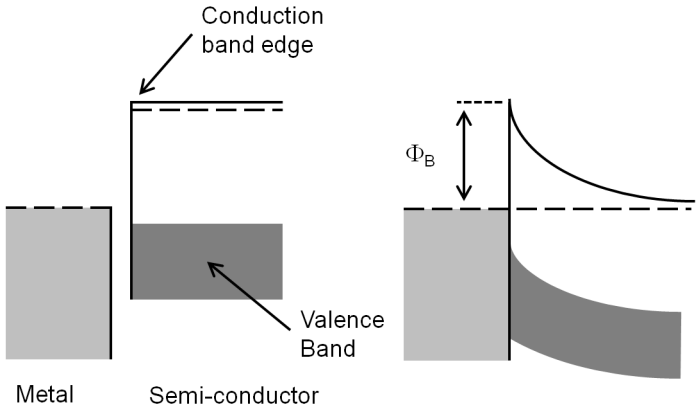


Figure 2.8: Schottky barrier for n-type semiconductor, the work function is indicated by the dashed lines. Left: Bands just before contact is made. Right: Band bending after thermal equilibrium is reached. Φ_B is the Schottky barrier height.

When a semiconductor and metal are brought together a contact is formed. This contact may be Ohmic or Schottky depending on the materials used and also how the contact is prepared. An Ohmic contact exhibits a linear, symmetric current-voltage curve, while a non-linear curve (rectifying behaviour) is obtained with a Schottky contact. A basic description of the behaviour at a Schottky contact is given here, a detailed discussion can be found in the review by Tung [116]. When a semiconductor and a metal are brought together, electrons are transferred from the material with the higher work function to the material with the lower work function until their work functions are equal, as shown in Figure 2.8 for an n-type semiconductor. A barrier layer (of height Φ_B) forms in the

semiconductor in which charge is depleted, this barrier then prevents the flow of current asymmetrically, resulting in the rectification typical of a Schottky contact. Whether an Ohmic or Schottky contact is required depends on the application - CMOS interconnects require Ohmic contacts while Schottky contacts are needed for Schottky diodes and Schottky transistors.

Metal-CNT contacts have been found to exhibit both Ohmic and Schottky behaviours. Ohmic contacts have been reported for CNTs contacted to Pd [104, 117, 118] and Rh [118], conversely, Schottky contacts have been reported for Al and Ti [119]. Both Pd and Rh have high work functions (ϕ_m) (5.1 eV and 5.0 eV respectively), while Al and Ti have lower ϕ_m (both 4.3 eV), it is this difference in ϕ_m which has been suggested to lead to very different behaviour when a metal is brought into contact with a CNT [120]. Pd-CNT contacts have also been reported to have a diameter dependent Φ_B, contacts involving small diameter CNTs are reported to have Φ_B of up to 300 meV, while those with larger diameter CNTs have $\Phi_B < 100$ meV [121]. This is consistent with Kim *et al* [117], who found a negligible Φ_B for larger diameter (> 1.6 nm) semiconducting CNTs in contact with Pd and Rh. Additionally, metal contacts can induce doping in the contacted CNT [122], with the different doping regimes related to the metal ϕ_m, p-type behaviour is seen in the case of Pd and Ti; ambipolar behaviour for Mg ($\phi_m = 3.6$ eV) and n-type behaviour for Ca ($\phi_m = 2.9$ eV). This behaviour can be understood by considering the band diagrams (see Figure 2.9). In the case of Pd and Ti, with larger ϕ_m, the E_f (Fermi energy) of the metal presumably lies close to the valence band edge of the CNT resulting in the easy injection of holes into the CNT, conversely for Ca with its very low ϕ_m, the E_f lies close the conduction band edge and n-type behaviour results. The ambipolar behaviour of Mg then suggests that the E_f lies near the middle of the CNT gap. Indeed, early computational work on metal-CNT interfaces suggested that the metal work function could be used to control the contact behaviour [120]. A detailed discussion of the literature

relating to Schottky barriers at metal-CNT contacts is given in the review of Svensson and Campbell [123].

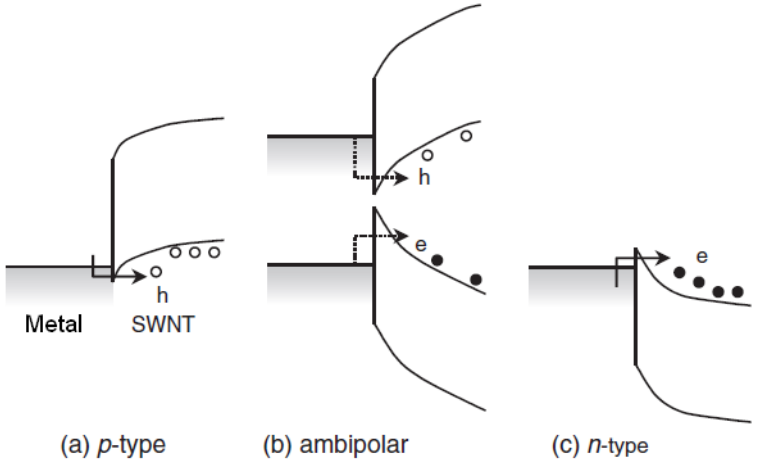


Figure 2.9: Band diagrams at the metal CNT contacts for (a) Pd- and Ti-CNT contacts, (b) Mg-CNT and (c) Ca-CNT. Figure taken from ref. [122].

A series of papers by Andriotis and co-workers have theoretically examined CNT transport properties (only metal-CNT contacts will be discussed here) to study the effect of geometry on contact properties by placing one or two Ni atoms on the side wall of metallic $(5, 5)$ and $(10, 0)$ CNTs [124, 125]. It was found that the character of the bonding and contact changed with the position of the metal, covalent bonds, metallic conduction and low contact resistance resulted from Ni at bridging sites (*i.e.* between C atoms) while ionic bonds, tunnelling conduction and high contact resistance resulted when Ni was at an on-top site (*i.e.* on one C atom). More recently, end- [126, 127] and side-contacted [126] $(10, 0)$-CNTs with Ni were considered. In both cases near linear (*i.e.* Ohmic) IV curves were obtained for short tube lengths, with progressively non-Ohmic IV curves when longer (*i.e.* more realistic) tube lengths were used between the metal contacts.

A number of theoretical studies have considered Al-CNT interfaces for small diameter, undoped CNTs. The earliest such study [128] considers $(10, 0)$ CNTs side contacted to Ca and Al surfaces, with rather different results. For Ca-CNT, the Fermi energy is located above the isolated CNT conduction band edge and

charge transfer from Ca to CNT takes place, while for Al-CNT the Fermi level was found to be below (but close to) the conduction band edge and charge transfer did not occur. This difference in behaviour is attributed to the substantial (1 eV) difference in the metal workfunctions between the two metals. The side contacted type regime has also been studied by Bai and co-workers [129] with a model of "partially-" and "fully-embedded" CNTs. In the fully embedded case the end of the CNT is fully wrapped by Al with one side of the CNT left bare in the partially embedded case. Some rectification behaviour is found for the partially embedded structure. A study of the end contacted Al-CNT interface [130] consisting of an $(8, 0)$-CNT between two Al slabs has also been reported. An interesting aspect of this study is in detailing exactly how far metal induced gap states (MIGS - regions of finite DOS in the contacted semiconductor, which lie in the gap of the isolated semiconductor, due to penetration of the metal surface states) extend into the CNT. Sixteen repeat units of the CNT were required to correctly reproduce the CNT DOS far from the metal interface. The electronic properties of the interface are strongly affected by charge transfer and the resultant MIGS. The end-contacted Al-CNT interface (with $(10, 0)$ CNT) has also been studied [131] but with a very short CNT (2 repeat units) used between the Al leads and any results are most likely strongly affected by the MIGS and indeed Ohmic IV curves were obtained (which is consistent with MIGS overlapping between the metal contacts), much as was found by Andriotis and co-workers at short tube lengths.

It is apparent that the behaviour of the metal-CNT contact is strongly influenced by both the contact metal used and the details of the contact structure. In this thesis, the CNT-metal contact is studied using computational methods and so the structure of the interface can be precisely controlled. This enables the structural dependence of the contact electronic properties to be investigated in a controlled environment.

2.9 Motivation for this Work

The research carried in this work is motivated primarily by the insufficient understanding of CNTs at the atomic scale and consequent difficulties in producing CNTs with the required physical properties for many promising technological applications. In particular, the electronic properties of CNTs may be controlled at the growth stage either through chirality controlled growth or through substitutional doping - however both cases present problems. It is possible to grow CNTs with narrow chiral distributions [132–134] (*i.e.* a small number of chiral indices account for most of the CNTs grown), but full chirality control remains elusive and may well be considered as the "Holy Grail" of the CNT community. Doping of CNTs presents different difficulties and much work is still needed in this area, with regard to suitable doping levels, uniform doping of tubes and tube morphology. In electronic devices at some point the CNT must be contacted to metal and the electronic properties are then also influenced by this contact. While much progress has been made in *in situ* monitoring of CNT growth, such methods have neither the spatial nor temporal resolution to enable atomic scale CNT growth to be studied. Computational modelling offers the unique possibility to study CNTs with full atom-by-atom control. Taking advantage of this atomic-scale control, this thesis focuses on the following topics:

- The origin of the defective structures of nitrogen-doped CNTs
- The effect of dopants on the electronic behaviour of metal contacted CNTs
- The interplay between the structure of a metal-CNT interface and its electronic properties
- The effects of vacancy defects on the electronic properties of large diameter CNTs

This work particularly focuses on the electronic properties of doped and defective CNTs. As has been discussed in this chapter, the electronic properties of CNTs in nanoelectronics are complicated by a number of factors including how the CNT is grown, the presence of defects and impurities in the CNT and how the CNT is contacted and to which metal. Ultimately, this work is driven by the need to better understand how these factors work together in nanoelectronic devices.

2.10 References

[1] K.S. Novoselov, A.K. Geim, S.V. Morozov, D. Jiang, Y. Zhang, S.V. Dubonos, I.V. Grigorieva, and A.A. Firsov. Electric Field Effect in Atomically Thin Carbon Films. *Science*, 306:666–669, 2004.

[2] H.W. Kroto, J.R. Heath, S.C. O'Brien, R.F. Curl, and R.E. Smalley. C_{60} - Buckminsterfullerene. *Nature*, 318:162–163, 1985.

[3] S. Iijima. Helical Microtubules of Graphitic Carbon. *Nature*, 354:56–58, 1991.

[4] S. Iijima and T. Ichihashi. Single-Shell Carbon Nanotubes of 1-nm Diameter. *Nature*, 363:603–605, 1993.

[5] D.S. Bethune, C.H. Kiang, M.S. de Vries, G. Gorman, R. Savoy, J. Vasquez, and R. Beyers. Cobalt-Catalysed Growth of Carbon Nanotubes with Single-Atomic Layer Walls. *Nature*, 363:605–606, 1993.

[6] A.K. Geim and K.S. Novoselov. The Rise of Graphene. *Nature Materials*, 6:193–191, 2007.

[7] R.H. Baughman, A.A. Zakhidov, and de Heer W.A. Carbon Nanotubes - The Route Towards Applications. *Science*, 297:787–792, 2002.

[8] R. van Noorden. Carbon Sequestration: Buried Trouble. *Nature*, 463: 871–873, 2010.

[9] W.B. Choi, S. Chae, E. Bae, J.W. Lee, B.H. Cheong, and J.R. Kim. Carbon-Nanotube-Based Nonvolatile Memory with Oxide-Nitride-Oxide Film and Nanosecond Channel. *Applied Physics Letters*, 82:275–277, 2003.

[10] U. Ganguly, C. Lee, T.H. Hou, and E.C. Kan. Enhanced Electrostatics for Low-Voltage Operations in Nanocrystal Based Nanotube/Nanowire Memories . *IEEE Transactions on Nanotechnology*, 6:22–28, 2007.

[11] P. Avouris, Z.H. Chen, and V. Perebeinos. Carbon-Based Electronics. *Nature Nanotechnology*, 2:605–615, 2007.

[12] G.F. Close, S. Yasuda, B. Paul, S. Fujita, and H.S.P. Wong. A 1 GHz Integrated Circuit with Carbon Nanotube Interconnects and Silicon Transistors. *Nano Letters*, 8:706–709, 2008.

[13] J. Chaste, L. Lechner, P. Morfin, G. Feve, G. Kontos, J.M. Berroir, D.C. Glatti, H. Happy, P. Hakonen, and B. Placais. Single Carbon Nanotube Transistor at GHz Freuquency. *Nano Letters*, 8:525–528, 2008.

[14] O. Breuer, U. Sundararaj, and R.W. Toogood. The Design and Performance of a New Minature Mixer for Speciality Polymer Blends and Nanocomposites. *Polymer Engineering and Science*, 45:868–879, 2004.

[15] A. Krishnan, E. Dujardin, T.W. Ebbesen, P.N. Yianilos, and M.M.J. Treacy. Young's Modulus of Single-Walled Nanotubes. *Physical Review B*, 58:14013–14019, 1998.

[16] M.F. Yu, O. Lourie, M.J. Dyer, K. Moloni, T.F. Kelly, and R.S. Ruoff. Strength and Breaking Mechanism of Multiwalled Carbon Nanotubes under Tensile Load. *Science*, 28:637–640, 2000.

[17] M.F. Yu, B.S. Files, S. Arepalli, and R.S. Ruoff. Tensile Loading of Ropes of Single-Wall Carbon Nanotubes and their Mechanical Properties. *Physical Review Letters*, 84:5552–5555, 2000.

[18] M.R. Falvo, G.J. Clary, R.M. Taylor, V. Chi, F.P. Brooks, S. Washburn, and R. Superfine. Bending and Buckling of Carbon Nanotubes under Large Strain. *Nature*, 389:582–584, 1997.

[19] I. Ivanov, A. Puretzky, G. Eres, H. Wang, Z.W. Pan, and H.T. Cui. Fast and Highly Anisotropic Thermal Transport Through Vertically Aligned Carbon Nanotube Arrays. *Applied Physics Letters*, 89:223110, 2006.

[20] W. Kim, R. Wang, and A. Majumdar. Nanostructuring Expands Thermal Limits. *Nano Today*, 2:40–47, 2007.

[21] M.S. Wang, L.M. Peng, J.Y. Wang, and Q. Chen. Electron Field Emission Chacteristics and Field Evaporation of a Single Carbon Nanotube. *Journal of Physical Chemistry B*, 109:110–113, 2005.

[22] A.G. Rinzler, J.H. Hafner, P. Nikolaev, L. Lou, S.G. Kim, D. Tomanek, P. Nordlander, D.T. Colbert, and R.E. Smalley. Unraveling Nanotubes - Field Emission from an Atomic Wire. *Science*, 269:1550–1553, 1995.

[23] W.A. De Heer, A. Chatelain, and D. Ugarte. A Carbon Nanotube Field Emission Electron Source. *Science*, 270:1179–1180, 1995.

[24] N. Wang, Z.K. Tang, G.D. Li, and J.S. Chen. Single-Walled 4 Å Carbon Nanotube Arrays. *Nature*, 408:50–51, 2000.

[25] J.A. Elliot, J.K.W. Sandler, A.H. Windle, R.J. Young, and M.S.P. Shaffer. Collapse of Single-Wall Carbon Nanotubes is Diameter Dependent. *Physical Review Letters*, 92:095501, 2004.

[26] M.P. Anantram and F. Léonard. Physics of Carbon Nanotube Electronic Devices. *Reports on Progress in Physics*, 69:507–561, 2006.

[27] L.X. Zheng, M.J. O'Connell, S.K. Doorn, X.Y. Liao, Y.H. Zhao, E.A. Akhadov, M.A. Hoffbauer, B.J. Roop, Q.X. Jia, R.C. Dye, D.E. Peterson, S.M. Huang, J. Liu, and Y.T. Zhu. Ultralong Single-Wall Carbon Nanotubes. *Nature Materials*, 3:673–676, 2004.

[28] M. Terrones. Science and Technology in the 21st Centuary: Synthesis, Properties and Applications of Carbon Nanotubes. *Annual Review of Materials Research*, 33:419–501, 2003.

[29] S. Frank, P. Poncharal, Z.L. Wang, and W.A. de Heer. Carbon Nanotube Quantum Resistors. *Science*, 280:1744–1746, 1998.

[30] W. Liang, M. Bockrath, D. Bozovic, J.H. Hafner, M. Tinkham, and H. Park. Fabry-Perot Interference in a Nanotube Electron Waveguide. *Nature*, 411: 665–669, 2001.

[31] A.Y. Kasumov, R. Deblock, M Kociak, B. Reulet, H. Bouchiart, I.I. Khodos, Y.B. Gorbatov, V.T. Volkov, C. Journet, and M. Burghard. Supercurrents Through Single-Walled Carbon Nanotubes. *Science*, 284:1508–1511, 1999.

[32] M.S. Dresselhaus, G. Dresselhaus, and A. Jorio. Unusual Properties and Structure of Carbon Nanotubes. *Annual Review of Materials Research*, 34: 247–278, 2004.

[33] Y.N. Zhang and L.X. Zheng. Towards Chirality-Pure Carbon Nanotubes. *Nanoscale*, 2:1919–1929, 2010.

[34] Z.B. Zhang, X.J. Liu, E.E.B. Campbell, and S.L. Zhang. Alternating Current Dielectrophoresis of Carbon Nanotubes. *Journal of Applied Physics*, 98:056103, 2005.

[35] A.M. Cassell, J.A. Raymakers, J. Kong, and H. Dai. Large Scale CVD Synthesis of Single-Walled Carbon Nanotubes. *Journal of Physical Chemistry B*, 103:6484–6492, 1999.

[36] E.F. Kukovitsky, S.G. L'vov, and N.A. Sainov. VLS-growth of Carbon Nanotubes from the Vapor. *Chemical Physics Letters*, 317:65–70, 2000.

[37] R.S. Wagner and W.C. Ellis. Vapor-Liquid-Solid Mechanism of Single Crystal Growth. *Applied Physics Letters*, 4:89–90, 1964.

[38] E.F. Kukovitsky, S.G. L'vov, N.A. Sainov, V.A. Shustov, and L.A. Chernozatonskii. Correlation between Metal Nanoparticle Size and Carbon Nanotube Growth. *Chemical Physics Letters*, 355:497–503, 2002.

[39] A.G. Nasibulin, P.V. Pikhista, H. Jiang, and E.I. Kauppinen. Correlation between catalyst particle and single-walled carbon nanotube diameter. *Carbon*, 43:2251–2257, 2005.

[40] Y. Homma, Y. Kobayashi, T. Ogino, D. Takagi, R. Ito, Y.J. Jung, and P.M. Ajayen. Role of Transition Metal Catalysts in Single-Walled Carbon Nanotube Growth in Chemical Vapor Deposition. *Journal of Physical Chemistry B*, 107:12161–12164, 2003.

[41] R.T.K Baker, M.A. Barber, P.S. Harris, F.S. Feates, and R.J. Waite. Nucleation and Growth of Carbon Deposits from the Nickel Catalyzed Decomposition of Acetylene. *Journal of Catalysis*, 26:51–62, 1972.

[42] J. Gavillet, A. Loiseau, C. Journet, F. Willaime, F. Ducastelle, and J.C. Charlier. Root-Growth Mechanism for Single-Wall Carbon Nanotubes. *Physical Review Letters*, 87:275504, 2001.

[43] E.E. Smalley, Y.B. Li, V.C. Moore, B.K. Price, R. Colorado, H.K. Schmidt, R.H. Hauge, A.R. Barron, and J.M. Tour. Single-Walled Carbon Nanotube Amplification: *En Route* to a Type-Specific Growth Mechanism. *Journal of the American Chemical Society*, 128:15824–15829, 2006.

[44] M. Lin, J.P.Y. Tan, C. Boothroyd, K.P. Loh, E.S. Tok, and Y.L. Foo. Direct Observation of Single-Walled Carbon Nanotube Growth at the Atomistic Scale. *Nano Letters*, 6:449–452, 2006.

[45] S. Helveg, C. López-Cartes, J. Sehested, P.L. Hansen, B.S. Clausen, J.R. Rostrup-Nielsen, A. Abild-Pedersen, and J.K. Nørskov. Atomic-scale imaging of Carbon Nanofibre Growth. *Nature*, 427:426–429, 2004.

[46] M. Lin, J.P.Y. Tan, C. Boothroyd, K.P. Loh, Tok. E.S., and Y.L. Foo. Dynamical Observation of Bamboo-like Carbon Nanotube Growth. *Nano Letters*, 7:2234–2238, 2007.

[47] H. Yoshida, S. Takeda, T. Uchiyama, H. Kohno, and Y. Homma. Atomic-Scale *In-situ* Observation of Carbon Nanotube Growth from Solid State Iron Carbide Nanoparticles. *Nano Letters*, 8:2082–2086, 2008.

[48] S. Hofmann, R. Sharma, C. Ducati, G. Du, C. Mattevi, C. Cepek, M. Cantoro, S. Pisana, A. Parvez, F. Cervantes-Sodi, A.C. Ferrari, R. Dunin-Borkowski, S. Lizzit, L. Petaccia, A. Goldoni, and J. Robertson. *In situ* Observations of Catalyst Dynamics during Surface-Bound Carbon Nanotube Nucleation. *Nano Letters*, 7:602–608, 2007.

[49] V. Stolojan, Y. Tison, Y. Chan, and R. Silva. Controlled Growth-Reversal of Catalytic Carbon Nanotubes under Electron-Beam Irradiation. *Nano Letters*, 6:1837–1841, 2006.

[50] Y. Shibuta and S. Maruyama. Molecular Dynamics Simulation of Generation Process of SWNTs. *Physica B*, 323:187–189, 2002.

[51] Y. Shibuta and S. Maruyama. Molecular Dynamics Simulation of Formation Process of Single-Walled Carbon Nanotubes by CCVD Method. *Chemical Physics Letters*, 382:381–386, 2003.

[52] F. Ding, A. Rosén, and K. Bolton. Molecular Dynamics Study of the Catalyst Particle Size Dependance on Carbon Nanotube Growth. *Journal of Chemical Physics*, 121:2775–2779, 2004.

[53] F. Ding, A. Rosén, and K. Bolton. Nucleation and Growth of Single-Walled Carbon Nanotubes: A Molecular Dynamics Study. *Journal of Physical Chemsitry B*, 108:17369–17377, 2004.

[54] F. Ding, A. Rosén, and K. Bolton. Dependance of SWNT Growth Mechanism on Temperature and Catalyst Particle Size: Bulk Versus Surface Diffusion. *Carbon*, 43:2215–2234, 2005.

[55] F. Ding and K. Bolton. The Importance of Supersaturated Carbon Concentration and Its Distribution in Catalytic Particles for Single-Walled Carbon Nanotube Nucleation. *Nanotechnology*, 17, 2006.

[56] F. Ding, A. Rosén, E.E.B. Campbell, L.K.L. Falk, and K. Bolton. Graphitic Encapsulation of Catalyst Particles in Carbon Nanotube Production. *Journal of Physical Chemistry B*, 100:7666–7670, 2006.

[57] Y. Ohta, Y. Okamoto, S. Irle, and K. Morokuma. Rapid Growth of a Single-Walled Carbon Nanotube on an Iron Cluster: Density-Functional Tight-Binding Molecular Dynamics Simulations. *ACS Nano*, 2:1437–1444, 2008.

[58] Y. Ohta, Y. Okamoto, S. Irle, and K. Morokuma. Temperature Dependance of Iron-Catalyzed Continued Single-Walled Carbon Nanotube Growth Rates: Density Functional Tight-Binding Molecular Dynamics Simulations. *Journal of Physical Chemistry C*, 113:159–169, 2009.

[59] Y. Ohta, Y. Okamoto, A.J. Page, S. Irle, and K. Morokuma. Quantum Chemical Molecular Dynamics Simulation of Single-Walled Carbon Nanotube Cap Nucleation on an Iron Particle. *ACS Nano*, 3:3413–3420, 2009.

[60] Y. Ohta, Y. Okamoto, S. Irle, and K. Morokuma. Density-functional tight-binding molecular dynamics simulations of SWCNT growth by surface diffusion on an iron cluster. *Carbon*, 47:1270–1275, 2009.

[61] Y. Ohta, Y. Okamoto, and K. Morokuma. Single-Walled Carbon Nanotube Cap Nucleation on an Iron Particle. *Physical Review B*, 79:195415, 2009.

[62] A.J. Page, S. Minami, Y. Ohta, S. Irle, and K. Morokuma. Comparison of Single-Walled Carbon Nanotube Growth from Fe and Ni Nanoparticles using Quantum Chemical Molecular Dynamics Methods. *Carbon*, 48:3014–3026, 2010.

[63] A.J. Page, S. Irle, and K. Morokuma. Polyyne Chain Growth and Ring Collapse Drives Ni-Catalysed SWNT Growth: A QM/MD Investigation. *Journal of Physical Chemistry C*, 114:8206–8211, 2010.

[64] A.J. Page, Y. Ohta, Y. Okamoto, S. Irle, and K. Morokuma. Defect Healing During Single-Walled Carbon Nanotube Growth: A Density-Functional Tight-Binding Molecular Dynamics Investigation. *Journal of Physical Chemistry C*, 113:20198–20207, 2009.

[65] Y.Q. Zhou, M. Karplus, K.D. Ball, and R.S. Berry. The Distance Fluctuation Criterion for Melting: Comparison of Square-Well and Morse Potential Models for Clusters and Homopolymers. *Journal of Chemical Physics*, 116: 2323–2329, 2002.

[66] J.Y. Raty, F. Gygi, and G. Galli. Growth of Carbon Nanotubes on Metal Nanoparticles: A Microscopic Mechanism from *Ab Initio* Molecular Dynamics Simulations. *Physical Review Letters*, 95:096103, 2005.

[67] P. Larsson, J.A. Larsson, R. Ahuja, F. Ding, B.I. Yakobson, H. Duan, A. Rosén, and K. Bolton. Calculating Carbon Nanotube-Catalyst Adhesion Strengths. *Physical Review B*, 75:115409, 2007.

[68] F. Ding, P. Larsson, J.A. Larsson, R. Ahuja, H. Duan, A. Rosén, and K. Bolton. The Importance of Strong Carbon-Metal Adhesion for Catalytic Nucleation of Single-Walled Carbon Nanotubes. *Nano Letters*, 8:463–468, 2008.

[69] Z. Li, J.A. Larsson, P. Larsson, R. Ahuja, J.M. Tobin, J. O'Byrne, M.A. Morris, G. Attard, and J.D. Holmes. Copper/Molybdenum Nanocomposite Particles as Catalysts for the Growth of Bamboo-Structured Carbon Nanotubes. *Journal of Physical Chemistry C*, 112:12201–12206, 2008.

[70] J.P. O'Byrne, Z. Li, J.M. Tobin, J.A. Larsson, P. Larsson, R. Ahuja, and J.D. Holmes. Growth of Carbon Nanotubes from Heterometallic Palladium and Copper Catalysts. *Journal of Physical Chemistry C*, 114:8115–8119, 2010.

[71] X.F. Zhu, B.Y. Xia, M.Y. Guo, Q.A. Zhang, and J.X. Li. Synthesis of Carbon Nanotube Composites with Size-Controlled Silicon Nanoparticles. *Carbon*, 48:3296–3299, 2010.

[72] L. Li, S. Reich, and J. Robertson. Modelling of Nucleation and Chirality Selection of Carbon Nanotubes. *Journal of Nanoscience and Nanotechology*, 6:1290–1297, 2006.

[73] S. Reich, L. Li, and J. Robertson. Structure and Formation Energy of Carbon Nanotube Caps. *Physical Review B*, 72:165423, 2005.

[74] S. Reich, L. Li, and J. Robertson. Control the Chirality of Carbon Nanotubes by Epitaxial Growth. *Chemical Physics Letters*, 421:469–472, 2006.

[75] P. Ayala, P. Arenal, M. Rümmeli, A. Rubio, and T. Pichler. The Doping of Carbon Nanotubes with Nitrogen and their Potential Applications. *Carbon*, 48:575–586, 2010.

[76] O. Stephan, P.M. Ajayan, C. Colliex, P. Redlich, J.M. Lambert, P. Bernier, and P. Lefin. Doping Graphitic and Carbon Nanotube Structures with Boron and Nitrogen. *Science*, 266:1683–1685, 1994.

[77] D. Golberg, Y. Bando, W. Han, K. Kurashima, and T. Sato. Single-Walled B-doped Carbon, B/N-Doped Carbon and BN Nanotubes Synthesized from Single-Walled Carbon Nanotubes through a Substitution Reaction. *Chemical Physics Letters*, 308:337–342, 1999.

[78] D. Golberg, Y. Bando, L. Bourgeois, K. Kurashima, and T. Sato. Large-Scale Synthesis and HRTEM Analysis of Single-Walled B- and N-doped Carbon Nanotube Bundles. *Carbon*, 38:2017–2027, 2000.

[79] M. Terrones, P.M. Ajayan, F. Banhart, X. Blase, D.L. Carroll, J.C. Charlier, R. Czerw, B. Foley, N. Grobert, R. Kamalakaran, P. Kohler-Redlich, M. Rühle, T. Seeger, and H. Terrones. N-doping and Coalescence of Carbon Nanotubes: Synthesis and Electronic Properties. *Applied Physics A - Materials Science and Processing*, 74:355–361, 2002.

[80] R. Czerw, M. Terrones, J.C. Charlier, X. Blase, B. Foley, R. Kamalakaran, B. Grobert, H. Terrones, D. Tekleab, P.M. Ajayan, W. Blau, M. Rühle, and D.L. Carroll. Identification of Electron Donor States in N-Doped Carbon Nanotubes. *Nano Letters*, 1:457–460, 2001.

[81] C. Tang, Y. Bando, D. Golberg, and F. Xu. Structure and Nitrogen Incorporation of Carbon Nanotubes synthesized by Catalytic Pyrolysis of Dimethylformamide. *Carbon*, 42:2625–2633, 2004.

[82] M.S. He, S. Zhou, J. Zhang, Z. Liu, and C. Robinson. CVD Growth of N-Doped Carbon Nanotubes on Silicon Substrates and its Mechanism. *Journal of Physical Chemistry B*, 109:9275–9279, 2005.

[83] WQ Han, P. Kohler-Redlich, T. Seeger, F. Ernst, M. Rühle, N. Grobert, W.K. Hsu, B.H. Chang, Y.Q. Zhu, H.W. Kroto, D.R.M. Walton, M. Terrones, and H. Terrones. Aligned CN_x Nanotubes by Pyrolysis of Ferrocene/C_{60} under NH_3 Atmosphere. *Applied Physics Letters*, 77:1807–1809, 2000.

[84] M. Nath, B.C. Satishkumar, A. Govindaraj, C.P. Vinod, and C.P. Rao. Production of bundles of aligned carbon and carbon-nitrogen nanotubes by the pyrolysis of precursors on silica-supported iron and cobalt catalysts. *Chemical Physics Letters*, 322:333–340, 2000.

[85] S.H. Lim, H.I. Elim, X.Y. Gao, T.S. Wee, W. Ji, J.Y. Lee, and J. Lin. Electronic and Optical Properties of Nitrogen-Doped Multiwalled Carbon Nanotubes. *Physical Review B*, 73:045402, 2006.

[86] Y.L. Li, F. Hou, Z.T. Yang, J.M. Feng, X.H. Zhong, and J.Y. Li. The Growth of N-doped Carbon Nanotube Arrays on Sintered Al_2O_3 Substrates. *Materials Science and Engineering B - Advanced Functional Solid-State Materials*, 158:69–74, 2009.

[87] Y. Cao, Y. Zhao, Q. Li, and Q. Jiao. Catalytic Synthesis of Nitrogen-Doped Multi-Walled Carbon Nanotubes Using Layered Double Hydroxides as Catalyst Precursors. *Journal of Chemical Sciences*, 121:225–229, 2009.

[88] Ph. Redlich, J. Loeffler, P.M. Ajayan, J. Bill, F. Aldinger, and M. Rühle. B-C-N Nanotubes and Boron Doping of Carbon Nanotubes. *Chemical Physics Letters*, 260:465–470, 1996.

[89] J.D. Wiggins-Camacho and K.J. Stevenson. Effect of Nitrogen Concentration on Capacitance, Density of States, Electronic Conductivity and Morphology of N-Doped Carbon Nanotube Electrodes. *Journal of Physical Chemistry C*, 113:19082–19090, 2009.

[90] K. Liu, Ph. Avouris, and R. Martel. Electrical Transport in Doped Multiwalled Carbon Nanotubes. *Physical Review B*, 63:161404, 2001.

[91] C.-C. Kaun, B. Larade, H. Mehrez, J. Taylor, and H. Guo. Current-Voltage Characteristics of Carbon Nanotubes with Substitutional Nitrogen. *Physical Review B*, 65:205416, 2002.

[92] J.A. Talla. First Principles Modeling of Boron-Doped Carbon Nanotube Sensors. *Physica B*, 407:966–970, 2012.

[93] S. Latil, S. Roche, D. Mayou, and J.-C. Charlier. Mesoscopic Transport in Chemically Doped Carbon Nanotubes. *Physical Review Letters*, 92:256805, 2004.

[94] W.K. Hsu, S. Firth, Ph. Redlich, M. Terrones, H. Terrones, Y.Q. Zhu, N. Grobert, A. Schilder, Clark. R.J.H., H.W. Kroto, and D.R.M. Walton. Boron-Doping Effects in Carbon Nanotubes. *Materials Chemistry*, 10:1425–1429, 2000.

[95] W.Z. Liang, J.L. Yang, and J. Sun. Controllable p and n doping of Single-Walled Carbon Nanotubes by Encapsulation of Organic Molecules and Fullerene: A Theoretical Investigation. *Applied Physics Letters*, 86:223113, 2005.

[96] L.J. Li, A.N. Khlobystov, J.G. Wiltshire, G.A.D. Briggs, and R.J. Nicholas. Diameter-Selective Encapsulation of Metallocenes in Single-Walled Carbon Nanotubes. *Nature Materials*, 4:481–485, 2005.

[97] V. Meunier and B.G. Sumpter. Amphoteric Doping of Carbon Nanotubes by Encapsulation of Organic Molecules: Electronic Properties and Quantum Conductance. *Journal of Chemical Physics*, 123:024705, 2005.

[98] J. Lu, S. Nagese, X.W. Zhang, D. Wang, M. Ni, Y. Maeda, T. Wakahara, T. Nakahodo, T. Tsuchiya, T. Akasaka, Z.X. Gao, D.P. Yu, H.Q. Ye, W.N. Mei, and Y.S. Zhou. Selective Interaction of Large or Charge-Transfer Aromatic Molecules with Metallic Single-Walled Carbon Nanotubes: Critical Role of the Molecular Size and Orientation. *Journal of the American Chemical Society*, 128:5114–5118, 2006.

[99] J. Lu, S. Nagese, D.P. Yu, H.Q. Ye, R.S. Han, Z.X. Gao, S. Zhang, and L.M. Peng. Amphoteric and Controllable Doping of Carbon Nanotubes by Encapsulation of Organic and Organometallic Molecules. *Physical Review Letters*, 93:116804, 2004.

[100] T. Takenobu, T. Takano, M. Shiraishi, Y. Murakami, M. Ata, K. Katuara, Y. Achiba, and Y. Iwasa. Stable and Controlled Amphorteric Doping by Encapsulation of Organic Molecules inside Carbon Nanotubes. *Nature Materials*, 2:683–688, 2003.

[101] R.G.A. Veiga and R.H. Miwa. *Ab Initio* Study of TCNQ-doped Carbon Nanotubes. *Physical Review B*, 73:245422, 2006.

[102] A.V. Krasheninnikov, K. Nordlund, and J. Keinonen. Production of Defects in Supported Carbon Nanotubes under Ion Irradiation. *Physical Review B*, 65:165423, 2002.

[103] Y. Fan, B.R. Goldsmith, and P.G. Collins. Identifying and Counting Point Defects in Carbon Nanotubes. *Nature Materials*, 4:906–911, 2005.

[104] D. Mann, A. Javey, Q. Wang, and H. Dai. Ballistic Transport in Metallic Nanotubes with Reliable Pd Ohmic Contacts. *Nano Letters*, 3:1541–1544, 2003.

[105] A.J. Stone and D.J. Wales. Theoretical Studies of Icosahedral C_{60} and Some Related Species. *Chemical Physics Letters*, 128:501–503, 1986.

[106] H. Hiura, T.W. Ebbesen, K. Tanigaki, and H. Takahashi. Raman Studies of Carbon Nanotubes. *Chemical Physics Letters*, 202:509–512, 1993.

[107] J.C. Meyer, C. Kisielowski, R. Erni, M.D. Rossell, M.F. Crommie, and A. Zettl. Direct Imaging of Lattice Atoms and Topological Defects in Graphene Membranes. *Nano Letters*, 8:3582–3586, 2008.

[108] M. Sammalkorpi, A. Krasheninnikov, A. Kuronen, L. Nordlund, and K Kaski. Mechanical Properties of Carbon Nanotubes with Vacancies and Related Defects. *Physical Review B*, 70:245416, 2004.

[109] S. Zhang, S.L. Mielke, R. Khare, D. Troya, R.S. Ruoff, G.C. Schatz, and T. Belytschko. Mechanics of Defects in Carbon Nanotubes: Atomistic and Multiscale Simulations. *Physical Review B*, 71:115403, 2005.

[110] N.M. Pugno. Young's Modulus reduction of Defective Nanotubes. *Applied Physics Letters*, 90:043106, 2007.

[111] R.G. Amorim, A. Fazzio, A. Antonelli, F.D. Novaes, and A.J.R. da Silva. Divacancies in Graphene and Carbon Nanotubes. *Nano Letters*, 7:2459–2462, 2007.

[112] B. Biel, F.J. Garcia-Vidal, A. Rubio, and F. Flores. Anderson Localization in Carbon Nanotubes: Defect Density and Temperature Effects. *Physical Review Letters*, 95:266801, 2005.

[113] B. Biel, F.J. Garcia-Vidal, A. Rubio, and F. Flores. *Ab initio* Study of Transport Properties in Defected Carbon Nanotubes: An O(N) Approach. *Journal of Physics-Condensed Matter*, 20:294214, 2008.

[114] H. Zeng, J.-P. Leburton, H. Hu, and J. Wei. Vacancy Cluster-Limited Electronic Transport in Metallic Carbon Nanotubes. *Solid State Communications*, 151:9–12, 2011.

[115] G.-D. Lee, C.Z. Wang, E. Yoon, N.-M. Hwang, D.-Y. Kim, and K.M. Ho. Diffusion, Coalescence, and Reconstruction of Vacancy Defects in Graphene Layers. *Physical Review Letters*, 95:205501, 2005.

[116] R.T. Tung. Recent advances in Schottky barrier concepts. *Materials Science and Engineering R*, 35:1–138, 2001.

[117] W. Kim, A. Javey, R. Tu, J. Cao, Q. Wang, and H.J. Dai. Electrical Contacts to Carbon Nanotubes Down to 1 nm in Diameter. *Applied Physics Letters*, 87:173101, 2005.

[118] W.G. Zhu and E. Kaxiras. The Nature of the Contact between Pd Leads and Semiconducting Carbon Nanotubes. *Nano Letters*, 6:1415–1419, 2006.

[119] J Liu, C.G. Lu, L. An, Q.A. Fu, H. Zhang, and J. Murduck. Schottky Diodes from Asymmetric Metal-Nanotube Contacts. *Applied Physics Letters*, 88: 133501, 2006.

[120] F. Leonard and J. Tersoff. Role of Fermi-Level Pinning in Nanotube Schottky Diodes. *Physical Review Letters*, 84:4693–4696, 2000.

[121] J. Svensson, A.A. Sourab, Y. Tarakanov, D.S. Lee, S.J. Park, S.J. Baek, Y.W. Park, and E.E.B. Campbell. The Dependence of the Schottky Barrier Height on Carbon Nanotube Diameter for Pd-Carbon Nanotube Contacts. *Nanotechnology*, 20:175204, 2009.

[122] Y. Nosho, Y. Ohno, S. Kishimoto, and T. Mizutani. Relation between Conduction Property and Work Function of Contact Metal in Carbon Nanotube Field-Effect Transistors. *Nanotechnology*, 17:3412–3415, 2006.

[123] J. Svensson and E.E.B. Campbell. Schottky Barriers in Carbon Nanotube-Metal Contacts. *Journal of Applied Physics*, 110:111101, 2011.

[124] M. Menon, A.N. Andriotis, and G.E. Froudakis. Curvature Dependence of the Metal Catalyst Atom Interaction with Carbon Nanotube Walls. *Chemical Physics Letters*, 320:425–434, 2000.

[125] A.N. Andriotis, M. Menon, and G.E. Froudakis. Various Bonding Configurations of Transition-Metal Atoms on Carbon Nanotubes: Their Effect on Contact Resistance. *Applied Physics Letters*, 76:3890–3892, 2000.

[126] A.N. Andriotis and M. Menon. Structual and Conducting Properties of Metal Carbon-Nanotube Contacts: Extended Molecule Approximation. *Physical Review B*, 76:045412, 2007.

[127] A.N. Andriotis, M. Menon, and H. Gibson. Realistic Nanotube-Metal Contact Configuaration for Molecular Electronics Applications. *IEEE Sensors Journal*, 8:910–913, 2008.

[128] A. Okada, S. Oshiyama. Electronic Structure of Semiconducting Nanotubes Adsorbed on Metal Surfaces. *Physical Review Letters*, 95:206804, 2005.

[129] P. Bai, E. Li, K.T. Lam, O. Kurniawan, and W.S. Koh. Carbon Nanotube Schottky Diode: An Atomic Perspective. *Nanotechnology*, 19:115203, 2008.

[130] K. Odbadrakh, P. Pomorski, and C. Roland. *Ab Initio* Band Bending, Metal Induced Gap States and Schottky Barriers of a Carbon and Boron Nitride Nanotube Device. *Physical Review Letters*, 73:233402, 2006.

[131] F. Gao, J.M. Qu, and M. Yao. Electrical Contact Resistance at the Carbon Nanotube/Pd and Carbon Nanotube/Al Interfaces in End-Contact by First-Principles Calculations. *Journal of Electronic Packaging*, 133:020908, 2011.

[132] G. Lolli, L.A. Zhang, L. Balzano, N. Sakulchaicharoen, Y.Q. Tan, and D.E. Resasco. Tailoring (m,n) Structure of Single-Walled Carbon Nanotubes by Modifying Reaction Conditions and the Nature of the Support of CoMo Catalysts. *Journal of Physical Chemistry B*, 110:2108–2115, 2006.

[133] X.L. Li, X.M. Tu, S. Zaric, K. Welsher, W.S. Seo, W. Zhao, and H.J. Dai. Selective Synthesis Combined with Chemical Separation of Single-Walled Carbon Nanotubes for Chirality Selection. *Journal of the American Chemical Society*, 129:15770–15771, 2007.

[134] H. Wang, B. Wang, X.Y. Quek, L. Wei, J.W. Zhao, L.J. Li, M.B. Chan-Park, Y.H. Yang, and Y.A. Chen. Selective Synthesis of (9,8) Single Walled Carbon Nanotubes on Cobalt Incorporated TUD-1 Catalysts. *Journal of the American Chemical Society*, 132:16747–16749, 2010.

Chapter 3

Computational Methods

This chapter provides a brief introduction to electronic structure theory emphasising the methods used in this work.

3.1 The Schrödinger Equation

The aim of many electronic structure techniques is to calculate approximate solutions to the time independent, non-relativistic Schrödinger equation [1] and thus obtain information about the energy and other properties of molecules from

$$H\Psi = E\Psi, \tag{3.1}$$

where H is the Hamiltonian operator corresponding to the total energy of a system of electrons and nuclei, Ψ is the wave function and E is the energy of the system. There are many acceptable values for the eigenfunctions Ψ of a molecule; each with its own eigenvalue E. The square of the wavefunction $|\Psi^2|$ gives the probability distribution of the electrons in the system. The Hamiltonian is a sum of the kinetic T and potential V energy and in atomic units ($\hbar = m_e = e = 1$) for N electrons and M nuclei is:

$$H = -\sum_{i=1}^{N} \frac{1}{2}\nabla_i^2 - \sum_{i=1}^{M} \frac{1}{2M_A}\nabla_A^2 - \sum_{i=1}^{N}\sum_{A=1}^{M} \frac{Z_A}{r_{iA}} + \sum_{i=1}^{N}\sum_{j>i}^{N} \frac{1}{r_{ij}} + \sum_{A=1}^{M}\sum_{B>A}^{M} \frac{Z_A Z_B}{R_{AB}} \quad (3.2)$$

where Z_A is the charge of nucleus A, $r_{iA} = |\vec{r}_i - \vec{R}_A|$, $r_{ij} = |\vec{r}_i - \vec{r}_j|$, $R_{AB} = |\vec{R}_A - \vec{R}_B|$ and ∇_i^2 and ∇_A^2 are Laplacian operators and involve differentiation with respect to the coordinates of the ith electron and Ath nucleus, respectively. The first two terms on the right hand side of 3.2 are the kinetic energy of the electrons T_e and nuclei T_n, respectively. The third term V_{ne} describes the attractive potential energy resulting from Coulombic interaction between electrons and nuclei, while the fourth V_{ee} and fifth V_{nn} terms describe the potential energy resulting from repulsive electron-electron and nucleus-nucleus interactions.

3.2 The Born-Oppenheimer Approximation

The Hamiltonian contains pair-wise attractive and repulsive terms (no particles move independently) and cannot be solved exactly except for simple systems (*e.g.* the hydrogen atom). As a result, a series of approximations must be made in order to simplify the problem, the first of which is the Born-Oppenheimer approximation [2]. This approximation exploits the fact that electronic motion occurs on a much shorter time-scale than nuclear motion due to the relative masses of the electrons and nuclei, even in the worst case scenario of the hydrogen atom, the nucleus is almost 2000 times more massive than the electron. The motion of the electrons can, in most circumstances, consequently be decoupled from that of the nuclei and electronic energies can be computed for fixed nuclear positions. T_n is then neglected while V_{nn} is a constant and can be dropped because any constant added to the energy operator H only shifts the operator eigenvalue E; the eigenfunction Ψ is unchanged. Thus the electronic Hamiltonian

is obtained:

$$H_{elec} = -\sum_{i=1}^{N} \frac{1}{2}\nabla_i^2 - \sum_{i=1}^{N}\sum_{A=1}^{M} \frac{Z_A}{r_{iA}} + \sum_{i=1}^{N}\sum_{j>i}^{N} \frac{1}{r_{ij}}. \tag{3.3}$$

The total energy E_{tot} in the damped nuclei approximation is obtained by summing E_{elec} (the electronic energy) and V_{nn}. Once the electronic problem has been solved, the nuclear problem may then be solved using the same idea. Because the electrons move much faster than the nuclei, the electronic coordinates can be replaced by their average values, averaged over Ψ_{elec} (the electronic wave function)

$$\begin{aligned} H_{nucl} = &-\sum_{i=1}^{M} \frac{1}{2M_A}\nabla_A^2 + \sum_{A=1}^{M}\sum_{B>A}^{M} \frac{Z_a Z_b}{R_{AB}} \\ &+ \left\langle -\sum_{i=1}^{N} \frac{1}{2}\nabla_i^2 + \sum_{i=1}^{N}\sum_{A=1}^{M} \frac{Z_A}{r_{iA}} + \sum_{i=1}^{N}\sum_{j>i}^{N} \frac{1}{r_{ij}} \right\rangle. \end{aligned} \tag{3.4}$$

The term in brackets in 3.4 is the electronic energy as a function of nuclear coordinates $E_{elec}(\{R_A\})$ and together with the second term V_{nn} is the total electronic energy as a function of nuclear position $E_{tot}(\{R_A\})$ and 3.4 simplifies to:

$$H_{nucl} = -\sum_{i=1}^{M} \frac{1}{2M_A}\nabla_A^2 + E_{tot}(\{R_A\}). \tag{3.5}$$

$E_{tot}(\{R_A\})$ is the potential energy surface (PES) for nuclear motion, with the minimum of the PES corresponding to the most stable geometry for the system.

3.3 Geometry Optimisation Techinques

The simplest molecule to find the most stable structure of is a linear diatomic, the only parameter to be varied is the bond length. If the energy as a function of

bond length is plotted for small displacements about the equilibrium geometry, a parabola will be obtained, with the optimal geometry at the minimum. For larger molecules such a process would have to be carried out iteratively, bond-by-bond and quickly becomes impractical. Ideally, the geometry should not be optimised a single coordinate at a time, but instead move along the direction of the steepest downward slope on the PES for all coordinates.

Optimisation methods are generalised techniques for finding the stationary points of a function, where the gradient is zero. For many purposes it is the minimum of the function that is of interest (*i.e.* where the matrix of the second derivative (Hessian) is positive definite. The derivative of the function is calculated with finite precision so the gradient is not reduced to zero. Instead the optimisation is considered converged when the gradient is below a selected threshold value. The simplest optimisation method commonly used in electronic structure calculations is steepest descent (SD).

In the SD method, the gradient vector (g) points in the direction where the function increases most, thus the function value is always lowered by stepping the function in the opposite direction. A series of function evaluations are performed in the negative gradient direction ($d = -g$) and once the function starts to increase an approximate minimum can be found by interpolation. A new gradient may then be calculated at this interpolated point and used for a new line search. The SD method is guaranteed to always approach a local minimum, however due to the inefficiencies of the method (each line search tends to partially undo the previous one and the closer to the minimum the slower the convergence as shown in Figure 3.1), it is usually used only when other methods fail.

The conjugate gradient (CG) method attempts to prevent the "partial undoing" of the previous line search intrinsic to the SD method. Instead of the next line search being perpendicular to the previous, it is carried out on a line which is a conjugate to previous search directions, as a result successive minimisations

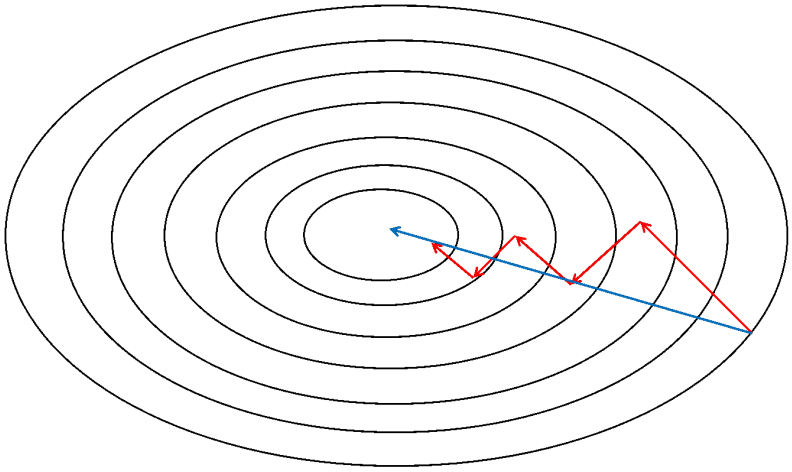


Figure 3.1: Schematic of the steepest descent method, showing the "partial undoing" of the previous optimisation step inherent to this method. Ideally, optimisation should proceed steadily down the PES as indicated by the blue arrow.

do not generate gradient components along previous directions. The CG method typically has much better convergence characteristics than SD, however the gradient from the previous step must be stored but this is a trivial requirement for modern computers.

For most of the geometry optimisations carried out in this work (pseudo-) Newton-Raphson (NR) methods are used, which rely on a second order Taylor expansion of the energy. The major advantage of NR methods is that the convergence is second order near a stationary point *i.e.* convergence speeds up as the stationary point is approached. However, NR methods have some disadvantages. Firstly, the memory and computational requirements for NR methods are also larger than for SD, since the Hessian must be diagonalised and stored. Because it can be computationally very demanding to calculate the Hessian an updating scheme can be used instead *i.e.* pseudo-NR methods. If there is a negative term in the Hessian, the function value increases and the optimisation can end up at a saddle point. If one of the Hessian eigenvalues is close to zero, the geometry can go beyond the region where the Taylor expansion is valid. To mitigate these issues geometry optimisations are initiated using non-Newton-Raphson methods in this work.

3.4 The Variational Principle

For most purposes it is the ground state (*i.e.* lowest energy) solution to the time independent Schrödinger equation that is of interest, the problem is how to improve the approximate Ψ or even to know if one is improving it. Through application of the variational principle, an upper bound for the exact ground state energy (E_{gs}) can be obtained. For any normalised Ψ (which satisfies appropriate boundary conditions):

$$E_{gs} \leq \langle \Psi | H | \Psi \rangle \equiv \langle H \rangle \tag{3.6}$$

i.e. the expectation value of the Hamiltonian, $\langle H \rangle$, is an upper bound for the exact ground state. The energy of the approximate wavefuction is always too large, thus the quality of a wavefunction can be assessed by its energy: a better wavefunction has a lower energy. Thus if you have a wavefunction with many adjustable parameters, the parameters can be optimised to get the lowest possible energy, *i.e.* the best wave function.

3.5 Density Functional Theory

Density functional theory (DFT) seeks to replace the extraordinarily complex N-electron wavefunction with its dependence on $3N$ spatial and N spin coordinates at the heart of the Schrödinger equation with a simpler quantity, the electron density, $\rho(r)$ dependent on 3 spatial coordinates:

$$\rho(r) = N \int ... \int |\psi(x_1, x_2, ..., x_N)|^2 ds \; dx_2 ... dx_N \tag{3.7}$$

The electron density is an integral over all the spin coordinates (s) and the spatial coordinates (r) of all but one electronic coordinate (Equation 3.7). The electron density is in fact a probability density; while all the other electrons have arbi-

trary spin and position, it determines the probability that any of the electrons (with arbitrary spin) can be found within a volume element dr. Following the literature, $\rho(r)$ is hereafter referred to as the electron density. In this section a basic discussion of DFT will be outlined, including the Hohenberg-Kohn theorems, the Kohn-Sham approach and approximations to the exchange and correlation functional.

3.5.1 Hohenberg-Kohn Theorems

Modern DFT was introduced by Hohenberg and Kohn in their 1964 paper [3] and the theorems therein are the basis of DFT, here the important points of these theorems are presented; for the proofs of the theorems see ref. [3]. The first Hohenberg-Kohn theorem, the existence theorem, is concerned with the very heart of DFT; can the N-electron wave function be replaced by the electron density which uniquely defines the system? The theorem proves that the ground state electron density determines the external potential (V_{ext}) of a system to within an additive constant. As a result the Hamiltonian operator of the system, and consequently all other properties (*e.g.* the energy), is uniquely determined by its electron density $\rho(r)$.

The second Hohenberg-Kohn theorem, the variation principle, is concerned with establishing that a certain density is the true ground state density. The proof makes use of the variational principle discussed in the previous section. The individual components of the ground state energy must be functionals of the density, as is the total energy from the Hohenberg-Kohn existence theorem. When the external potential results entirely from the nuclear attraction, the ground state energy $E_0[\rho_0]$ can be partitioned as:

$$E_0[\rho_0] = T[\rho_0] + E_{ee}[\rho_0] + E_{ne}[\rho_0]. \tag{3.8}$$

The contributions to the total energy can be conveniently spilt between those which depend on the system at hand, *i.e.* E_{ne} and those which are universally valid independent of the nuclear charge and N. E_{ne} is system dependent while the first and second terms of Equation 3.8 are universally valid and collectively make up the Hohenberg-Kohn functional F$[\rho(r)]$:

$$F[\rho(r)] = T[\rho(r)] + J[\rho(r)] + E_{ncl}[\rho(r)]. \tag{3.9}$$

The Hohenberg-Kohn functional contains the contributions to the total energy due to the kinetic energy T, the classical Coulomb interaction J and non-classical part of the potential energy resulting from correlation E_{ncl}, and is valid for any external potential V_{ext} and any number of particles. The energy functional (3.8) for a given potential V_{ext} is:

$$E[\rho] = \int V_{ext}\rho(r)dr + F[\rho]. \tag{3.10}$$

The second Hohenberg-Kohn theorem proves that the calculated energy (3.10) is an upper bound for the ground state energy and only equals the ground state energy when ρ is the true ground state density.

3.5.2 The Kohn-Sham Approach

The Kohn-Sham approach [4] seeks to compute as much of the true kinetic and exchange and correlation energy as possible exactly and then deal with what is left approximately. The Kohn-Sham ground state density can be represented by a Slater determinant [5]. The resulting spin orbitals φ_i are usually referred to as the Kohn-Sham orbitals and are determined by:

$$f_{ks}\varphi_i = \varepsilon_i\varphi_i, \tag{3.11}$$

where f_{ks} is the one electron Kohn-Sham operator.

The Kohn-Sham orbitals are connected to the real system by ensuring that the moduli of the squared orbitals $\{\varphi_i\}$ is exactly the ground state density $\rho_0(r)$:

$$\rho_s(r) = \sum_i^N \sum_s |\varphi_i(r,s)|^2 = \rho_0(r). \tag{3.12}$$

This condition is imposed by correct choice of the external potential.

The exact kinetic energy of the non-interacting system T_s with the same density as the real system can be calculated using the Kohn-Sham orbitals:

$$T_s = -\frac{1}{2}\sum_i^N \langle\varphi_i|\nabla^2|\varphi_i\rangle \tag{3.13}$$

That T_s is not equal to the real kinetic energy is accounted for by the reformulation of 3.9:

$$F[\rho(r)] = T_s[\rho(r)] + J[\rho(r)] + E_{xc}[\rho(r)] \tag{3.14}$$

The exchange and correlation functional E_{xc} is introduced in 3.14. The part of the real kinetic energy not in T_s is combined with the non-classical electrostatic contributions to yield this functional, *i.e.* all terms which cannot be exactly computed are contained within E_{xc}.

To minimise the energy of the system with the constraint that the orbitals are orthonormal the following condition must be fulfilled:

$$\begin{aligned}\left(-\frac{1}{2}\nabla^2 + \left[\int \frac{\rho(r_2)}{r_{12}} dr_2 + V_{xc}(r_1) - \sum_A^M \frac{Z_A}{r_{1A}} \right] \right)\varphi_i \\ = \left(-\frac{1}{2}\nabla^2 + V_{eff}(r_1) \right)\varphi_i = \varepsilon_i \varphi_i.\end{aligned} \tag{3.15}$$

The Kohn-Sham one-electron equation (Equation 3.15) must be solved iteratively, since V_{eff} depends on the density through the Coulomb term and V_{xc}.

In principle the Kohn-Sham approach is exact; if the exact forms of V_{xc} and E_{xc} were known, the Kohn-Sham approach would lead to the exact total energy, *i.e.* the correct eigenvalue in the many-electron Schrödinger equation. Of course, the form of E_{xc} and hence V_{xc} is not known and is approximated when DFT is used, achieving better approximation to the exchange and correlation functional is an important focus of DFT research. As a further complication, the variation principle no longer strictly holds when approximations are made to E_{xc}.

3.5.3 Approximations to the Exchange and Correlation Functional

As already touched on, the accuracy of DFT depends on how well the exchange and correlation functional E_{xc} can be approximated. The exact form of E_{xc} is unknown and there is no systematic approach to achieving improved approximations. The only real guidance available is the sum rules for the exchange-correlation hole (which can be further split into the Fermi and Coulomb holes) [6]:

- The exchange-correlation hole contains the charge of one electron.
- The Fermi hole is negative everywhere and also integrates to -1.
- The Coulomb hole over all space has no charge but has both positive and negative regions.

While these rules give some ideas of how the functional should be constrained, it is also the case that functionals which do meet these requirements are not always better than those which do not.

The simplest approximation to the E_{xc} is the local density approximation (LDA). It is based on the uniform electron gas, a hypothetical charge neutral

system in which electrons of constant density move on a uniform positive background. While the uniform electron gas is very different to any realistic atoms or molecules which have rapidly varying densities, it is the only system for which an accurate exchange and correlation energy functional is known. The LDA E_{xc} is then:

$$E_{xc}^{LDA}[\rho] = \int \rho(r)\varepsilon_{xc}[\rho(r)]dr, \tag{3.16}$$

where $\varepsilon_{xc}[\rho(r)]$ is the exchange-correlation energy per electron for the uniform electron gas. The LDA can easily be extended to the unrestricted and spin polarised cases by splitting $\rho(r)$ into two spin densities, $\rho_\alpha(r)$ and $\rho_\beta(r)$. The LDA gives surprisingly good results for structures while systemically overestimating atomisation energies which results in overbinding. To achieve sufficient accuracy in many applications, more sophisticated approximations to E_{xc} are necessary.

The LDA is based on the uniform electron gas, but in real systems the electron density varies rapidly. One approach towards a more accurate functional consequently seeks also to include the gradient of the density in E_{xc}. The LDA can be viewed as the first term in a functional Taylor expansion and one can then seek to obtain better results by introducing the second term. This leads to the gradient expansion approximation (GEA), which in many cases actually performs worse than the LDA. By enforcing the sum rules outlined above on the GEA, generalised gradient approximations (GGA) are obtained, which offer improved performance with respect to the LDA. There are many different GGA functionals (*e.g.* BLYP[7, 8], PW91 [9], PBE [10]) but results of similar quality are generally obtained for all such functionals [6].

The most accurate functionals in terms of energetics are hybrid functionals. Such functionals combine exact exchange and gradient corrected exchange and

correlation in specific ratios, for example the hybrid function of Becke [11]:

$$E_{xc} = E_{XC}^{LSDA} + a_0(E_X^{exact} - E_X^{LSDA}) + a_x\Delta E_x^{B88} + a_c\Delta E_C^{PW91} \tag{3.17}$$

where ΔE_x^{B88} [7] and E_C^{PW91} [9] are gradient corrections to LSDA exchange and correlation, respectively. The coefficients (a_0, a_x, a_c) are determined by fitting to experimental data and thus the hybrid functional is semi-empirical. The most widely used hybrid functional is B3LYP, which replaces the Perdew-Wang correlation functional in Equation 3.17, E_c^{PW91}, by that of Lee, Yang and Parr [8].

3.6 Basis Sets

A set of functions which can be used to construct an unknown function is called a basis set and can be used to represent the wave function or electron density in electronic structure calculations. The use of basis sets is an approximation because basis sets used in actual calculations are not complete (such a basis set would necessitate an infinite number of basis functions). In this section plane waves and localised atomic (or atom-like) orbital (AO) basis functions, which are the most widely used basis functions in DFT, will be discussed.

3.6.1 Plane Waves

Modelling extended systems such as crystalline materials typically uses a unit cell with periodic boundary conditions. Such "infinite" systems suggest also using basis functions with infinite range (as opposed to localised AO based basis functions). In the case of a metal, the outer valence electrons behave as nearly free electrons which suggests using solutions to the Schrödinger equation for free electrons as a basis. For infinite systems, the energy spacing between molecular orbitals disappears and bands are formed. Electrons in bands can then be

described by a basis set of plane waves in three dimensions:

$$\chi(r) = e^{i\vec{k}.\vec{r}}. \tag{3.18}$$

The number of plane waves used (k) is determined by the cut-off energy ($E_{cut} = \frac{1}{2}k^2$) and the number of basis functions can therefore be systematically increased by increasing the cut-off energy. Plane waves are ideal for describing delocalised, slowly varying electron density, however core electrons are strongly localised and valence electrons close to the core also oscillate rapidly. Describing the core region well then requires a large number of rapidly oscillating plane waves (and so a large cut-off energy). In practice pseudopotentials and projector augmented waves (discussed later in this chapter) can be used to describe the core region greatly reducing the number of plane waves required. While plane waves are suited to periodic systems, they can also be used to model finite systems provided a sufficiently large supercell is chosen such that the system does not interact with its periodic image. This is the approach taken in this work when the VASP program [12–15], which uses a plane wave basis, is used with finite structures.

3.6.2 Localised orbitals

Localised orbitals may be literal atomic orbitals or atom-like orbitals. The major difficulties associated with AOs is that, unlike plane waves, the orbitals must be chosen for a given system to be both efficient and accurate (*i.e.* there is no unique way to make a basis larger) and issues relating to over-completeness as basis set convergence is approached. The popularity of AO basis sets is due to the relatively small number of basis functions required, much smaller than plane waves, and hence their computational efficiency.

The most widely used localised basis functions consist of Gaussians multiplied by polynomials. Gaussian type orbitals (GTOs) have the general form:

$$\eta^{GTO}(r) = Nx^l y^m z^n exp[-\alpha r^2]. \tag{3.19}$$

N is the normalisation factor, α is the orbital exponent and determines the compactness of the orbital while $L = l + m + n$ classifies the orbital, *i.e.* $L = 0$ is s-type, $L = 1$ is p-type etc. The position r is measured relative to an atomic site for atom centred Gaussians. The popularity of Gaussians as a localised basis is due to their efficiency in calculations since multi-centre integrals can be evaluated analytically when Gaussians are used. Slater type orbitals (STOs) which are exponential functions, are typically approximated by sums of Gaussians and commonly used as basis functions because the computationally convenient properties of Gaussians are retained while their form is closer to that of an atomic-type orbital.

Localised orbitals can also be constructed within spherically symmetric potentials. The atomic orbitals themselves could be used, but they have long range tails which reduce accuracy in molecules and solids. Numerical orbitals are short range orbitals based on such atomic orbitals and are strictly localised within a given cut-off radius, eliminating numerically demanding long range tails. Numerical local orbitals are particularly suited to systems with many atoms in a simulation cell and which have large vacuum - precisely the systems to be studied in this work. In this thesis, we use the OpenMX code which implements numerical orbitals [16]. In particular, localised orbitals are essential for the non-equilibrium Green's function method (discussed later in this chapter) which we use for electron transport calculations.

3.7 Pseudopotentials and PAW

For many applications of computational methods the core electrons are unimportant but a large number of basis functions are required to expand the associated orbitals increasing the computational cost. This is especially severe for later elements in the periodic table which have a large number of core electrons. The fundamental idea of the pseudopotential (PP) is to replace the effects of the core electrons and the Coulomb potential of the nucleus by an effective potential which acts on the valence electrons. There are many ways to generate PPs, here only those used in this work (norm-conserving PPs and ultra-soft PPs) will be discussed. The projector augmented wave (PAW) method, which is an alternative to PPs (used in this work by the VASP code) is also introduced.

Though the PP concept has a long history, it is the norm-conservation condition that enabled accurate, transferable PPs to be constructed. It is essential that PPs be transferable so that they can be constructed in one environment (typically an atom) and then used in other environments (ions, molecules etc.) to correctly describe valence properties. Hamann, Schülter and Chiang give the requirements for a good (*i.e.* accurate and transferable) *ab initio* PP [17]:

1. The all electron and pseudo valence eigenvalues are in agreement for a chosen reference atomic configuration

2. The all electron and pseudo valence wave functions are in agreement beyond a chosen core radius (r_c)

3. The integrated charge densities inside r_c are the same for the all electron and pseudo charge densities (norm conservation)

4. The logarithmic derivatives of the all electron and pseudo wave function agree for $r > r_c$, as do their first energy derivatives

While imposing norm conservation leads to accurate and transferable PPs, there is still the problem of the smoothness of the PP (fewer basis functions can be used with a smooth PP). The difficulty is the conflicting requirements of a small r_c required for accuracy and transferability (a "hard" PP) while a smooth pseudofunction necessitates a large r_c (a "soft" PP). Ultrasoft PPs [18] seek to solve this conflict by relaxing the norm-conservation condition which enables a much larger r_c to be chosen than for a norm-conserving PP, while still maintaining accuracy and transferability.

Although the norm-conserving and ultrasoft pseudopotentials are suitable for most DFT calculations, some properties cannot be calculated without the full wave function which is lost when these PPs are employed. The PAW method [19] offers an alternative to these PP techniques, reducing the number of basis functions needed while still retaining information on the wave function in the core region. Close to the core, the wave function oscillates rapidly, while in the bonding region it is smooth, it is these oscillations which greatly increase the number of plane wave basis functions needed and hence the computational load. The PAW method replaces the all-electron wave function by an auxiliary smooth wave function. Far from the nucleus, the wave function becomes smooth (*i.e.* the region of the valence electrons) and so only the wave function close to the core, where it is not smooth (*i.e.* inside the "augmentation sphere") is augmented using auxillary partial waves and projectors.

3.8 Electron Localisation Function

The electron localisation function (ELF) identifies localised electrons in atomic and molecular systems and is used to visualise chemical bonding. It was introduced by Becke and Edgecombe in 1990 [20]. The ELF was originally formulated for use with the Hartree-Fock method and was extended to DFT in 1992 by

Savin and co-workers [21]. The basic idea behind the ELF is that the electron pair probability ($P^{\sigma\sigma}_{cond}$) can be used as a gauge for electron localistion. If an electron of spin σ is known to be located at position A (the reference point), then the conditional probability of finding another electron (also of spin σ) at postion B can be calculated. By consideration of the Pauli exclusion principle, the probabilty of the second electron also being at position A must be 0, while the total conditional probability is one less than the total number of σ electrons.

Consideration of $P^{\sigma\sigma}_{cond}$ as a method to examine bonding is long established (a summary of these efforts is given in ref [22]). Becke and Edgecombe realised that useful information about electron localisation can be obtained from short range behaviour as B approaches A. In this case, the second term of the spherically averaged conditional pair probability ($P^{\sigma\sigma}_{cond}(A,s)$ - where s is the separation of A and B) is important,

$$P^{\sigma\sigma}_{cond}(A,s) = \frac{1}{3}\left[\tau_\sigma - \frac{1}{4}\frac{(\nabla\rho_\sigma)^2}{\rho_\sigma}\right]s^2 + ... \tag{3.20}$$

where τ_σ is the positive definite kinetic energy density and ρ_σ is the density. The electron localisation is related to the size of the term in square brackets in Equation 3.20, (D_σ); if D_σ is small the electron at A is localised. D_σ is not bounded from above and is inversely related to localisation, while Becke and Edgecombe wanted a bounded value which was directly related to localisation.

Therefore, Becke and Edgecombe defined the ELF such that $0 \leq ELF \leq 1$ by scaling with a suitable uniform electron gas and a large ELF corresponds to high localisation:

$$ELF = \left(1 + \left(\frac{D_\sigma}{D^0_\sigma}\right)^2\right)^{-1}, \tag{3.21}$$

where D^0_σ is a uniform electron gas with the same spin density as D_σ. The upper limit of the ELF is 1 and this corresponds to perfect localisation, while an ELF

value of 0.5 is equivalent to an electron-gas like pair probability.

3.9 Non-Equilbrium Green's Function Method

In this thesis, the non-equilibrium Green's function (NEGF) method is used to calculate electronic transmission, electron current and conductivity, as well as to generate current-voltage characteristics. A brief summary of the method for electronic transport calculations is given here; full details of this method can be found in the literature, *e.g.* ref. [23] and more specifically the OpenMX implementation is described in ref. [24]. The infinite one-dimensional system studied using NEGF is shown in Figure 3.2 and consists of central region C_0 and cells L_i and R_i arranged semi-infinitely along the a-axis, with periodicity along the b- and c-axes. While the cells L_i and R_i need not be the same, all L_i cells must be identical to one another, as must all R_i cells. Each L_i is then one repeat unit of the left lead and each R_i one repeat unit of the right lead.

When the chemical potential is constant throughout the system (*i.e.* the equilibrium state), DFT can be used to compute the electronic structure. The system can be represented by a KS matrix equation arising from the use of an atomic orbital expansion

$$H\vec{c} = \varepsilon S\vec{c}, \tag{3.22}$$

where $\vec{c}$ is a column vector of AO coefficients, ε is the eigenvalue, and H and S are the Hamiltonian and overlap matrices, respectively; the overlap matrix results from the non-orthogonality of the AO basis functions.

In the NEGF calculation, the central region C_0 is extended by including one repeat unit of each lead so that electronic structure in the interface regions can relax. In addition, two conditions are imposed:

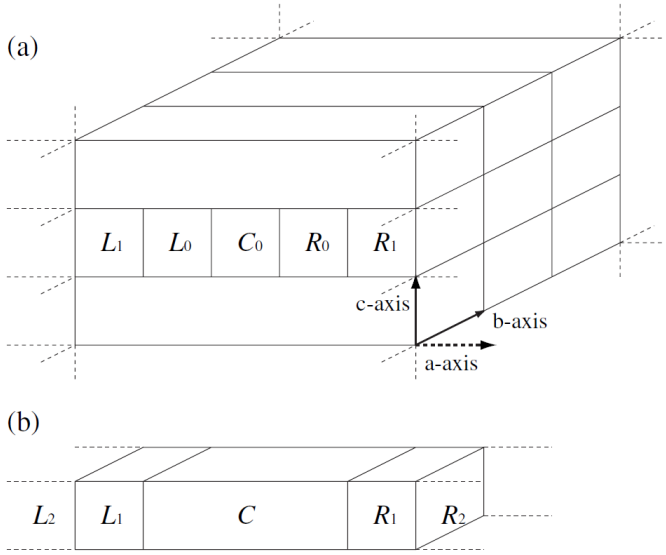


Figure 3.2: (a) Schematic of the system to be studied with the NEGF method. Infinite left (L_i) and right (R_i) leads and a central scatterer (C_0) are along the a-axis, with periodicity on the bc place. (b) is the one-dimensional system created by consideration of the periodic boundary condition in the bc plane and extension of the region around C_0 to include the first repeat unit of the left and right leads within the region C. Figure taken from ref. [24].

1. The basis orbitals in the central region C_0 overlap with those in L_0 and R_0 but must not overlap with those in L_1 and R_1.

2. The basis orbitals in L_i and R_i must not overlap lap with basis orbitals beyond the nearest neighbour cells.

These two conditions can be trivially satisfied by adjusting the size of the L_i and R_i unit cells because of the strictly localised AOs used. With these two conditions satisfied, the Hamiltonian matrix in equation 3.22 can be written in block tridiagonal form and the Green's function G can be defined as:

$$G(Z)(ZS - H) = I \tag{3.23}$$

where Z is a complex energy.

The Green's function of region C in Figure 3.2 is then given by:

$$G_C(Z) = [ZS_C - H_C - \Sigma_L(Z) - \Sigma_R(Z)]^{-1} \tag{3.24}$$

where $\Sigma_L(Z)$ and $\Sigma_R(Z)$ are the lead self-energies and are defined by:

$$\Sigma_L(Z) = (ZS_{CL_1} - H_{CL_1})G_L(Z)(ZS_{L_1C} - H_{L_1C}) \tag{3.25}$$

for the left lead with a similar equation for the right lead. The self-energies encompass the effect of the semi-infinite leads on the region C. The lead self-energies include the surface Green's function of the lead region, which are evaluated using an iterative method. The equilibrium Green's function method is extended to the non-equilibrium case - where the chemical potential is not uniform throughout the system - by modification of the equilibrium electron density. The spin resolved transmission $T_\sigma(E)$ can then be calculated within the Landauer formalism:

$$T_\sigma(E) = \frac{1}{V_c}\int_{BZ} dk^3 T_\sigma^{(k)}(E), \tag{3.26}$$

where V_c is the volume of the cell and $T_\sigma^{(k)}$ is the spin and k-resolved transmission:

$$T_\sigma(E)^{(k)} = Tr[\Sigma_{\sigma,L_1}^{(k)}(E)G_{\sigma,C}^{(k)}(Z)\Sigma_{\sigma,R_1}^{(k)}(E)G_{\sigma,C}^{(k)}(Z)]. \tag{3.27}$$

The current (I_σ) can then be evaluated using the transmission formula:

$$I_\sigma = \frac{e}{h}\int dE\, T_\sigma(E)\Delta f(E), \tag{3.28}$$

where $\Delta f(E)$ is the difference in the Fermi function between the left and right leads.

3.10 References

[1] E. Schrödinger. An Undulatory Theory of the Mechanics of Atoms and Molecules. *Physical Review*, 28:1049–1070, 1926.

[2] M. Born and R. Oppenheimer. Zur Quantentheorie der Molekeln. *Annalen Der Physik*, 389:457–484, 1927.

[3] P. Hohenberg and W. Kohn. Inhomogeneous Electron Gas. *Physical Review*, 136:B864–B871, 1964.

[4] W. Kohn and L.J. Sham. Self-Consistent Equations Including Exchange and Correlation Effects. *Physical Review*, 140:A1133–A1138, 1965.

[5] J.C. Slater. The Theory of Complex Spectra. *Physical Review*, 34:1293–1322, 1929.

[6] W. Koch and F.C. Holthausen. *A Chemist's Guide to Density Functional Theory*. Wiley-VCH, 2001.

[7] A.D. Becke. Density-Functional Exchange-Energy Approximation with Correct Asymptotic Behavior. *Physical Review A*, 38:3098–3100, 1988.

[8] C. Lee, W. Yang, and R.G. Parr. Development of the Colle-Salvetti Correlation-Energy Formula into a Functional of the Electron Density. *Physical Review B*, 37:785–789, 1988.

[9] J.P. Perdew, J.A. Chevary, S.H. Vosko, K.A. Jackson, M.R. Pederson, D.J. Singh, and C. Fiolhais. Atoms, Molecules, Solids, and Surfaces - Applications of the Generalized Gradient Approximation for Exchange and Correlation. *Physical Review B*, 46:6671–6687, 1992.

[10] J.P. Perdew, K. Burke, and M. Ernzerhof. Generalized Gradient Approximation Made Simple. *Physical Review Letters*, 77:3865–3868, 1996.

[11] A.D. Becke. Density-Functional Thermochemistry. III. The Role of Exact Exchange. *Journal of Chemical Physics*, 98:5648–5652, 1993.

[12] G. Kresse and J. Hafner. *Ab Initio* Molecular Dynamics for Liquid-Metals. *Physical Review B*, 47:558–561, 1993.

[13] G. Kresse and J. Hafner. *Ab Initio* Molecular-Dynamics Simulation of the Liquid-Metal Amorphous-Semiconductor Transition in Germanium. *Physical Review B*, 49:14251–14269, 1994.

[14] G. Kresse and Furthmüller. J. Efficient Iterative Schemes for *Ab Initio* Total-Energy Calculations using a Plane-Wave Basis Set. *Physical Review B*, 54:11169–11186, 1996.

[15] G. Kresse and D. Joubert. From Ultrasoft Pseudopotentials to the Projector Augmented-Wave Method. *Physical Review B*, 59:1758–1775, 1999.

[16] T. Ozaki. Variationally Optimized Atomic Orbitals for Large-Scale Electronic Structures. *Physical Review B*, 67:155108, 2003.

[17] D.R. Hamann, M. Schlüter, and C. Chiang. Norm-Conserving Pseudopotentials. *Physical Review Letters*, 43:1494–1497, 1979.

[18] D. Vanderbilt. Soft Self-Consistent Equations in a Generalized Eigenvalue Formalism. *Physical Review B*, 41:7892–7895, 1990.

[19] P.E. Blöchl. Projector Augmented-Wave Method. *Physical Review B*, 50:17953–17979, 1994.

[20] A.D. Becke and K.E. Edgecombe. A Simple Measure of Electron Localization in Atomic and Molecular-Systems. *Journal of Chemical Physics*, 92:5397–5403, 1990.

[21] A. Savin, O. Jepsen, J. Flad, O.K. Andersen, H. Preuss, and H.G. von Schnering. Electron Localization in Solid-State Structures of the Elements: the Diamond Structure. *Angewandte Chemie International Edition*, 31:187–188, 1992.

[22] A. Savin, R. Nesper, S. Wengert, and T.F. Fässler. ELF: The Electron Localization Function. *Angewandte Chemie International Edition*, 36:1808–1832, 1997.

[23] S. Datta. *Electronic Transport in Mesoscopic Systems*. Cambridge University Press, Cambridge, 1997.

[24] T. Ozaki, K. Nishio, and H. Kino. Efficient Implementation of the Nonequilibrium Green Function Method for Electronic Transport Calculations. *Physical Review B*, 81:035116, 2010.

Chapter 4

Nitrogen Doped Carbon Nanotube Growth Mechanism

4.1 Introduction

Realising the potential of CNTs for many applications requires control over CNT electronic properties at the growth stage, which is currently lacking. Doping of CNTs is an alternative route to controlling CNT electronic properties [3, 4]. Suitable dopants should be incorporated into the CNT lattice without causing excessive disruption to minimise deterioration in electronic properties due to electron scattering at defects. This suggests that the dopant atom should be a similar size to the carbon atom which makes nitrogen an obvious dopant candidate [5]. As well as being incorporated directly into the CNT lattice as a substitutional dopant whereby one nitrogen atom replaces one carbon atom, nitrogen can also be incorporated in a pyridine-like fashion where nitrogen bonds only to two carbon atoms, as in the aromatic pyridine molecule [6]. The level of nitrogen dopants in CNTs reported in the literature is consistently high and ranges from 1-20 atom % [7] and such doped CNTs are reported exclusively to grow with a bamboo structure [3, 7–15].

Chemical vapour deposition (CVD) growth of CNTs occurs in a similar way for single-walled (SWNTs), multi-walled (MWNTs) and bamboo (BCNTs) carbon

nanotubes. A feedstock gas is cracked by a transition metal nanoparticle catalyst, which acts as a support for further growth. The nanoparticle catalyst plays a crucial role in CNT growth. Firstly, the CNT diameter is determined by the size of the nanoparticle catalyst [16]. Secondly, the strength of the metal-carbon bond has a critical role as the binding energy obeys a "Goldilocks" criterion. If the binding energy is too low, the nascent CNT cap cannot be stabilised on the catalyst and no CNT results, on the other hand if the binding is too high a metal carbide is preferentially formed on the catalyst surface. However, if the binding energy is in a window between these two extremes, CNT growth can occur [17–20].

The precise details of the growth mechanism differ in a crucial way for BCNTs. When SWNTs and MWNTs grow, the catalyst continuously cracks the carbon source and the CNT grows without interruption until the catalyst is poisoned or the supply of feedstock gas is stopped. When BCNTs grow, graphitic carbon layers found in the nanotube cap bind more strongly to the catalyst surface; such an effect is also seen with alloy catalysts [19, 20]. As growth progresses, the molten metal nanoparticle elongates until the nanoparticle surface energy is no longer counteracted by the stabilisation due to binding to the CNT inner shell and the nanoparticle retracts to a lower surface energy state [21] at which point a graphitic carbon layer then grows across the surface of the catalyst. This elongation process is continually repeated, resulting in the formation of the characteristic BCNT chambers. The binding energy of nitrogen doped CNTs is calculated using density functional theory and by comparison to similar calculations for undoped CNTs [17, 18], it is determined that nitrogen binds more strongly to cobalt than carbon. By consideration of the results of these simulations in conjunction with experimental results, the origin of the typical nitrogen-doped CNT bamboo structure is explained.

4.2 Methods

The ability of a Co nanoparticle to stabilize the growing end of a nitrogen-doped CNT was investigated by calculating the binding energy of (3,3), (5,0), (5,5) and (10,0) SWNTs adhering to Co clusters of suitable diameter. Calculated binding energies ΔE are compared to binding energies previously reported for undoped CNTs [17, 18]. In each case the CNT contains one substitutional nitrogen dopant representing doping of 1.7 to 3.5 atom %, comparable to dopant concentrations reported in the literature. The binding energies have been calculated within density functional theory (DFT) using the VASP program [22–25]. The projector augmented wave (PAW) method was used [26], along with the Perdew-Wang formulation of the generalised gradient approximation (GGA) exchange and correlation functional [27]. A plane wave cut-off energy of 400 eV was used for the relaxation of the nanotube systems, followed by a single-point calculation with a 500 eV cut-off energy. The simulation box for (3,3) CNT and (3,3)-Co_{13} complex was 10 x 10 x 20 $Å^3$, for (5,0) CNT and (5,0)-Co_{13} complex was 10 x 10 x 30 $Å^3$ and was 15 x 15 x 30 $Å^3$ for (5,5) CNT, (5,5)-Co_{55} complex, (10,0) CNT and (10,0)-Co_{55} complex. For the smaller systems a Gaussian smearing of 0.05 eV was used, while the Methfessel-Paxton scheme [28] was used for the Co_{55} systems to aid convergence to the ground state solution. Spin-polarised calculations were performed in all cases and the structures were relaxed without symmetry constraints. The experimental portion of the work performed in conjugation with the theoretical analysis presented here is described in ref. [29]; CVD was used to grow CNTs which were analysed using Raman spectroscopy, transmission electron microscopy and X-ray photoelectron spectroscopy.

4.3 Simulated Structures

The optimised structures for the nanoparticle-CNT complexes with a dopant nitrogen atom bonding directly to the nanoparticle ("Layer 1") are shown in Figure 4.1. The bond lengths at the interface are not strongly affected by the introduction of the nitrogen dopant, which is expected given the similar sizes of the nitrogen and carbon atoms. In all cases, the Co-N bond is slightly longer than Co-C (∼1%), while the C-N bond is slightly shorter than the C-C bond (∼2%). To simulate continued growth of a CNT after introduction of a dopant atom, we move the nitrogen atom away from the interfaces to Layers 2, 3 and 4 as indicated in Figure 4.1 and re-optimise the geometry of the structure, calculating the binding energy in each case.

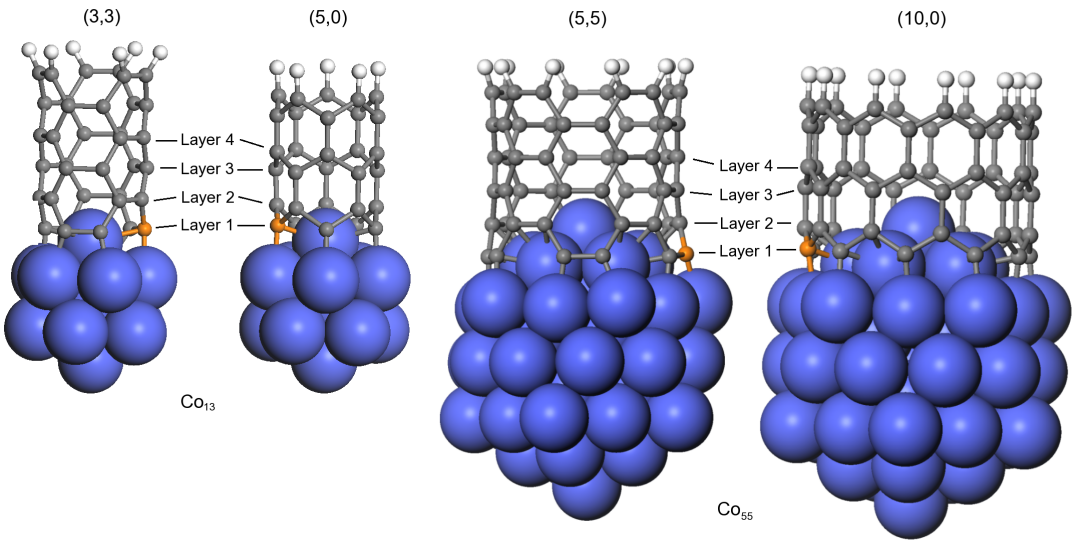


Figure 4.1: Structures of the (3,3) and (5,0) nanotubes bound to a Co_{13} metal cluster and the (5,5) and (10,0) nanotubes bound to a Co_{55} metal cluster with a nitrogen atom substituting a carbon atom in Layer 1 in each case. Layer 2, Layer 3 and Layer 4 dopant positions are as indicated. The Co atoms are coloured blue, C grey, H white and N orange.

The bonds between the CNT and the nanoparticle are highly directional. The C atoms at the CNT edge are typically close to two Co atoms, one is below the C atom at a similar angle to C in the next CNT layer if the CNT were continued

instead of terminating at the metal nanoparticle and one is behind the C atom inside the CNT. However C atoms at the CNT edge bond only to the atom below them in the nanoparticle and not to the Co atom behind them, even though the distance from the CNT edge to both Co atoms is similar. This is confirmed using the electron localisation function (ELF - described in detail in Section 3.8). An ELF of 1 corresponds to perfect localisation, while an ELF of 0.5 corresponds to electron-gas-like pair probability. A high ELF value therefore corresponds to localised electrons, such as those in covalent bonds and electron lone pairs.

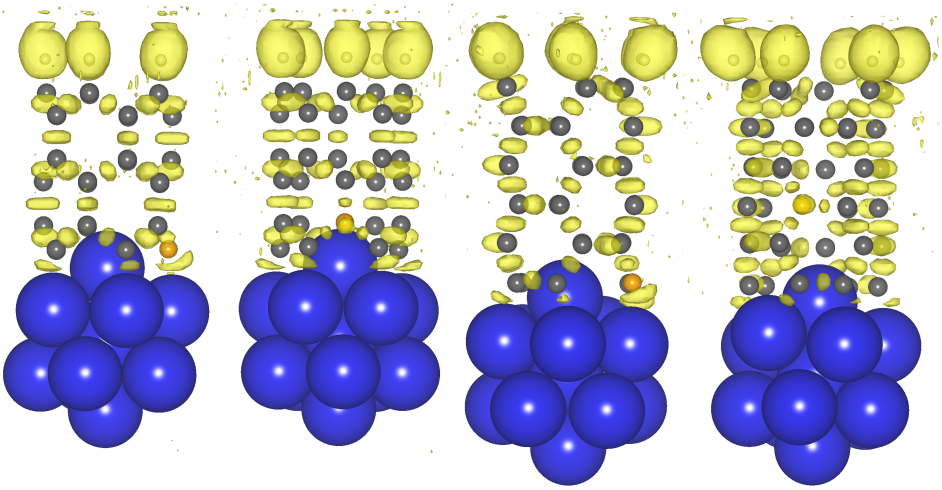


Figure 4.2: 0.7 isosurfaces (in yellow) of the ELF, indicating regions of localised electrons. From Left to Right: (5,0)-complex with N in Layer 1, (5,0)-complex with N in Layer 2, (3,3)-complex with N in Layer 1 and (3,3)-complex with N in Layer 3. The Co atoms are coloured blue, C grey, H white and N orange.

The 0.7 isosurface of the ELF for the (5,0)- and (3,3)-complexes are shown in Figure 4.2. It is clear that each interface CNT atom bonds covalently to the nanoparticle via a single bond to the Co atom below it. Thus there are 5 CNT-Co bonds at the (5,0)-complex interface, 6 at the (3,3)-complex interface and 10 bonds at the (10,0)- and (5,5)-complex interfaces, as discussed in the preceding section. The nitrogen lone pairs in all cases are directed outward from the CNT, which is as expected; due to the curvature of the CNT, this position minimises the repulsion between the electron lone pair and the electrons in the C-N/Co-N bonds.

4.4 Binding Energies

The binding strength of a CNT to a metal catalyst has previously been shown to be of extreme importance to successful catalysis and CNT growth [17–20, 30]. If this binding strength is too low growth will not occur, while if the binding is too strong carbon-carbon bond formation is less favourable and metal carbide formation occurs. We calculate the dissociation energies of N-doped CNT-metal complexes and thus calculate the binding energy ΔE per bond.

$$n\Delta E = E_{comp} - (E_{cluster} + E_{CNT}) \tag{4.1}$$

where E_{comp} is the total energy of the complex, $E_{cluster}$ is the total energy of the isolated metal nanoparticle, E_{CNT} is the total energy of the isolated CNT fragment and n is the number of CNT-cluster bonds at the interface, which is 5 for the (5,0)-complex, 6 for the (3,3)-complex and 10 for both the (10,0)- and (5,5)-complex, as discussed. We will compare these values to those previously reported in the literature for the undoped complexes.

In most cases the introduction of the nitrogen dopant in Layers 2-4 does not strongly affect the strength of the CNT-nanoparticle interaction; once the nitrogen dopant no longer bonds to the nanoparticle surface, it has minimal effect on the metal-CNT interface. However, in all Layer 1 cases the ΔE values are consistently less favourable than the equivalent undoped cases, which suggests that the metal-CNT interaction is in fact *weakened* by incorporation of nitrogen at the interface. This results from using the calculation of binding energies - the energy differences between the complexed nanotube and the isolated nanotube and cluster fragments *i.e.* dissociation energies - as a measure for bond strength. Consequently, any differences in the stabilisation of the individual tube and cluster fragments is also necessarily included in the calculated ΔE. Each sequence of nitrogen doped structures differs only in the position of the nitrogen atom and

Table 4.1: Total energies for all cobalt nanoparticle/CNT complexes and the corresponding unbound tube fragments with nitrogen replacing one carbon atom in Layer 1-4 (see Figure 4.1) and CNT binding energies ΔE. The total energy of the Co_{13} cluster and Co_{55} clusters are -66.90 eV and -329.09 eV respectively. The "Undoped" data are reproduced from Larsson *et al* [18].

	Co_{13}-(3,3)			Co_{13}-(5,0)		
	E_{CNT} (eV)	E_{comp} (eV)	ΔE (eV)	E_{CNT} (eV)	E_{comp} (eV)	ΔE(eV)
Layer 1	-326.55	-403.86	-1.74	-264.46	-345.57	-2.84
Layer 2	-324.58	-403.24	-1.96	-263.00	-345.24	-3.07
Layer 3	-324.62	-402.99	-1.91	-262.87	-345.19	-3.08
Layer 4	-324.66	-403.05	-1.91	-262.69	-345.35	-3.15
Undoped	-326.32	-404.19	-1.87	-264.27	-346.21	-3.02

	Co_{55}-(5,5)			Co_{55}-(10,0)		
	E_{CNT} (eV)	E_{comp} (eV)	ΔE (eV)	E_{CNT} (eV)	E_{comp} (eV)	ΔE(eV)
Layer 1	-558.69	-904.44	-1.67	-548.61	-905.13	-2.74
Layer 2	-556.82	-903.42	-1.75	-546.91	-904.42	-2.84
Layer 3	-556.78	-903.57	-1.77	-545.47	-904.07	-2.95
Layer 4	-556.73	-903.35	-1.75	-546.37	-904.20	-2.87
Undoped	-558.39	-905.07	-1.76	-549.53	-905.35	-2.67

the total energies of the complexes E_{comp} can be directly compared for a given chirality in this case. As seen in E_{comp}, the incorporation of nitrogen at the interface strengthens the metal-CNT interaction; the total energy of the Layer 1 complexes are consistently lower than the corresponding Layer 2-4 energies. The Layer 1 complex is 0.62 eV lower in energy for the (3,3)-complex and 0.33 eV, 1.12 eV and 0.71 eV lower for the (5,0)-, (5,5)- and (10,0)-complexes, respectively.

In the case of the Layer 1 ΔE, the stronger binding in the complexes is counteracted by a large fragment stabilisation of the Layer 1 dissociated tubes (Figure 4.3), where the nitrogen atom bonds only to two other atoms, as opposed to three other atoms in the Layers 2-4 nanotube fragments. The Layer 1 total energies for the nanotube fragment (E_{CNT}) are 1.97 eV, 1.46 eV, 1.87 eV and 1.70 eV lower than the corresponding Layer 2 fragments for (3,3), (5,0), (5,5) and (10,0) nanotubes, respectively. The fragment stabilisation energies for the dissociated nanotube fragments are larger than the decrease in the Layer 1 complex energies

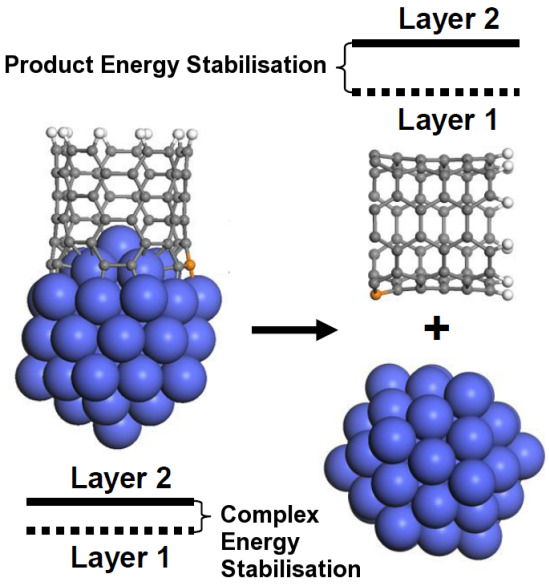


Figure 4.3: Energy levels showing the relative stabilities of nitrogen in Layer 1 compared to Layer 2 for the Co_{55}-(5,5) complex (left) and the dissociated products (right). The stabilisation of the dissociated products is much larger when nitrogen is in Layer 1 than in Layer 2 which is due to the difference in the N-doped tube fragment. This effect results in the smaller dissociation energy for Layer 1 even though the CNT bonds more strongly in this case, which is evident in the total energies of the complexes. Co atoms coloured blue, C grey, H white and N orange.

relative to Layer 2. Therefore, while the Layer 1 complex is lower in energy than the Layer 2 complex, the dissociated Layer 1 products are lower still in energy than those for Layer 2. These differences in relative energies are shown schematically in Figure 4.3 for the case of Co_{55}-(5,5). Compared to Layer 2, the "product energy stabilisation" is always larger than the "complex energy stabilisation" for nitrogen in Layer 1 due to the difference in the environment of the nitrogen in the tube fragments. The nitrogen in Layer 1 is in a very stable environment on the tube edge bonded to only two other atoms, *i.e.* a pyridine-like environment. Thus a nitrogen atom on the tube edge decreases the dissociation energy, which is reflected in the calculated binding energies. The strongest binding of the CNT to the metal therefore occurs when nitrogen bonds directly to the metal, as reflected in the E_{comp} values in Table 4.1.

4.5 Analysis of the Growth Mechanism

Typical SWNT and MWNT growth can be conveniently divided into three distinct stages. During the first stage graphitic carbon "flakes" form a cap on the surface of the catalyst which increases the stability of the nanoparticle surface atoms. Growth enters stage two with elongation of the catalyst due to this stabilisation in conjunction with deposition of carbon at the cap edge. As the nanoparticle elongates, metal-metal bonds are lost in favour of more and more surface atoms, which are stabilised by the cap and sidewalls of the nascent CNT. At some point, the stabilisation of the metal surface atoms by the innermost carbon layer no longer counteracts the increase in surface energy of the elongated nanoparticle and the nanoparticle contracts to a more stable spherical shape. After this contraction, growth enters a third phase with carbon from the nanoparticle added to the nanotube growth edge and the growth of a typical hollow CNT occurs. The CNT growth mechanism is illustrated schematically in Figure 4.4. When nitrogen is introduced during CNT growth, this third growth phase is not attained. Instead, the first two stages of growth continually repeat leading to formation of a bamboo CNT.

High resolution transmission electron microscopy (HRTEM) images (Figure 4.5) show that nitrogen-doped CNTs adopt a bamboo structure. The number of carbon layers in the bamboo CNT chambers differ through the chamber - at the chamber tip there are a larger number of layers than at the base. The bamboo CNTs imaged have 12 carbon layers in the tip, 20 carbon layers in the sidewall near the tip while at the base of the chamber there are typically 7 carbon layers. Previous *in situ* TEM studies have shown the the number of layers in a nanotube structure is related to the time the metal catalyst nanoparticle is resident at that position in the structure [21, 31]. It is the bamboo CNT structure that forms instead of the more crystalline MWNT structure when nitrogen is introduced at the growth stage due to the greater binding of nitrogen doped

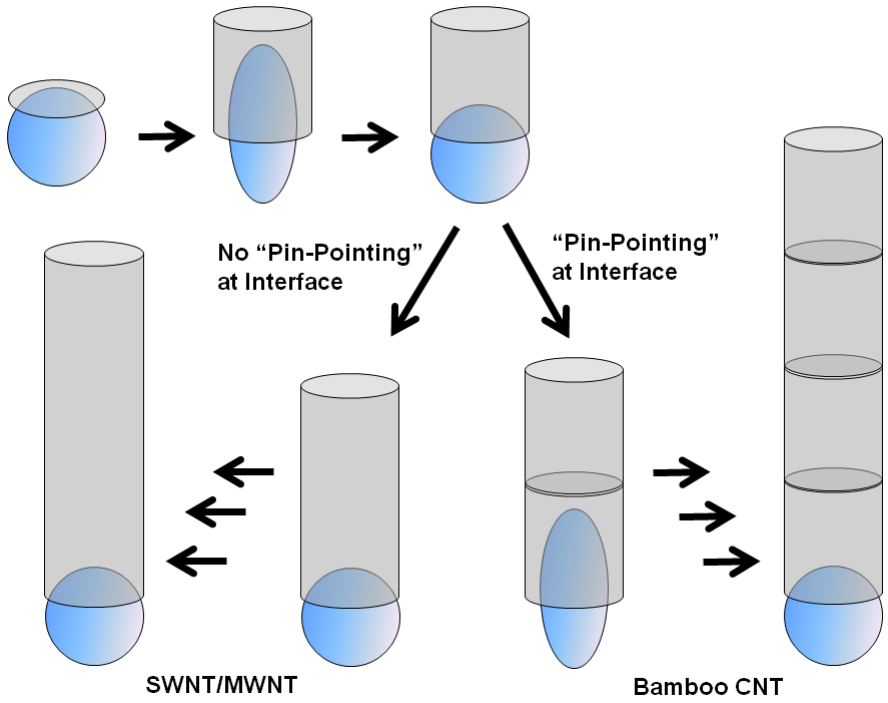


Figure 4.4: Schematic of CNT growth process. In stage one of CNT growth graphitic carbon nucleates on the catalyst surface. Stage two follows with deformation of the nanoparticle catalyst. Stage two growth repeats continually when "pin-pointing" occurs at the catalyst, resulting in BCNT growth. In the absence of "pin-pointing" growth enters stage three and SWNT/MWNT growth results.

graphitic structures to the nanoparticle catalyst than undoped structures. As discussed in the previous section, the nitrogen-cobalt bond is stronger than the carbon-cobalt bond. Nitrogen-cobalt bonds consequently cause local pinning of the nanoparticle catalyst to the interior of the nanotube, which increases residency time and ultimately leads to compartment and bamboo CNT formation.

Due to the CNT growth mechanism, the tip of the bamboo CNT is formed before the sidewalls, resulting in longer residency times at the tip and hence the disparity in the number of carbon layers through the typical bamboo CNT chamber. The chamber sidewalls are thicker near the tip of the chamber than the base because the deformation of the catalyst during growth means that the sidewalls near the tip receive more carbon. Each subsequent chamber tip has the same thickness as the tip of the first bamboo CNT chamber, which strongly suggests that stage two CNT growth involving catalyst elongation/relaxation

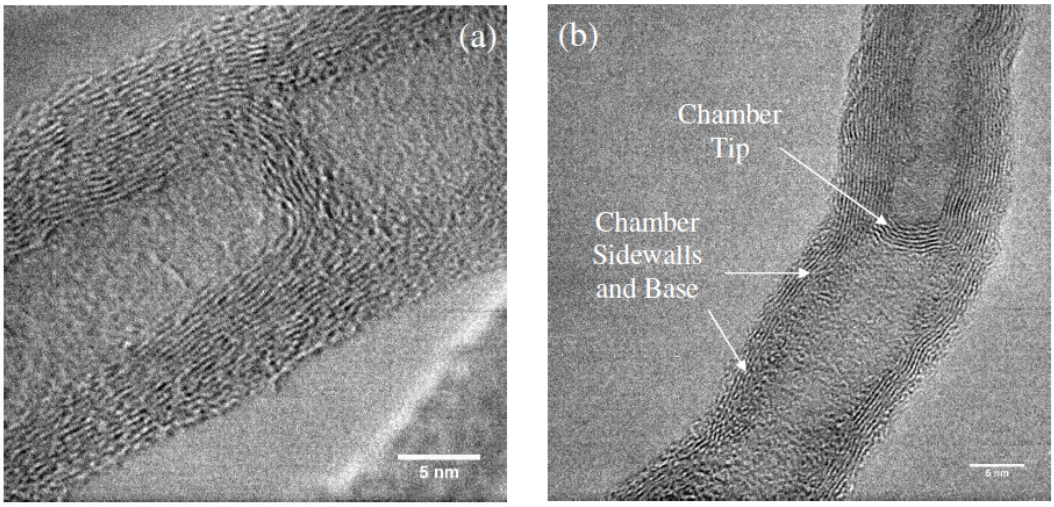


Figure 4.5: TEM images of N-doped bamboo-structured carbon nanotubes. Figure take from ref. [29].

repeats at regular intervals when a bamboo CNT forms. The third stage of CNT growth which produces the more typical SWNTs and MWNTs does not occur when nitrogen is incorporated in the CNT due to pinning at the catalyst surface.

The bamboo structure typical of nitrogen doped CNTs is also seen when alloy catalysts are employed in CNT growth [19, 20]. Use of alloy catalysts also alters the binding energy at the metal-CNT interface compared to use of a homogeneous catalyst. The commonality shared between nitrogen doped CNT growth and growth of CNTs from alloy catalysts is non-uniform nanoparticle-nanotube bond strengths. For nitrogen doped CNT growth the increase in ΔE is attributable to nitrogen; the nitrogen-metal bond is stronger than the carbon-metal bond. Similarly, when alloy catalysts are used, the binding strength is not uniform at the catalyst-CNT interface due to carbon bonding to different elements, *e.g.* stronger binding to Mo in Cu/Mo catalysts. The formation of bamboo CNTs has been observed when nitrogen is incorporated into the nanotube with growth conditions that produce SWNTs in the absence of nitrogen. The binding energies discussed show that nitrogen acts as a local pin-pointing agent between the nanoparticle and the CNT during growth and it is this effect which is directly responsible for

the bamboo CNT stucture of nitrogen doped CNTs.

4.6 Conclusion

In this chapter, theory and experiment are combined to offer an explanation of the bamboo CNT growth mechanism. DFT calculations show that the nitrogen-cobalt bond is stronger than the carbon-cobalt bond. This difference in bond strength results in points of increased interaction strength between the growing CNT and the nanoparticle, which results in elongation of the nanoparticle during growth. Repeated cycles of elongation and contraction of the nanoparticle are a direct result of the "pin-pointing" by nitrogen at the catalyst surface and are proposed as the cause of the experimentally observed bamboo structure of nitrogen doped CNTs [29].

4.7 References

[1] T.W. Odom, J.L. Huang, P. Kim, and C.M. Lieber. Atomic Structure and Electronic Properties of Carbon Nanotubes. *Nature*, 391:62–64, 1998.

[2] T.W. Odom, J.L. Huang, P. Kim, and C.M. Lieber. Structure and Electronic Properties of Carbon Nanotubes. *Journal of Physical Chemistry B*, 104:2794–2809, 2000.

[3] S.H. Lim, H.I. Elim, X.Y. Gao, T.S. Wee, W. Ji, J.Y. Lee, and J. Lin. Electronic and Optical Properties of Nitrogen-Doped Multiwalled Carbon Nanotubes. *Physical Review B*, 73:045402, 2006.

[4] I.O. Maciel, J. Campos-Delgado, E. Cruz-Silva, M.A. Pimenta, B.G. Sumpter, V. Meunier, F. Lopez-Urias, E. Munoz-Sandoval, H. Terrones, M. Terrones, and A. Jorio. Synthesis, Electronic Structure, and Raman Scattering of Phosphorus-Doped Single-Wall Carbon Nanotubes. *Nano Letters*, 9:2267–2272, 2009.

[5] Y.H. Huang, J.P. Gao, and R.Z. Liu. Structure and Electronic Properties of Nitrogen-Containing Carbon Nanotubes. *Synthetic Materials*, 113:251–255, 2000.

[6] M. Terrones. Science and Technology in the 21st Centuary: Synthesis, Properties and Applications of Carbon Nanotubes. *Annual Review of Materials Research*, 33:419–501, 2003.

[7] M. Glerup, M. Castignolles, M. Holzinger, G. Hug, A. Loiseau, and P. Bernier. Synthesis of Highly Nitrogen-Doped Multi-Walled Carbon Nanotubes. *Chemical Communications*, (20):2542–2543, 2003.

[8] P. Ayala, P. Arenal, M. Rümmeli, A. Rubio, and T. Pichler. The Doping of Carbon Nanotubes with Nitrogen and their Potential Applications. *Carbon*, 48:575–586, 2010.

[9] R. Czerw, M. Terrones, J.C. Charlier, X. Blase, B. Foley, R. Kamalakaran, B. Grobert, H. Terrones, D. Tekleab, P.M. Ajayan, W. Blau, M. Rühle, and D.L. Carroll. Identification of Electron Donor States in N-Doped Carbon Nanotubes. *Nano Letters*, 1:457–460, 2001.

[10] M. Terrones, P.M. Ajayan, F. Banhart, X. Blase, D.L. Carroll, J.C. Charlier, R. Czerw, B. Foley, N. Grobert, R. Kamalakaran, P. Kohler-Redlich, M. Rühle, T. Seeger, and H. Terrones. N-doping and Coalescence of Carbon Nanotubes: Synthesis and Electronic Properties. *Applied Physics A - Materials Science and Processing*, 74:355–361, 2002.

[11] C. Tang, Y. Bando, D. Golberg, and F. Xu. Structure and Nitrogen Incorporation of Carbon Nanotubes synthesized by Catalytic Pyrolysis of Dimethylformamide. *Carbon*, 42:2625–2633, 2004.

[12] M.S. He, S. Zhou, J. Zhang, Z. Liu, and C. Robinson. CVD Growth of N-Doped Carbon Nanotubes on Silicon Substrates and its Mechanism. *Journal of Physical Chemistry B*, 109:9275–9279, 2005.

[13] M. Nath, B.C. Satishkumar, A. Govindaraj, C.P. Vinod, and C.P. Rao. Production of bundles of aligned carbon and carbon-nitrogen nanotubes by the pyrolysis of precursors on silica-supported iron and cobalt catalysts. *Chemical Physics Letters*, 322:333–340, 2000.

[14] Y.L. Li, F. Hou, Z.T. Yang, J.M. Feng, X.H. Zhong, and J.Y. Li. The Growth of N-doped Carbon Nanotube Arrays on Sintered Al_2O_3 Substrates. *Materials Science and Engineering B - Advance Functional Solid-State Materials*, 158:69–74, 2009.

[15] Y. Cao, Y. Zhao, Q. Li, and Q. Jiao. Catalytic Synthesis of Nitrogen-Doped Multi-Walled Carbon Nanotubes Using Layered Double Hydroxides as Catalyst Precursors. *Journal of Chemical Sciences*, 121:225–229, 2009.

[16] E.F. Kukovitsky, S.G. L'vov, N.A. Sainov, V.A. Shustov, and L.A. Chernozatonskii. Correlation between Metal Nanoparticle Size and Carbon Nanotube Growth. *Chemical Physics Letters*, 355:497–503, 2002.

[17] F. Ding, P. Larsson, J.A. Larsson, R. Ahuja, H. Duan, A. Rosén, and K. Bolton. The Importance of Strong Carbon-Metal Adhesion for Catalytic Nucleation of Single-Walled Carbon Nanotubes. *Nano Letters*, 8:463–468, 2008.

[18] P. Larsson, J.A. Larsson, R. Ahuja, F. Ding, B.I. Yakobson, H. Duan, A. Rosén, and K. Bolton. Calculating Carbon Nanotube-Catalyst Adhesion Strengths. *Physical Review B*, 75:115409, 2007.

[19] Z. Li, J.A. Larsson, P. Larsson, R. Ahuja, J.M. Tobin, J. O'Byrne, M.A. Morris, G. Attard, and J.D. Holmes. Copper/Molybdenum Nanocomposite Particles as Catalysts for the Growth of Bamboo-Structured Carbon Nanotubes. *Journal of Physical Chemistry C*, 112:12201–12206, 2008.

[20] J.P. O'Byrne, Z. Li, J.M. Tobin, J.A. Larsson, P. Larsson, R. Ahuja, and J.D. Holmes. Growth of Carbon Nanotubes from Heterometallic Palladium and Copper Catalysts. *Journal of Physical Chemistry C*, 114:8115–8119, 2010.

[21] S. Helveg, C. López-Cartes, J. Sehested, P.L. Hansen, B.S. Clausen, J.R. Rostrup-Nielsen, A. Abild-Pedersen, and J.K. Nørskov. Atomic-scale imaging of Carbon Nanofibre Growth. *Nature*, 427:426–429, 2004.

[22] G. Kresse and Furthmüller. J. Efficient Iterative Schemes for *Ab Initio* Total-Energy Calculations using a Plane-Wave Basis Set. *Physical Review B*, 54:11169–11186, 1996.

[23] G. Kresse and J. Hafner. *Ab Initio* Molecular Dynamics for Liquid-Metals. *Physical Review B*, 47:558–561, 1993.

[24] G. Kresse and J. Hafner. *Ab Initio* Molecular-Dynamics Simulation of the Liquid-Metal Amorphous-Semiconductor Transition in Germanium. *Physical Review B*, 49:14251–14269, 1994.

[25] G. Kresse and D. Joubert. From Ultrasoft Pseudopotentials to the Projector Augmented-Wave Method. *Physical Review B*, 59:1758–1775, 1999.

[26] P.E. Blöchl. Projector Augmented-Wave Method. *Physical Review B*, 50:17953–17979, 1994.

[27] J.P. Perdew, J.A. Chevary, S.H. Vosko, K.A. Jackson, M.R. Pederson, D.J. Singh, and C. Fiolhais. Atoms, Molecules, Solids, and Surfaces - Applications of the Generalized Gradient Approximation for Exchange and Correlation. *Physical Review B*, 46:6671–6687, 1992.

[28] M. Methfessel and A.T. Paxton. High-Precision Sampling for Brillouin-Zone Integration in Metals. *Physical Review B*, 40:3616–3621, 1989.

[29] J.P. O'Byrne, Z. Li, S.L.T. Jones, P.G. Fleming, J.A. Larsson, M.A. Morris, and J.D. Holmes. Nitrogen-Doped Carbon Nanotubes: Growth, Mechanism and Structure. *ChemPhysChem*, 12:2996–3001, 2011.

[30] J.Y. Raty, F. Gygi, and G. Galli. Growth of Carbon Nanotubes on Metal Nanoparticles: A Microscopic Mechanism from *Ab Initio* Molecular Dynamics Simulations. *Physical Review Letters*, 95:096103, 2005.

[31] M. Lin, J.P.Y. Tan, C. Boothroyd, K.P. Loh, Tok. E.S., and Y.L. Foo. Dynamical Observation of Bamboo-like Carbon Nanotube Growth. *Nano Letters*, 7:2234–2238, 2007.

Chapter 5

Aluminium-Carbon Nanotube Interface Electronic Properties: The Effect of Dopants

5.1 Introduction

In order for CNT potential applications to be realised, CNTs must be contacted to metals and so it is imperative that the metal-CNT contact is understood at a fundamental level. There are two major configurations into which CNT-metal contacts may be categorised: side contact and end contact. In the side contact configuration, the CNT side wall makes contact with the metal [8], while the CNT is terminated by the metal in the end contact configuration [12]. In this work, focus is placed on the end contact configuration.

The metal used in the contact profoundly affects the nature of the contact formed, with Ohmic or Schottky contacts formed depending on the metal used [13]. The contrasting behaviours resulting from contact with different metals is presumed to be caused by differences in the metal work function ϕ_m; Ohmic contacts result when high ϕ_m metals are used conversely, a low ϕ_m is associated with Schottky contacts [14]. The major advantage of the end contact configuration is that it enables stronger bonding between the CNT and metal, which has

been implicated as the source of the better transport behaviour in Pd than Au, despite their identical ϕ_m [15]. While consideration of ϕ_m has some success as a simple prediction of contact behaviour, it clearly cannot account for the more subtle aspects of the contact such as the interface structure. Early tight binding molecular dynamics studies indicate the importance of understanding the detailed CNT-interface geometry by showing the position on the CNT where Ni-C bonds formed dramatically impacted the CNT properties [16, 17].

The Al-CNT contact has been previously studied theoretically by Bai [18], Okada [19], Odbadrakh [20], Vitale [21] and Gao [22]. The Okada study considers a side contact configuration, while Bai considers side and end-type contacts. The works of Odbadrakh, Vitale and Gao study the end contact configuration exclusively, using structures most similar to those considered in this work. In particular, these studies highlight the importance of considering the metal induced gap states (MIGS) or regions of finite DOS in the gap of the isolated semiconductor which are induced upon contact to a metal. If the device region used in calculations is too short, semi-conducting CNTs appear metallic due to slowly decaying MIGS.

At this time it is not possible to selectively grow CNTs of a particular chirality and hence with specific electronic properties; despite extensive research efforts only preferential growth of certain chiralities has been achieved [23–25]. Doping CNTs offers an alternative path towards control of electronic properties. Substitional doping by boron or nitrogen results in metallic CNTs [26–29], but also introduces additional problems. The electronic properties of intrinsically metallic CNTs degrade on incorportation of substitutional dopants [30, 31] and in addition it is difficult to precisely control the level of dopants within the CNT and dopant atom fluctuations [32] will necessarily impact on achieving reproducible electronic properties. As CNTs are hollow, it is also possible to incorporate dopants within the CNT *i.e.* endohedral doping. Endohedral dopants such as fullerenes [33],

metallocenes [34] and organic molecules [33, 35–39] have been studied in the literature, with significant effects found for the electronic properties of the doped CNTs. Endohedral dopant molecules with large electron affinities induce p-type doping while those with small ionisation potentials result in n-type doping of the CNT.

This work focuses on end contacts between aluminium and doped (16,0)-CNTs, previous studies of the end contact configuration consider smaller diameter, less realisitic CNTs. Idealised nitrogen and boron doped CNTs (*i.e.* we assume no additional defects) are considered along with the endohedral dopant tetrathiafulvalene (TTF) which is known to induce n-type doping in CNTs and to be air stable as an endohedral dopant [38]. To the best of our knowledge, doped CNTs have not before been studied theorectically in conjunction with metal contacts. In each case, we study the system under zero and finite source-drain bias using first principles non-equilibrium Green's function (NEGF) calculations.

5.2 Methods

Density functional theory (DFT) and NEGF [40] as implemented by the software package OpenMX [41] are used to calculate the transport characteristics of the Al-CNT interface. All calculations use the PBE [42] formulation of the generalised gradient approximation (GGA) exchange and correlation functional, along with normconserving pseudopotentials [43]. The Al-CNT interface is modelled by bonding a (16,0)-CNT (pristine; substitutionally doped with N and B; and endohedrally doped with TTF) to a (111) Al slab. In each case full structural optimisations are carried out for the interfaces (with the exception of the Al back plane, which is frozen) and for the Al and CNT lead units until all forces are less than $5\text{x}10^{-4}$ Hartree/Bohr. The OpenMX code employs a linear combination of pseudo atom orbitals method [44, 45], the pseudoatomic orbitals chosen for

geometry optimisations are as stated in Table 5.1. An energy cut-off of 150 Ry is used for numeric integration and supercells were chosen such that there was a minimum vacuum of 1 nm in all non-periodic directions.

Table 5.1: Basis sets used for geometry optimisations and NEGF calculations. The first part of the basis set notation, *i.e.* the number, is the cut-off radius of the PAO in Bohr, the second part indicates the number of orbitals used for the valence electrons. For example, S 6.0-s2p2 implies a cut-off of 6.0 Bohr and a total of 8 basis functions (2 s functions and 6 p functions)

Element	Geometry	NEGF
H	4.0-s2	4.0 s2
B	4.5-s2p2	4.5-s1p1
C	4.5-s2p2	4.5-s2p1
N	4.5-s2p2	4.5-s1p1
Al	6.0-s2p3	6.0-s1p2
S	6.0-s2p2	6.0-s2p2

The NEGF method is used to generate the transport characteristics. The basis sets used in the NEGF calculations are as given in Table 5.1. A 128x128x128 grid is used for numeric integration and the cell size is again chosen to have 1 nm of vacuum, in this case in all directions perpendicular to the transport direction. The calculations are considered converged when the norm of the residual density matrix was below at least $1\text{x}10^{-4}$ and ideally below $1\text{x}10^{-6}$, although this stricter convergence criterium has negligible impact on the electronic properties. Transmission curves are obtained as follows: first, band structure calculations are performed for the left (Al) and right (CNT) leads using the same basis sets to be employed in the NEGF calculations to generate the lead Hamiltonians; next NEGF calculations are performed for structures consisting of these leads and a central scattering region which together form the interface; finally NEGF results are used to generate the transmission with the TranMain code. As well as calculating transmission at zero bias, we calculate the transmission at finite source-drain biases, with the bias applied to the right (CNT) electrode. In the case of the pristine CNT, a full NEGF calculation is performed in steps of 0.1

V between -1.0 V and 1.0 V. We then use the OpenMX interpolation scheme between 0 bias and 1 V and -1 V to generate the other data points which allows us to assess the applicability of the interpolation scheme in general for the study of the Al-CNT systems. For all other Al-CNT interfaces, full NEGF calculations are performed for 0 bias, 1 V and -1 V with interpolation used to generate additional data points. In each case we check the interpolation by performing full NEGF calculations for two additional data points.

5.3 Electronic Structure of the CNT leads

The structures of the CNT lead unit principle layers are shown in Figure 5.1. The pristine CNT lead consists of single repeat unit of the (16,0)-CNT unit cell containing 64 carbon atoms. The B- and N-doped leads consist of three repeat units of the pristine CNT lead cell with two substitutional dopants with the same doping profile used in both dopant cases. The substitutional dopant concentration is 1 at. %, a relatively low level for N- and B-dopants in CNTs, which range up to 20 at. % experimentally. The TTF@CNT structure contains a TTF molecule per unit cell of the (16,0)-CNT; this dopant concentration has been previously reported by Lu *et al* [37] to be necessary for doping of the CNT by the encapsulated TTF to occur. The TTF@CNT lead used for transport calculations consists of three such unit cells. Mulliken populations analysis shows that TTF donates electronic charge to the CNT, which is anticipated for an endohedral dopant with a small ionisation potential. Encapsulated TTF is found to have a net positive charge of $0.09|e|$ hence TTF donates 0.09 electrons to the CNT in reasonable agreement with the value of $0.12|e|$ estimated by Lu [37], well within the error inherent in Mulliken population analysis.

The band structures of the CNT-leads are given in Figure 5.2. The pristine (16,0)-CNT has a band gap of $\sim$0.5 eV, which is consistent with literature DFT

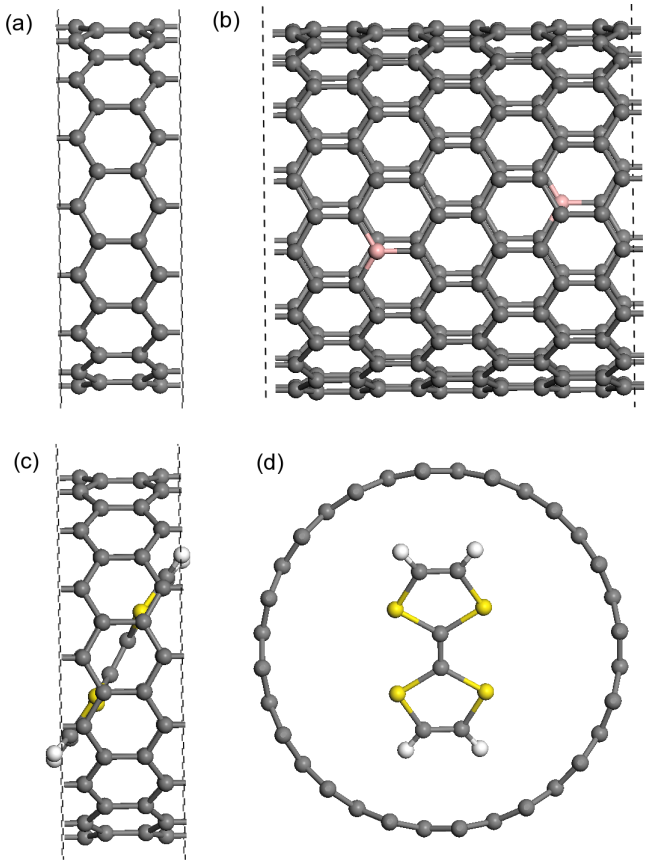


Figure 5.1: Optimised (16,0)-CNT Lead structures (carbon is grey, hydrogen is white, boron is pink and sulfur is yellow). (a) Side view of pristine (16,0)-CNT lead. (b) Side view of B-CNT lead (an identical dopant profile is used in the N-doped lead). Side (c) and top (d) view of TTF@CNT lead.

values for this chirality [46]. Already, at the relatively low substitutional doping concentration for CNTs used in this study, the B-doped and N-doped band structures clearly show that the CNT is metallic, with bands crossing the Fermi level. The gap of the pristine CNT persists but is narrowed by 0.1 eV and shifted to higher (lower) energies by $\sim$0.5 eV for B-(N-)dopants. These results are consistent with previous literature reports [30, 47, 48]. The band structure of TTF@CNT is consistent with n-type doping of the CNT, the flat dopant band meets the conduction band of the CNT close to the Fermi level. This flat dopant band contrasts greatly with the curved bands seen for N and B dopants and implies that the TTF states remain very localised and there is little interaction between the dopant molecules. This difference is unsurprising, given N and B and incorpo-

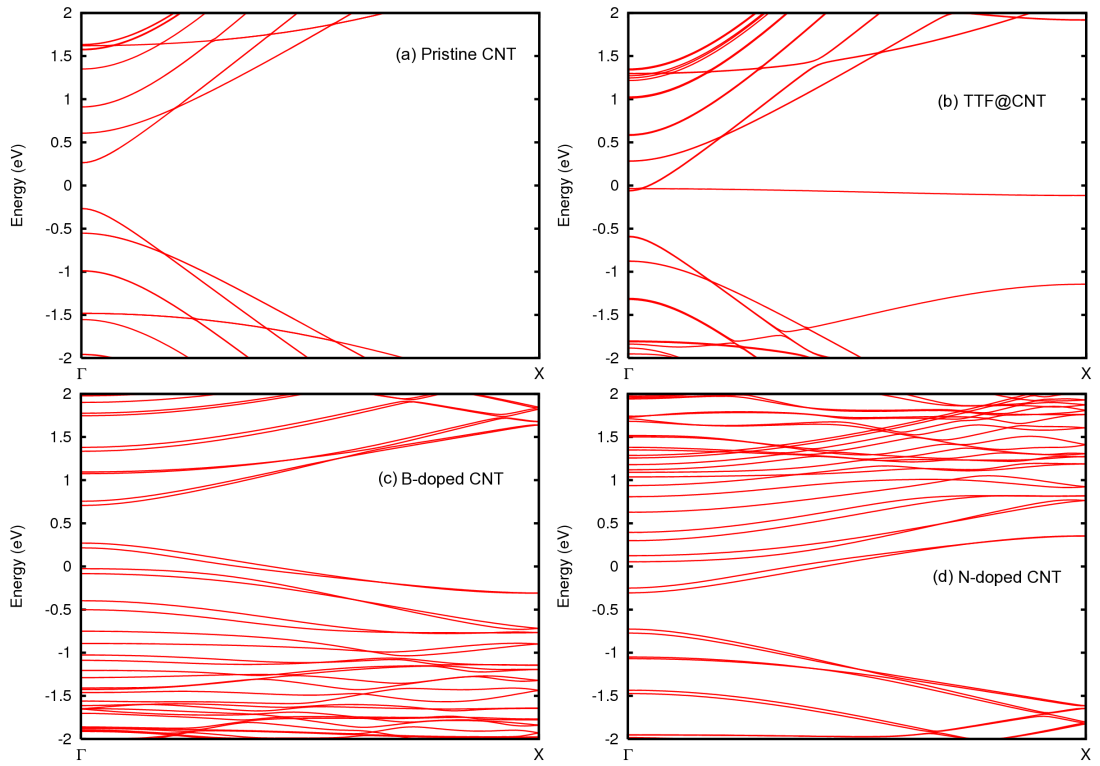


Figure 5.2: Band structures for the pristine and doped (16,0)-CNT lead structures. The Fermi level is at 0 eV in all cases.

rated into the CNT sidewall, while the endohedral dopants are merely physisorbed inside the CNT. The study by Lu *et al* finds a relatively curved dopant band for TTF@CNT when there is one CNT unit cell for each TTF molecules and conversely finds an almost flat band when there are two CNT unit cells for each TTF molecule. The origin of this discrepancy in band structure is not known.

While the introduction of N and B in the CNT lattice clearly results in heavy doping of the CNTs as is seen in the band structures in Figure 5.2, these dopant atoms also act as defects in the CNT lattice. Before contacting these CNTs to Al, we assess the scattering which results from these defect atoms by considering the transmission of the periodic CNT structures, which are shown in Figure 5.3. At positive energies, a considerable deviation from the characteristic CNT stepped transmission is seen for the N-doped CNT and similarly at negative energies a deviation is seen for the B-doped CNT, therefore significant electron

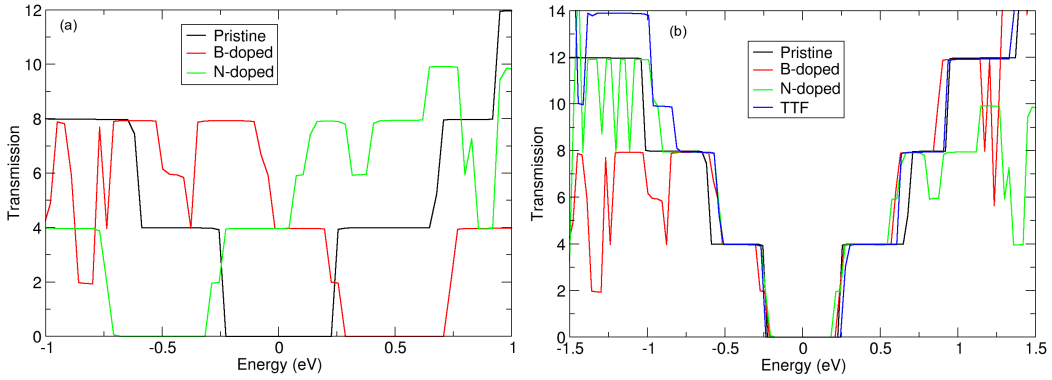


Figure 5.3: Transmission of the doped CNTs. (a) The Fermi level is energy is 0 eV for all CNTs, the TTF@CNT curve is only shifted by ∼0.35 eV relative to the pristine CNT and has been omitted for clarity. (b) The transmissions of the doped CNTs have been shifted to coincide with the transmission gap of the pristine CNT, to emphasize the scattering relative to the pristine CNT.

scattering occurs when there are N and B dopants in the CNT lattice, particularly in the conduction band for N-doping and in the valence band for B-doping. We have a low dopant concentration relative to many experimentally generated N- and B-doped CNTs and so an even greater scattering would be anticipated for such CNTs. In the case of TTF@CNT the transmission is only shifted relative to the pristine CNT (as would be expected from the band structures) without significant scattering. The preservation of the ideal CNT lattice and resultant lack of scattering is one of the primary advantages endohedral doping has over substitutional doping.

5.4 Al-CNT Interfaces

The structure used in the NEGF calculations is shown in Figure 5.4 for the interface between Al and the pristine CNT. A similar structure is used for the calculations involving the doped leads. In the case of the pristine CNT there are a total of 7 CNT repeat units in the extended scattering region; see Figure 3.2. We find significant metal induced gap states (MIGS) - states in the band gap of a semiconductor resulting from contact to a metal - in the CNT repeat

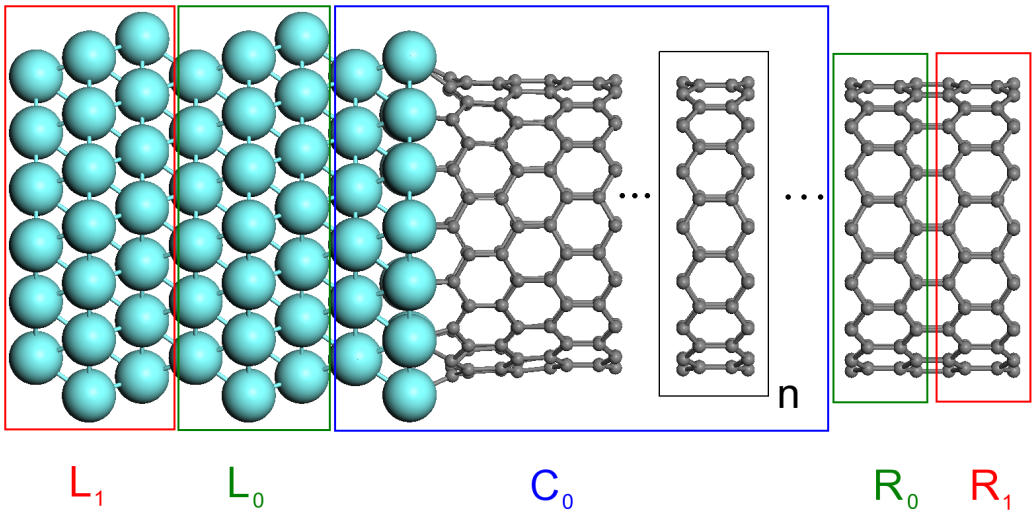


Figure 5.4: Structure of the pristine Al-CNT interface (n=4), labelled as described in Figure 3.2. An adapted version of this structure is used for the interfaces between Al and the doped CNTs.

unit which bonds to the Al, labelled as "Repeat 1" in the inset of Figure 5.5 (a). The MIGS are found to drop off in an exponential fashion in Figure 5.5 (a), with low MIGS for repeat unit 7 ("Repeat 7"). This result is consistent with that previously reported by Odbadrakh for the interface between (8,0)-CNT and Al metal [20] and highlights the importance of considering sufficiently large structures in NEGF calculations of metal-CNT interfaces. The study of Al-CNT and Pd-CNT interfaces by Gao *et al* [22] used only two CNT units between the metal leads, consequently, although the semi-conducting (10,0)-CNT was studied, they found no gap in transmission and an Ohmic contact. A similar effect is seen in the case of the doped CNT-Al interfaces, except that the CNT gap is displaced from the Fermi energy, as already seen for the doped CNT lead band structures.

Figure 5.5 (b) plots the average charge found on the atoms in the layers of the structure in Figure 5.4 by Mulliken population analysis, clearly charge is transferred from the Al nanowire to the CNT, *i.e.* a surface dipole forms, with a total of 2.9 electrons donated to the CNT. The charge in the CNT layers far from the interface oscillate and there is no net charge transfer to the CNT outside of the carbon layer involved in bonding at the interface, this result is consistent

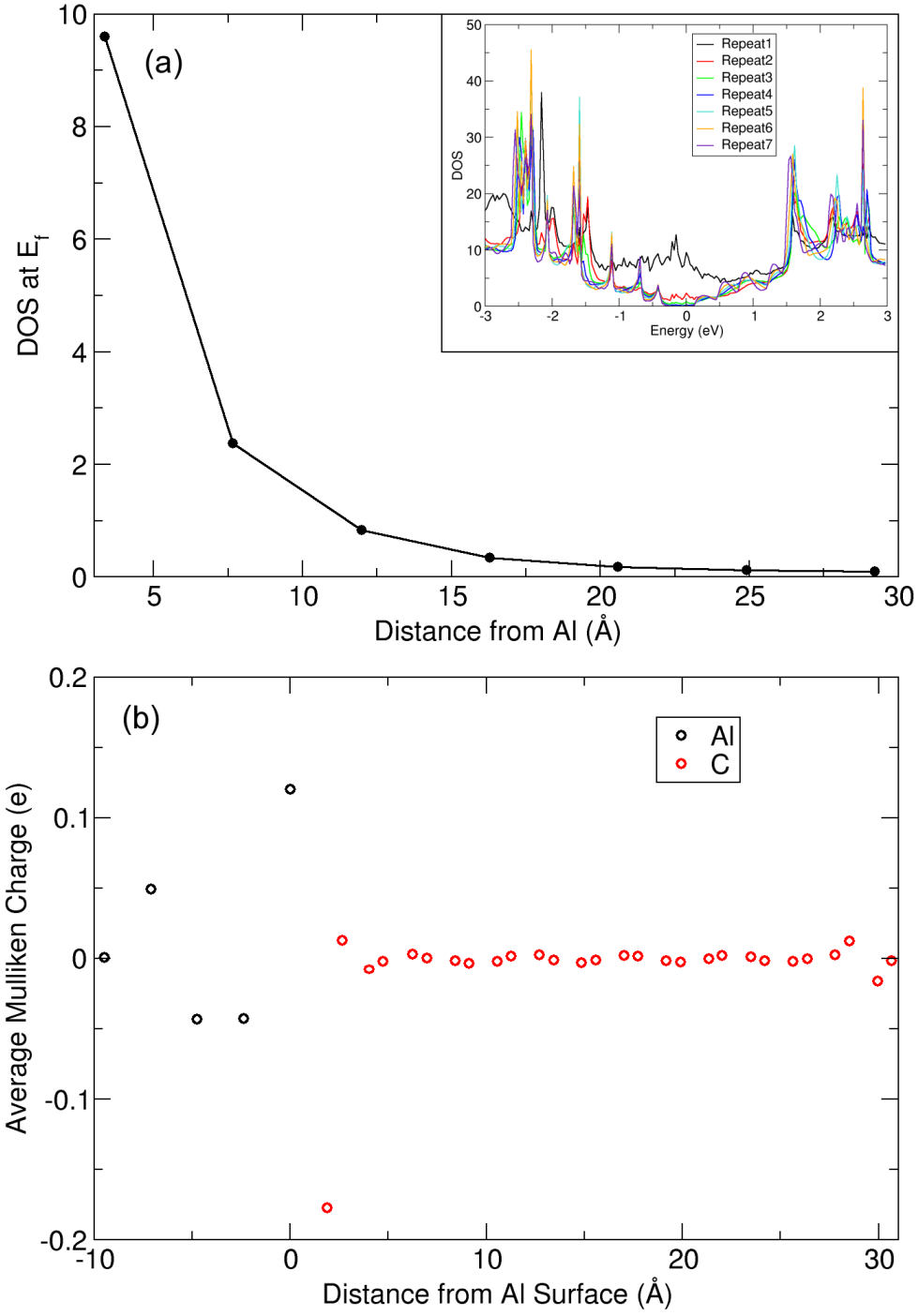


Figure 5.5: (a): Decay in CNT gap states with distance from the interface for the pristine CNT. (inset): DOS of each CNT repeat unit in the scattering region of the pristine CNT, notice the reappearance of the CNT gap. (b): Average Mulliken charge per layer for the Al-CNT interface. Electronic charge is transfered from Al to C at the interface.

with that previously reported for the interface between Al and a (10,0)-CNT [21]. A similar direction of charge transfer is found for the interfaces between Al and the doped CNT structures, with a transfer of 2.5e, 1.6e and 1.5e found for the B-doped CNT, N-doped CNT and TTF@CNT respectively.

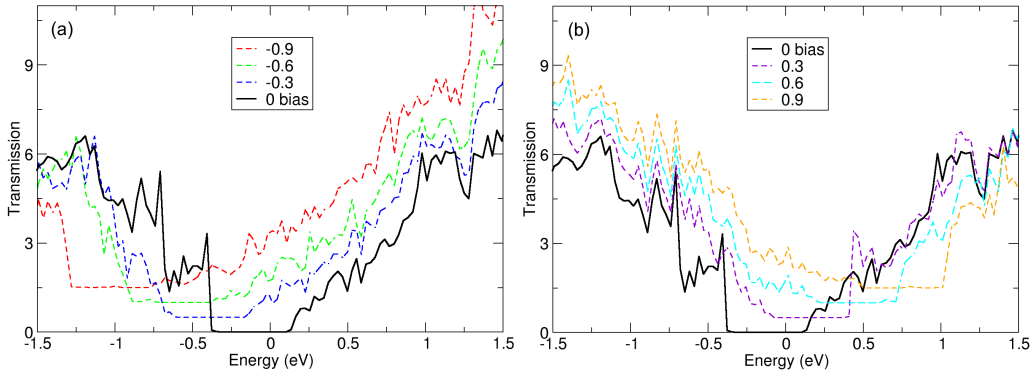


Figure 5.6: Transmission of Al-Pristine CNT interface for bias voltages for selective negative (a) and positive (b) source-drain bias voltages. The curves have been displaced along the y-axis for clarity.

In Figure 5.6, the transmission for the interface between the pristine CNT and Al at zero bias and selected negative and postive source drain biases is given, with the bias applied to the right (CNT) electrode. The zero-bias transmission matches up with the DOS plotted in the inset of Figure 5.5 (a) as is to be expected, since if there is zero DOS, transmission cannot occur. The transmission is lower than that of the periodic CNT (Figure 5.3) implying that significant electron scattering takes place at the Al-CNT interface. The primary affect of applying a source drain bias is to shift the obtained transmission, as shown in Figure 5.6. A negative applied bias pushes the Fermi energy above the transmission gap associated with the CNT, while a positive applied bias has the opposite effect, with the Fermi energy moving below the region of zero transmission. As described in Section 3.9, the current is obtained by integrating the transmission over a voltage bias window. At zero applied bias, there is no current. As a negative bias is applied, the transmission at the Fermi energy becomes non-zero for -0.3 V as seen in Figure 5.6 (a), therefore a current is to be expected at such a

bias. If instead a positive bias is applied, the transmission is still zero for 0.3 V as seen in Figure 5.6 (b), but is clearly non-zero for an applied bias of 0.6 V, thus we can anticipate that the current will become non-zero at biases larger than 0.3 V and an asymmetric current-volatge (IV) curve is hence expected for the contact between the pristine CNT and Al.

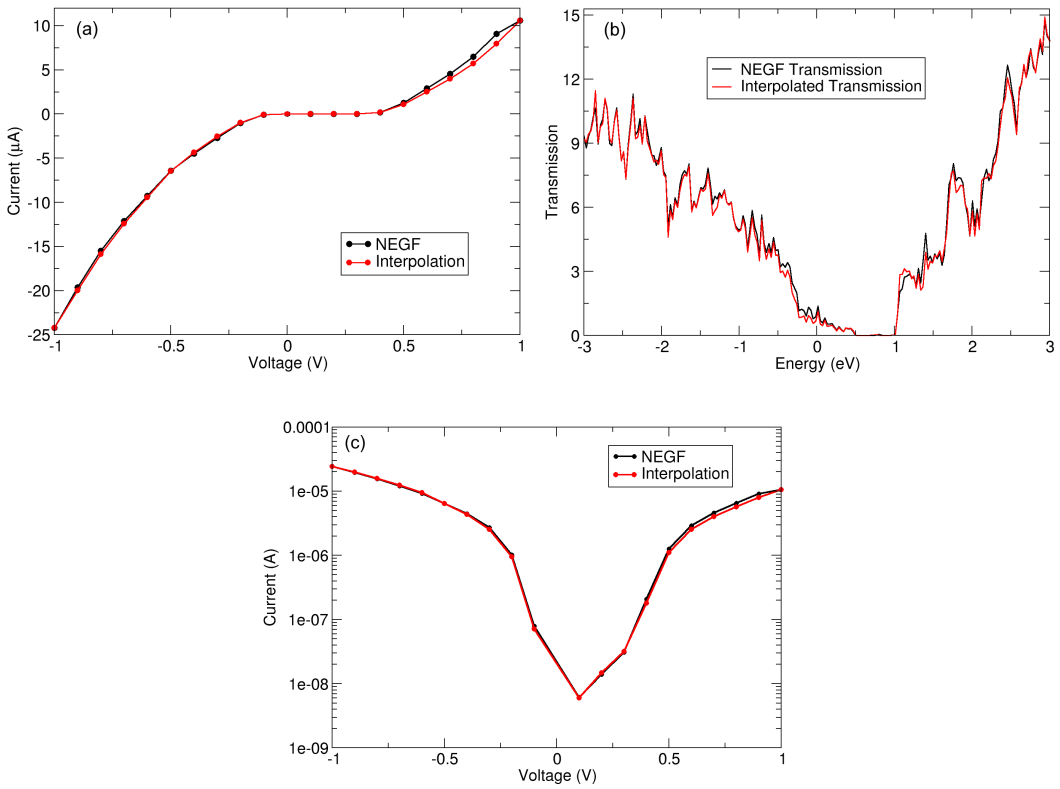


Figure 5.7: (a) Comparison of NEGF and OpenMX interpolation scheme for the IV characteristics at the interface of pristine CNT and Al. (b) Comparison of NEGF and interpolated transmission for an applied bias of 0.9 V. (c) Log scale plot of IV.

The IV curve we obtain for the pristine CNT-Al contact is given in Figure 5.7 (a). The IV curve is consistent with our analysis of the transmission results. There is marked asymmetry between current at positive and negative source drain biases and diode-like behaviour caused by the position of the Fermi energy being close to the CNT conduction band edge after contact is made with Al. We also include the IV curve obtained by interpolating between the zero bias result and 1.0 and -1.0 results, showing the excellent agreement between these two techniques

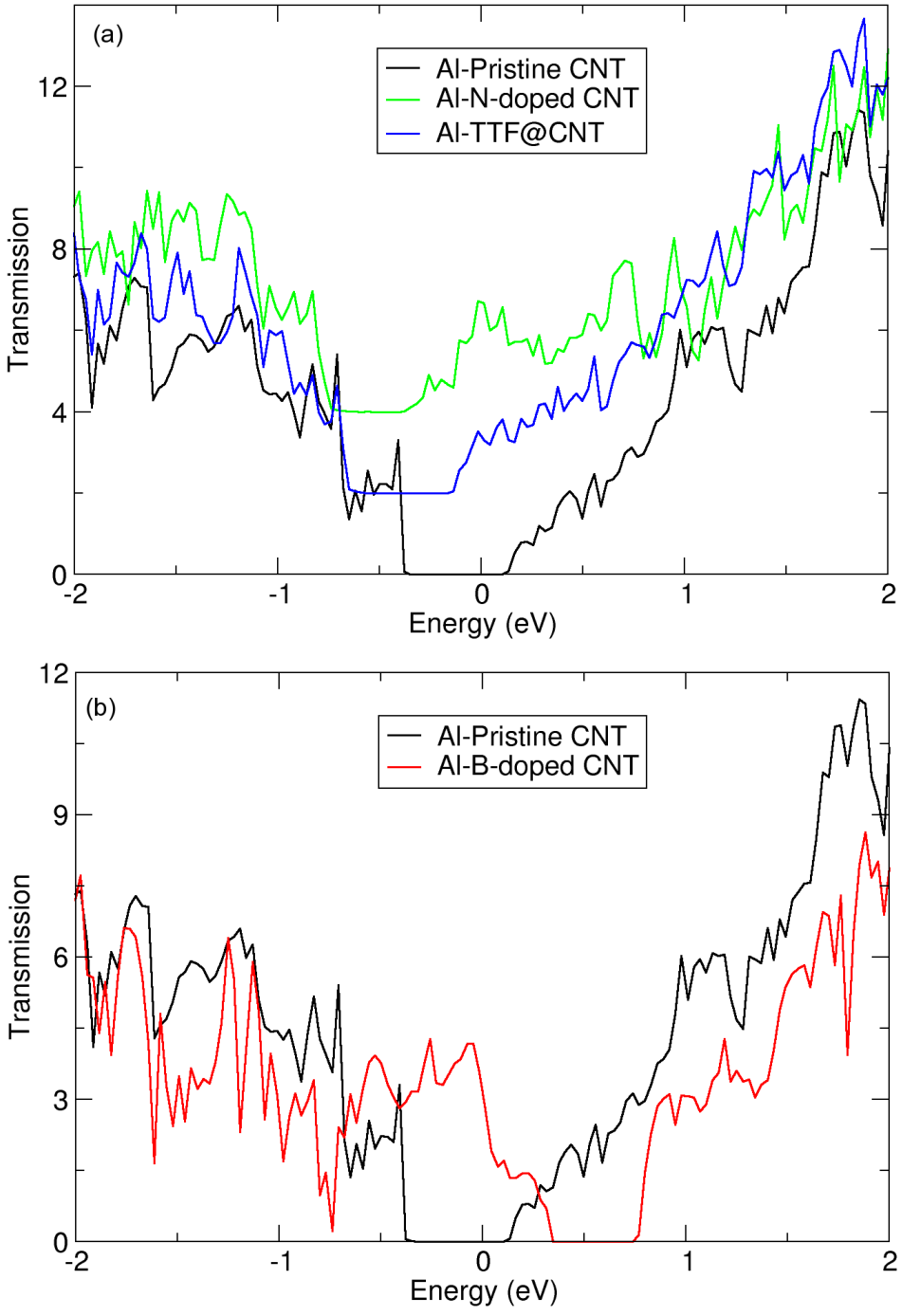


Figure 5.8: (a) Transmission of the pristine, N-doped and TTF@CNT contacts with Al. For clarty, the transmissions of the doped interfaces have been shifted along the y-axis. (b) Transmission of the pristine and B-doped CNT interfaces.

for calculating IV curves. Figure 5.7 (b) compares the transmission for 0.9 V bias (among the IV points showing poorest agreement between NEGF and interpolation) and again see very good agreement between the NEGF and interpolation scheme results. We consider the interpolated results to be sufficiently accurate to be employed for generating the IV curves of the interfaces between the doped CNTs and Al, with checks on the interpolated IV curve performed as described in the methods section. Odbadrakh and co-workers [20] have previously calculated the IV curve at postive bias for the Al/(8,0)-CNT contact and also found currents of the order of μA.

Figure 5.8 (a) and (b) plot the zero bias transmission for the pristine and doped CNT interfaces with Al. The shifting and narrowing of the CNT gap seen on doping with N and B is preserved when the CNT is contacted to metal. The transmission of the N- and B-doped contacts with Al is generally less than that of the pristine CNT; the scattering which results from substitutional dopants has an impact and is visible in the transmission curve even after scattering due to a metal-CNT interface occurs. For example, there is a sharp dip in transmission for the B-doped CNT interface at $\sim$-0.9 eV which corresponds to a similar dip seen for the B-doped CNT by itself (see Figure 5.3 (a)), a similar sharp drop in transmission which can be attributed to scattering at the dopant atom can be seen at $\sim$0.7 eV in the case of the N-doped CNT. The dopant "defect" will clearly have an impact on the IV characteristics of the interfaces studied. In the case of TTF, the transmission closely follows the transmission of the pristine CNT-Al interface, again illustrating that the endohedral dopant does not cause significant scattering because it does not disrupt the CNT lattice in the way the substitutional dopants do. As discussed for the CNT lead structures, the primary effect of doping with TTF is to shift the Fermi level by $\sim$ 0.3 eV with respect to the pristine CNT.

The current-voltage characteristics of the pristine and doped CNT-Al inter-

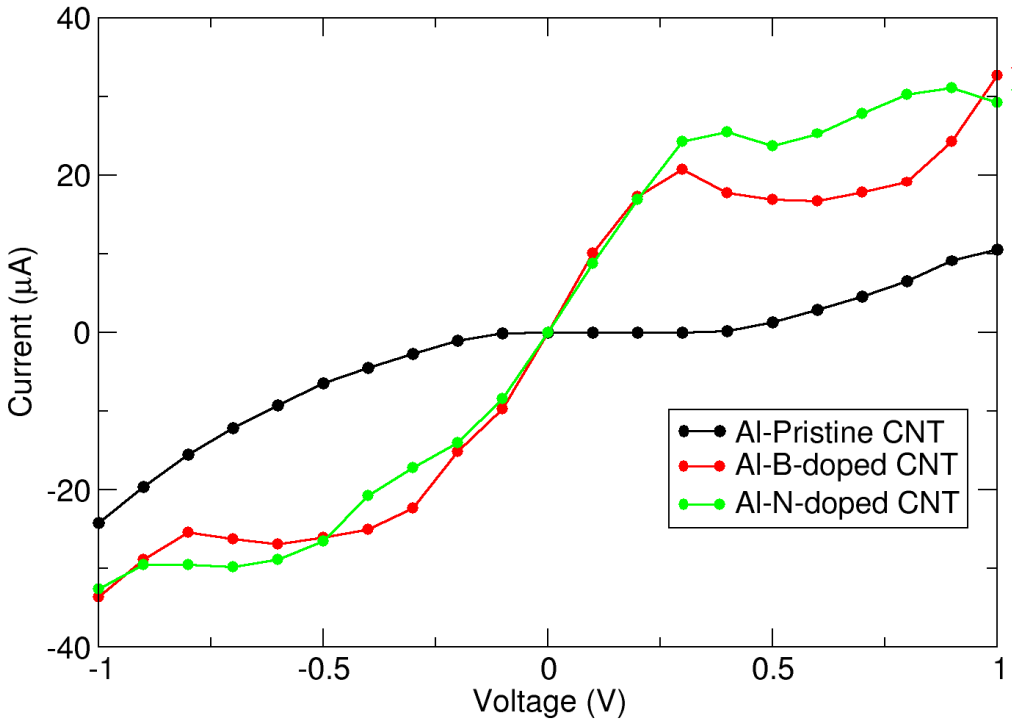


Figure 5.9: Current-Voltage graph of the pristine and doped Al-CNT interfaces.

faces are shown in Figure 5.9. As already discussed, there is no current through the pristine CNT-Al interface at low source-drain biases and there is an asymmetric IV behaviour due to the Fermi level aligning closer to the conduction band of the CNT. This contrasts greatly with the behaviour of the interfaces between the metallic B- and N-doped CNTs and Al. Similar IV curves are obtained for both substitutional dopants, with a linear IV at low bias, indicating an Ohmic contact is formed as anticipated by the non-zero DOS at the Fermi level for these cases. At larger negative biases, the transmission gap due to the CNT band gap is encountered for the B-doped interface which results in a flattening of the IV curve. A similar behaviour is seen for the N-doped interface, but this time at positive bias voltages. However, a flattening of the IV curve is also seen at biases which do not encounter the transmission gap in Figure 5.8 for both B- and N-doped CNTs. We attribute this flattening of the IV curve at positive(negative) biases for B(N) to scattering at the substitutional dopant atoms. At low bias voltages,

doped CNTs may offer a route to exclusively metallic CNTs and Ohmic metal-CNT contacts. In this work we find that the (16,0)-CNT becomes metallic when substitutionally doped, additional investigation is needed to ascertain the conducting behaviour of doped armchair and chiral CNTs and the nature of contacts between metal and such CNTs to confirm this behaviour holds in general.

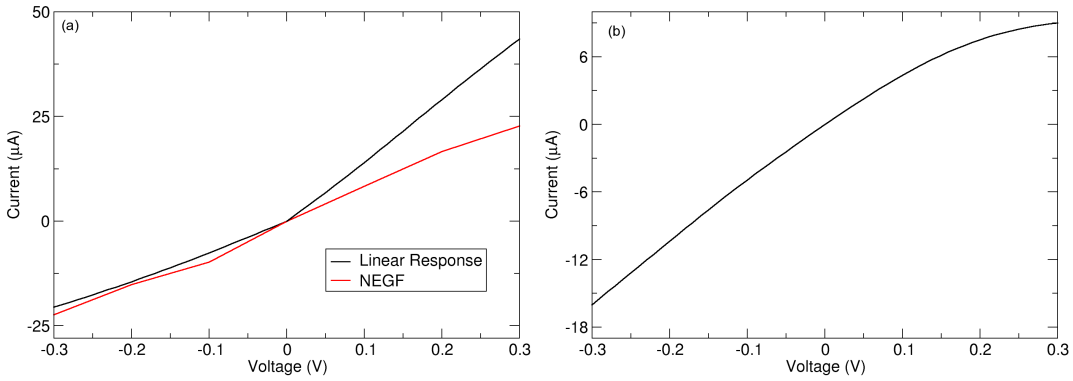


Figure 5.10: (a) Comparison of NEGF and linear response IV curves at low bias for the Al-B-doped CNT interface. (b) Linear response IV curve for Al-TTF@CNT interface.

Figure 5.10 (a) compares the IV curve obtained from NEGF calculations and a linear response method which uses the zero-bias transmission only for the Al-B-doped CNT interface and shows that at low bias voltages there is a reasonable agreement between these results particularly for negative bias voltages. In Figure 5.10 (b), the linear response IV curve for the Al-TTF@CNT interface obtained from the zero-bias transmission results of Figure 5.8 (a) is shown. At very low biases the IV curve is linear and at negative applied bias this linearity is maintained. However, at a small positive bias of 0.1 V, the IV curve begins to flatten as the CNT transmission gap is encountered in an analogous fashion to the interface with the N-doped CNT, though at a lower bias (see Figures 5.8 (a) and 5.9). As already discussed, endohedral TTF dopes the CNT with minimal scattering, therefore it can also be anticipated that even at higher applied negative biases, the IV will remain linear. Thus, the contact has a diode-like behaviour. At postive applied biases, the CNT gap is encountered at low bias ($<$ 200 mV) and

the current saturates at ~ 8 μA, while at negative biases a linear current-voltage relationship is maintained.

5.5 Conclusion

Substitutional doping by boron and nitrogen at concentrations of 1 at. % makes the (16,0)-CNT metallic. Boron and nitrogen act as defects in the CNT lattice resulting in a reduction in transmission relative to the undoped CNT whereas endohedral doping of the CNT does not cause significant scattering compared to the pristine CNT. The interface between the CNTs and Al is also a source of significant scattering. A slightly asymmetric IV curve occurs for the Al-contacted undoped CNT with little current at low source-drain biases. Similar IV characteristics occur for Al-contacted B- and N-doped CNTs, with a linear IV occurring at low bias, indicative of an Ohmic contact, however at larger biases the IV curve becomes non-linear because the shifted CNT gap is encountered and due to scattering off the B/N atoms in the CNT. A linear IV is also obtained for the Al contacted TTF@CNT for low biases, however due to the position of the Fermi level, the CNT gap is encoutered at small positive biases and a diode-like behaviour is anticipated.

5.6 References

[1] R.H. Baughman, A.A. Zakhidov, and de Heer W.A. Carbon Nanotubes - The Route Towards Applications. *Science*, 297:787–792, 2002.

[2] P. Avouris, Z.H. Chen, and V. Perebeinos. Carbon-Based Electronics. *Nature Nanotechnology*, 2:605–615, 2007.

[3] G.F. Close, S. Yasuda, B. Paul, S. Fujita, and H.S.P. Wong. A 1 GHz Integrated Circuit with Carbon Nanotube Interconnects and Silicon Transistors. *Nano Letters*, 8:706–709, 2008.

[4] S.J. Tans, A.R.M. Verschueren, and C. Dekker. Room-Temperature Transistor based on a Single Carbon Nanotube. *Nature*, 393:49–52, 1998.

[5] A. Javey, H. Kim, M. Brink, Q. Wang, A. Ural, J. Guo, P. McIntyre, P. McEuen, M. Lundstrom, and H. Dai. High-κ Dielectrics for Advanced Carbon-Nanotube Transistors and Logic Gates. *Nature Materials*, 1:241–246, 2002.

[6] R.T. Weitz, U. Zschieschang, F. Effenberger, H. Klauk, M. Burghard, and K. Kern. High-Performance Carbon Nanotube Field Effect Transistors with a Thin Gate Dielectric Based on a Self-Assembled Monolayer. *Nano Letters*, 7:22–27, 2007.

[7] J. Svensson, N. Lindahl, H. Yun, M. Seo, D. Midtvedt, Y. Tarakanov, N. Lindvall, O. Nerushev, J. Kinaret, S. Lee, and E.E.B. Campell. Carbon Nanotube Field Effect Transistors with Suspended Graphene Gates. *Nano Letters*, 11:3569–3575, 2011.

[8] H.M. Manohara, E.W. Wong, E. Schlecht, B.D. Hunt, and P.H. Siegel. Carbon Nanotube Schottky Diodes Using Ti-Schottky and Pt-Ohmic Contacts for High Frequency Applications. *Nano Letters*, 5:1469–1474, 2005.

[9] J Liu, C.G. Lu, L. An, Q.A. Fu, H. Zhang, and J. Murduck. Schottky Diodes from Asymmetric Metal-Nanotube Contacts. *Applied Physics Letters*, 88:133501, 2006.

[10] J. Kong, N.R. Franklin, C. Zhou, M.G. Chapline, S. Peng, K. Cho, and H. Dai. Nanotube Molecular Wires as Chemical Sensors. *Science*, 287:622–625, 2000.

[11] A. Modi, N. Koratkar, E. Lass, B. Wei, and P.M. Ajayan. Miniaturized Gas Ionization Sensors using Carbon Nanotubes. *Nature*, 424:171–174, 2003.

[12] C. Santini, A. Volodin, C. Van Haesendonck, S. De Gendt, G. Groeseneken, and P.M. Vereecken. Carbon Nanotube-Carbon Nanotube Contacts as an Alternative towards Low Resistance Horizontal Interconnects. *Carbon*, 49:4004–4012, 2011.

[13] W.G. Zhu and E. Kaxiras. The Nature of the Contact between Pd Leads and Semiconducting Carbon Nanotubes. *Nano Letters*, 6:1415–1419, 2006.

[14] F. Leonard and J. Tersoff. Role of Fermi-Level Pinning in Nanotube Schottky Diodes. *Physical Review Letters*, 84:4693–4696, 2000.

[15] J.J. Palacios, P. Tarakeshwar, and D.M. Kim. Metal Contacts in Carbon Nanotube Field-Effect Transistors: Beyond the Schottky Barrier Paradigm. *Physical Review B*, 77:113403, 2008.

[16] A.N. Andriotis, M. Menon, and G.E. Froudakis. Various Bonding Configurations of Transition-Metal Atoms on Carbon Nanotubes: Their Effect on Contact Resistance. *Applied Physics Letters*, 76:3890–3892, 2000.

[17] A.N. Andriotis, M. Menon, and G.E. Froudakis. Curvature Dependence of the Metal Catalyst Atom Interaction with Carbon Nanotubes Walls. *Chemical Physics Letters*, 320:425–434, 2000.

[18] P. Bai, E. Li, K.T. Lam, O. Kurniawan, and W.S. Koh. Carbon Nanotube Schottky Diode: An Atomic Perspective. *Nanotechnology*, 19:115203, 2008.

[19] A. Okada, S. Oshiyama. Electronic Structure of Semiconducting Nanotubes Adsorbed on Metal Surfaces. *Physical Review Letters*, 95:206804, 2005.

[20] K. Odbadrakh, P. Pomorski, and C. Roland. *Ab Initio* Band Bending, Metal Induced Gap States and Schottky Barriers of a Carbon and Boron Nitride Nanotube Device. *Physical Review Letters*, 73:233402, 2006.

[21] V. Vitale, A. Curioni, and W. Andreoni. Metal-Carbon Nanotube Contacts: The Link between Schottky Barrier and Chemical Bonding. *Journal of the American Chemical Society*, 130:5848–5849, 2008.

[22] F. Gao, J.M. Qu, and M. Yao. Electrical Contact Resistance at the Carbon Nanotube/Pd and Carbon Nanotube/Al Interfaces in End-Contact by First-Principles Calculations. *Journal of Electronic Packaging*, 133:020908, 2011.

[23] G. Lolli, L.A. Zhang, L. Balzano, N. Sakulchaicharoen, Y.Q. Tan, and D.E. Resasco. Tailoring (m,n) Structure of Single-Walled Carbon Nanotubes by Modifying Reaction Conditions and the Nature of the Support of CoMo Catalysts. *Journal of Physical Chemistry B*, 110:2108–2115, 2006.

[24] X.L. Li, X.M. Tu, S. Zaric, K. Welsher, W.S. Seo, W. Zhao, and H.J. Dai. Selective Synthesis Combined with Chemical Separation of Single-Walled Carbon Nanotubes for Chirality Selection. *Journal of the American Chemical Society*, 129:15770–15771, 2007.

[25] H. Wang, B. Wang, X.Y. Quek, L. Wei, J.W. Zhao, L.J. Li, M.B. Chan-Park, Y.H. Yang, and Y.A. Chen. Selective Synthesis of (9,8) Single Walled Carbon Nanotubes on Cobalt Incorporated TUD-1 Catalysts. *Journal of the American Chemical Society*, 132:16747–16749, 2010.

[26] K. Liu, Ph. Avouris, and R. Martel. Electrical Transport in Doped Multi-walled Carbon Nanotubes. *Physical Review B*, 63:161404, 2001.

[27] J.A. Talla. First Principles Modeling of Boron-Doped Carbon Nanotube Sensors. *Physica B*, 407:966–970, 2012.

[28] S.H. Lim, R. Li, W. Ji, and J. Lin. Effects of Nitrogenation on Single-Walled Carbon Nanotubes within Density Functional Theory. *Physical Review B*, 76:195406, 2006.

[29] A.C.M. Carvalho and M.C. dos Santos. Nitrogen-Substituted Nanotubes and Nanojunctions: Conformations and Electronic Properties. *Journal of Applied Physics*, 100:084395, 2006.

[30] C.-C. Kaun, B. Larade, H. Mehrez, J. Taylor, and H. Guo. Current-Voltage Characteristics of Carbon Nanotubes with Substitutional Nitrogen. *Physical Review B*, 65:205416, 2002.

[31] S. Latil, S. Roche, D. Mayou, and J.-C. Charlier. Mesoscopic Transport in Chemically Doped Carbon Nanotubes. *Physical Review Letters*, 92:256805, 2004.

[32] W.K. Hsu, S. Firth, Ph. Redlich, M. Terrones, H. Terrones, Y.Q. Zhu, N. Grobert, A. Schilder, Clark. R.J.H., H.W. Kroto, and D.R.M. Walton. Boron-Doping Effects in Carbon Nanotubes. *Materials Chemistry*, 10:1425–1429, 2000.

[33] W.Z. Liang, J.L. Yang, and J. Sun. Controllable p and n doping of Single-Walled Carbon Nanotubes by Encapsulation of Organic Molecules and Fullerene: A Theoretical Investigation. *Applied Physics Letters*, 86:223113, 2005.

[34] L.J. Li, A.N. Khlobystov, J.G. Wiltshire, G.A.D. Briggs, and R.J. Nicholas. Diameter-Selective Encapsulation of Metallocenes in Single-Walled Carbon Nanotubes. *Nature Materials*, 4:481–485, 2005.

[35] V. Meunier and B.G. Sumpter. Amphoteric Doping of Carbon Nanotubes by Encapsulation of Organic Molecules: Electronic Properties and Quantum Conductance. *Journal of Chemical Physics*, 123:024705, 2005.

[36] J. Lu, S. Nagese, X.W. Zhang, D. Wang, M. Ni, Y. Maeda, T. Wakahara, T. Nakahodo, T. Tsuchiya, T. Akasaka, Z.X. Gao, D.P. Yu, H.Q. Ye, W.N. Mei, and Y.S. Zhou. Selective Interaction of Large or Charge-Transfer Aromatic Molecules with Metallic Single-Walled Carbon Nanotubes: Critical Role of the Molecular Size and Orientation. *Journal of the American Chemical Society*, 128:5114–5118, 2006.

[37] J. Lu, S. Nagese, D.P. Yu, H.Q. Ye, R.S. Han, Z.X. Gao, S. Zhang, and L.M. Peng. Amphoteric and Controllable Doping of Carbon Nanotubes by Encapsulation of Organic and Organometallic Molecules. *Physical Review Letters*, 93:116804, 2004.

[38] T. Takenobu, T. Takano, M. Shiraishi, Y. Murakami, M. Ata, K. Katuara, Y. Achiba, and Y. Iwasa. Stable and Controlled Amphorteric Doping by Encapsulation of Organic Molecules inside Carbon Nanotubes. *Nature Materials*, 2:683–688, 2003.

[39] R.G.A. Veiga and R.H. Miwa. Ab Initio Study of TCNQ-doped Carbon Nanotubes. *Physical Review B*, 73:245422, 2006.

[40] T. Ozaki, K. Nishio, and H. Kino. Efficient Implementation of the Nonequilibrium Green Function Method for Electronic Transport Calculations. *Physical Review B*, 81:035116, 2010.

[41] www.openmx-square org.

[42] J.P. Perdew, K. Burke, and M. Ernzerhof. Generalized Gradient Approximation Made Simple. *Physical Review Letters*, 77:3865–3868, 1996.

[43] I. Morrison, D.M. Bylander, and L. Kleinman. Non-Local Hermitian Norm-Conserving Vanderbilt Pseudopotenial. *Physical Review B*, 47:6728–6731, 1993.

[44] T. Ozaki. Variationally Optimized Atomic Orbitals for Large-Scale Electronic Structures. *Physical Review B*, 67:155108, 2003.

[45] T. Ozaki and H. Kino. Numerical Atomic Basis Orbitals from H to Kr. *Physical Review B*, 69:195113, 2004.

[46] V. Zólyomi and J. Kürti. First-Principles Calculations for the Electronic Band Structures of Small Diameter Single-Wall Carbon Nanotubes. *Physical Review B*, 70:085403, 2004.

[47] A.M. Nemilentsau, M.V. Shuba, G.Y. Slepyan, P.P. Juzhit, S.A. Maksimenko, P.N. D'yachkov, and A. Lakhtaakia. Substitutional Doping of Carbon Nanotubes to Control their Electronmagnetic Characteristics. *Physical Review B*, 82:235424, 2010.

[48] X.M. Liu, H.R. Gutierrez, and P.C. Eklund. Electrical Properties and Far Infrared Optical Conductivity of Boron-Doped Single-Walled Carbon Nanotubes Films. *Journal of Physics-Condensed Matter*, 22:334213, 2010.

Chapter 6

Effect of Structure on Electronic Properties of the Iron-Carbon Nanotube Interface

6.1 Introduction

A detailed introduction to the current literature of metal-CNT interfaces is given in the Chapter 5 and in Section 2.8 of Chapter 2 to which the reader is referred for an in depth discussion. In this study we consider end contacts between the semiconducting (10,0)-CNT and several different iron electrode structures. Previous studies have considered the CNT embedded in the metal contact [1], we take a different approach and instead contact the CNT to a raised "bump" on the metal surface. We specifically choose iron as the metal contact because it is a commonly used CNT growth catalyst and such a configuration has previously been assessed experimentally for the frequently used growth catalyst Ni [2]. Additionally, we consider the B-doped (10,0)-CNT interface, again in end contact with iron metal.

6.2 Methods

Density functional theory (DFT) and the non-equilibrium Green function (NEGF) [3] method as implemented by the software package OpenMX [4] are

used to calculate the transport characteristics of the Fe-CNT interface. All calculations use the PBE [5] formulation of the generalised gradient approximation (GGA) exchange and correlation functional, along with norm conserving pseudopotentials [6]. We model the Fe-CNT interface by bonding directly a (10,0) CNT (pristine and boron doped (B-doped)) to an Fe slab. The Fe slabs consists of 7x7 (111) Fe, with an additional raised Fe "dock", used to sample varying contact configurations. In addition we consider two model systems: an iron nanowire and a small diameter CNT contacted to an iron nanowire. Full structural optimisations are carried out for all interfaces and the Fe and CNT leads, with the exception of Fe back plane, which is frozen for all interfaces until all forces are less than $5x10^{-4}$ Hartree/Bohr. The OpenMX code employs a linear combination of pseudoatomic orbitals method [7, 8], the pseudoatomic orbitals chosen for geometry optimisations are Fe6.0-s2p2d2 for iron, C4.5-s2p2 for carbon, B4.5s2p2 for boron and H4.0s2 for hydrogen. An energy cut-off of 150 Ry is used for numerical integration and supercells were chosen such that there was a minimum vacuum of 1 nm in all non-periodic directions.

The NEGF method is used to generate the transport characteristics. The basis sets used are Fe6.0-s2p2d1 for iron and C4.5-s2p1 for carbon, with B as before. A 128x128x128 grid is used for the numerical integration and the cell size is chosen such that there was 1 nm of vacuum in all directions perpendicular to the transport direction. The calculations are considered converged when the norm of the residual density matrix was below at least $1x10^{-4}$ and ideally below $1x10^{-6}$, although this stricter convergence criterium has negligible impact on the electronic properties. Transmission curves are obtained as follows, first, band structure calculations are performed for the left (Fe) and right (CNT) leads, generating the lead Hamiltonians. Next, the NEGF calculations are performed for structures consisting of theses leads and a central scattering region describing the interface. Finally NEGF results are used to generate the transmission with

the TranMain code. Additionally, we use the linear response method (assessed in Chapter 5) to generate IV characteristics for the Fe-B-doped CNT interface.

6.3 Model Systems

It is essential that the effect of spin polarisation, particularly in the vicinity of the Fermi level, on calculations involving iron are understood before drawing conclusions from closed shell calculations. Open-shell calculations greatly increase the cost of calculations, both in terms of memory requirements and computational time. Two model systems - a 6 Å diameter iron nanowire (FeNW) and the interface between a (5,0)-CNT and FeNW - are considered to study the importance of spin polarisation on the calculation of electron transport.

6.3.1 Iron Nanowire

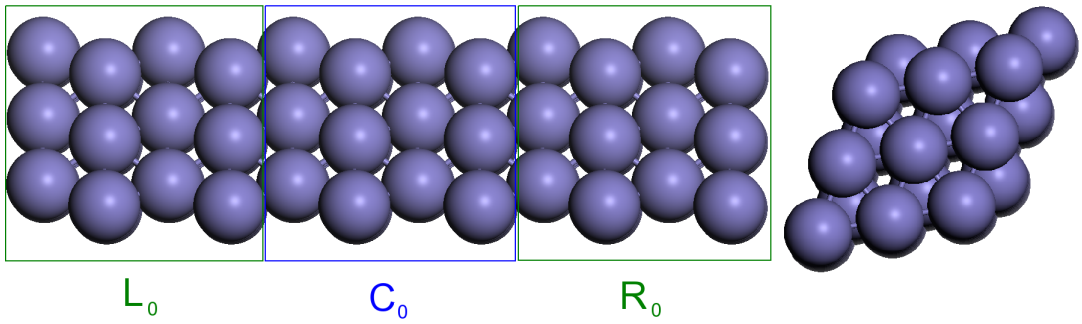


Figure 6.1: Side (left) and top (right) view of the FeNW structure, the Fe-Lead structure is equivalent to L_0 and the side view is labelled as in Figure 3.2

The FeNW structure is as illustrated in Figure 6.1. The FeNW-Lead structure which is used in the SCF calculations contains 36 iron atoms, while the full FeNW, used in NEGF calculations contains 3 FeNW-Lead repeat units consisting of 108 atoms. The band structures in Figure 6.2 show that the NW is metallic, as expected. Low lying bands near -50 eV are due to the 3p orbitals of iron. The full band structures indicate that the up and down spin bands of the open shell

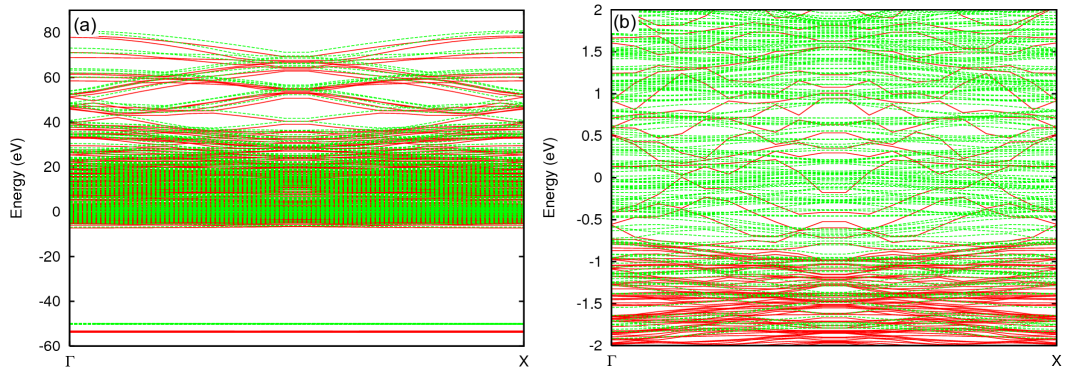


Figure 6.2: Band structure of open shell Fe Lead. (a) is the full band structure, showing that the up and down spin are shifted relative to one another. (b) is the band structure close to the Fermi level (0 eV), most bands crossing the Fermi level are of one spin.

calculation are similar to the closed shell case, with the notable difference that they are shifted with respect to each other. The band structures close to the Fermi energy indicate that the up bands are shifted down with respect to the closed shell case, while conversely the down bands are shifted to higher energy. The result is that at the Fermi energy, the majority of the bands are of a single spin in the open shell case.

Figure 6.3 shows the DOS close to the Fermi level for the FeNW-lead (SCF) and Fe-NW (NEGF) for the closed shell calculation, the corresponding open shell results are shown in Figure 6.4. The DOS resembles the band structure *i.e.* areas with dense bands have high DOS and vice versa. The shift seen in the band structures for open shell calculations is again seen in the DOS; the up DOS is shifted down by around 1 eV relative to the closed shell DOS, while the down DOS is conversely shifted up in energy by approximately the same amount. The DOS shows a peak around -55 eV, which totals 216 electrons (not seen Figures 6.3 and 6.4 as focus is placed on the region about the Fermi level), the total number of 3p electrons in the FeNW-lead confirming that the low lying bands are due to the 3p electrons.

From test calculations using large basis sets up to Fe6.0-s3p3d3f2 and VASP

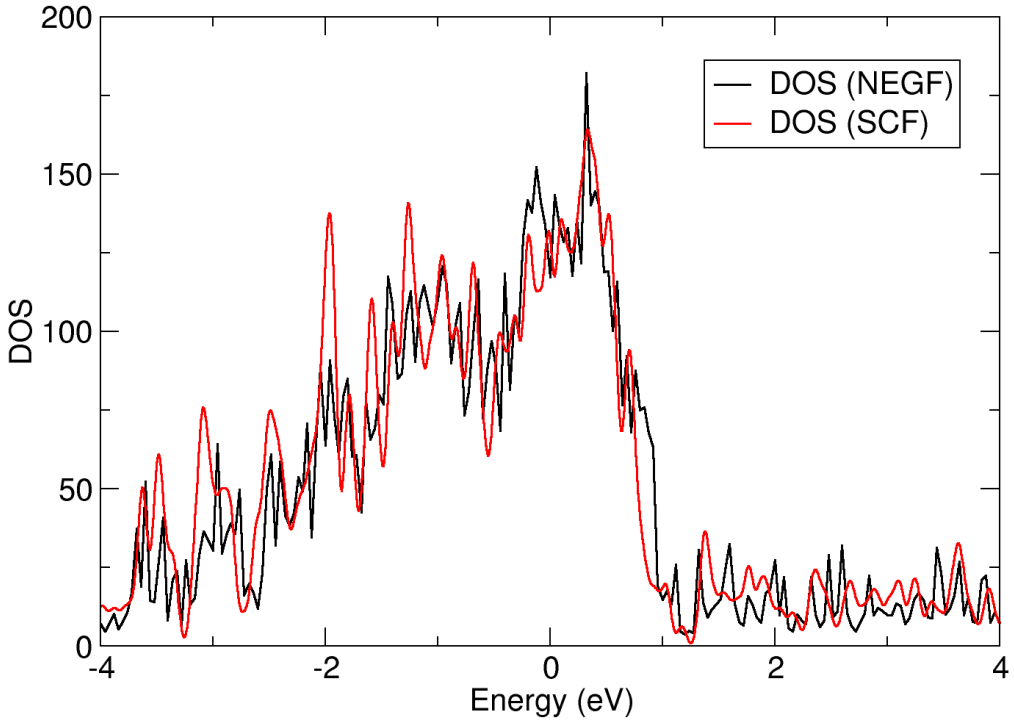


Figure 6.3: DOS of closed shell FeNW-Lead (SCF) and Fe-NW (NEGF) around the Fermi energy (0 eV). The NEGF DOS has been scaled to account for the differing number of Fe atoms in FeNW and FeNW-lead the calculations.

plane wave results, a spin per Fe atom of 2.8-2.9 was anticipated. In the case of the open shell FeNW-lead, we find an average spin of 2.85 (varying from 2.6 to 3.2) so in spite of restricted basis set size (s2p2d1), the spin is well described. Again, in the spin polarised NEGF FeNW calculation, the Fe spin is well described with an average spin of 2.86, ranging from 2.6 to 3.3. Obtaining NEGF results (closed shell and polarised) with similar DOS to the SCF FeNW-lead proved more difficult than had been anticipated. Initially, very different DOS results were obtained for NEGF than in the lead calculations and in addition the Fe spin was incorrect. Adjusting input parameters to increase the accuracy of the calculation by increasing the grid size for numerical integration resulted in correct spin for the spin polarised NEGF calculation and also good agreement in DOS for the SCF and NEGF calculations. The most important input parameters in OpenMX for controlling the accuracy of the calculation are “NEGF.NUM.Poles”

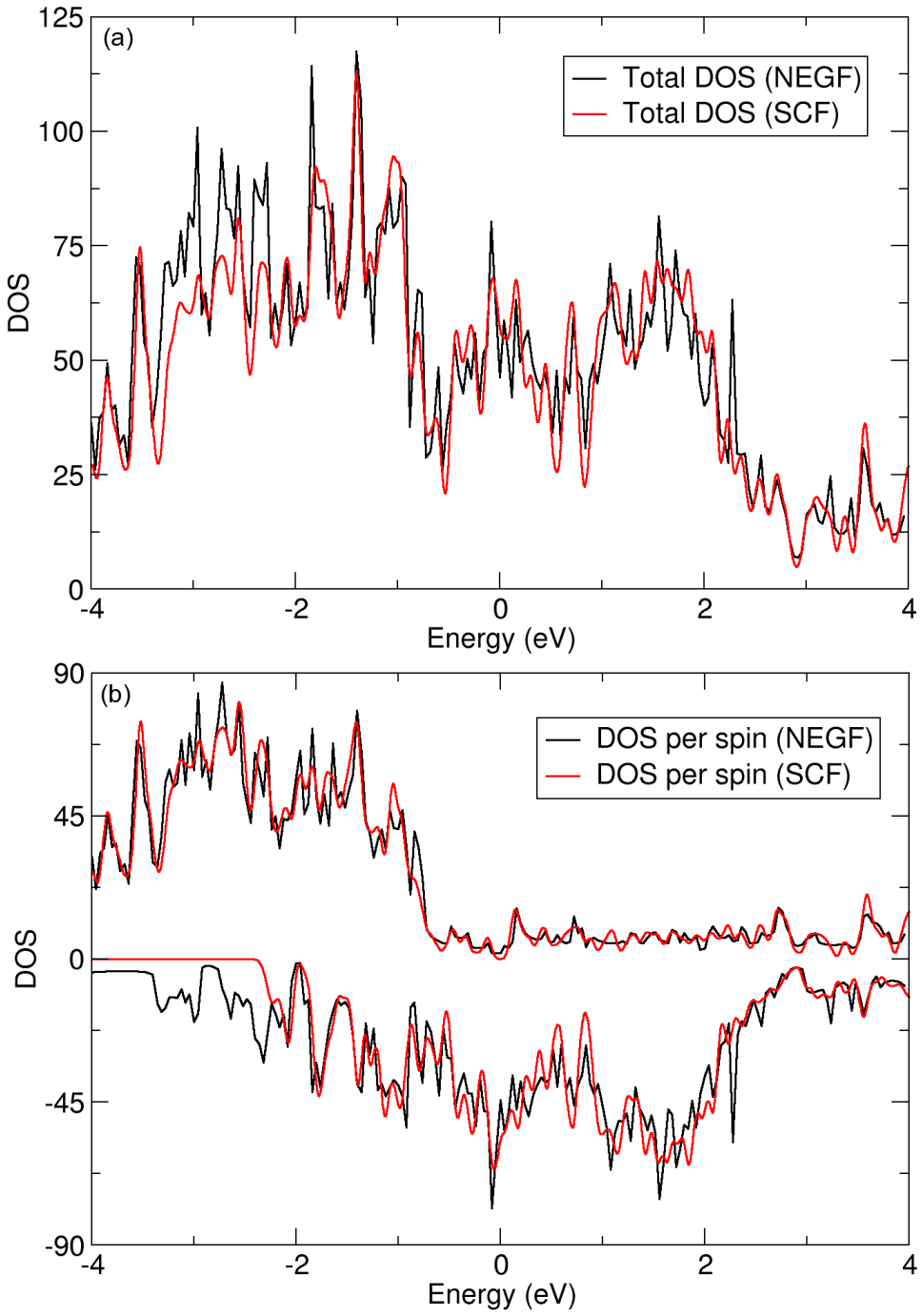


Figure 6.4: (a) Total DOS for open shell Fe-Lead SCF and Fe-NW NEGF calculations. (b) Contribution to total DOS from each spin for both calculations. The Fermi energy is at 0 eV and the NEGF DOS has been scaled to account for the different number of atoms in the Lead and NW structures, which are calculated using periodic boundary conditions and self-enegeries, respectively.

and "scf.Ngrid" which control the number of poles in the calculation of the Fermi-Dirac function and and the size of the numerical integration grid, respectively.

6.3.2 FeNW-(5,0)-CNT Interface

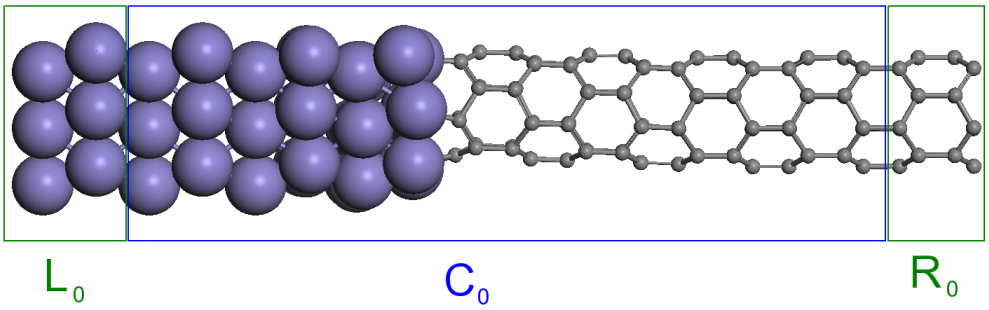


Figure 6.5: Structure of the (5,0)-FeNW scattering region, the labelling is as explained in Figure 3.2. Fe is purple and C is grey.

The Fe-(5,0)-CNT interface provides a more realistic model of the Fe-(10,0)-CNT interface we wish to study than the Fe-NW while still being computationally tractable for both closed and open shell calculations. The pristine (5,0)-CNT exhibits a vanishingly small band gap. This result is not unexpected as CNT electronic properties contrary to the simple zone-folding picture which predicts that the (5,0)-CNT should be a semi-conductor have previously been reported for narrow diameter CNTs [9, 10]. The total DOS of the Fe-CNT interface is dominated by iron and as a result closely resembles the DOS of the FeNW (compare Figure 6.6 (a) with Figures 6.3 and 6.4). Spin polarisation of the CNT atoms is negligible even at the interface, although up and down spin DOS do differ slightly at the Fermi level for carbon bonded to iron. Far from the interface up and down spin DOS are very similar and the open and closed shell DOS agree closely (Figure 6.6 (b)). Transmission close to the Fermi level is relatively low for both the open and closed shell cases (Figure 6.7) and is similar in both cases. In addition the transmission results are dominated by the CNT. Figure 6.8 shows the IV curves obtained using the linear response method for the closed and open

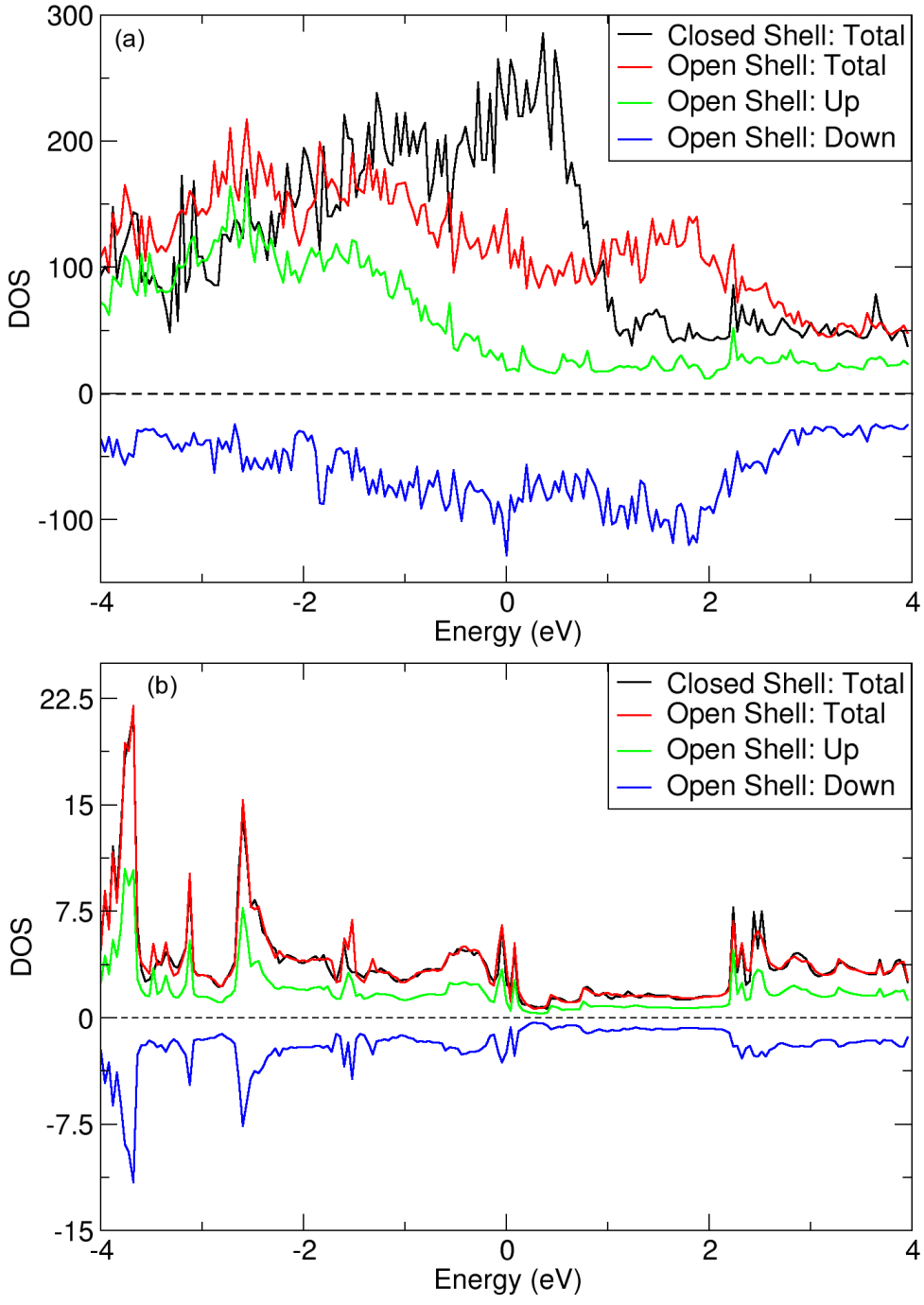


Figure 6.6: (a) Total DOS for the (5,0)-FeNW system for polarised (open shell) and unpolarised (closed shell) NEGF calculations. (b) DOS for the repeat unit of the CNT furthest from the interface for the polarised and unpolarised case.

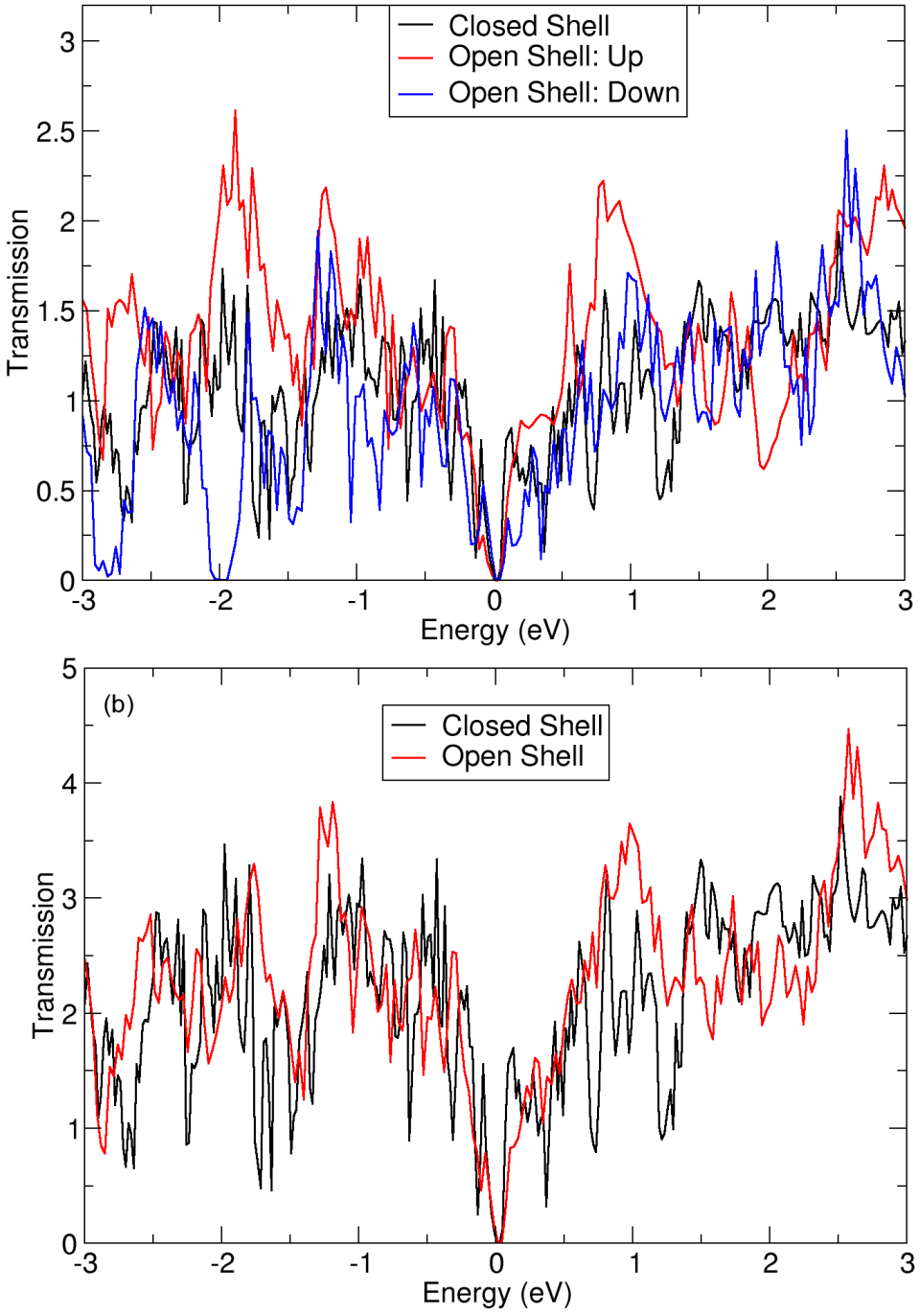


Figure 6.7: Transmission of the (5,0)-FeNW system. (a) Transmission per spin channel for closed and open shell calculations of the (5,0)-FeNW system. (b) Total transmission for both open and closed shell calculations.

shell calculations. There is good agreement between the closed and open shell currents, with the closed shell current less than 40% larger. These results suggest that, provided the iron DOS is larger than the CNT DOS close to the Fermi level, closed shell calculations provide a reasonable approximation to open shell transmission calculations in the vicinity of the Fermi level.

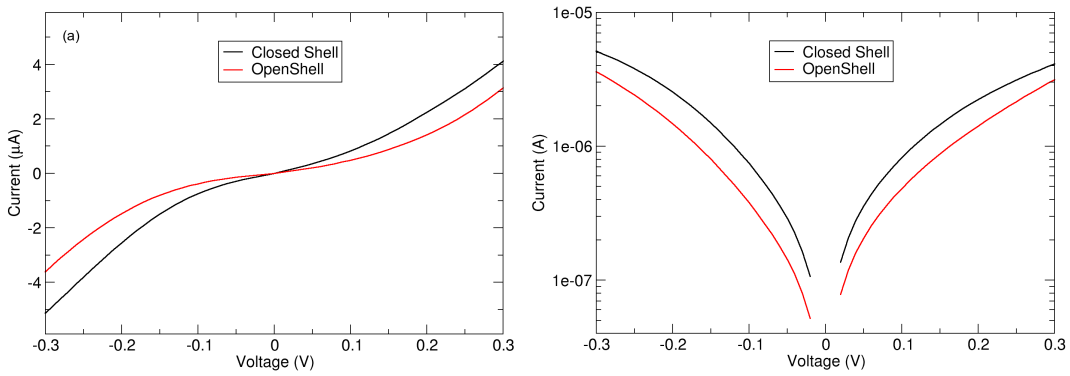


Figure 6.8: (Comparison of the IV curves obtained for the closed and open shell (5,0)-FeNW using (a) linear scale and (b) log scale.

6.4 Fe-(10,0)-CNT Interface

Structures for varying Fe-CNT interfaces are given in Figure 6.9. Following the discussion of the previous section, all calculations of the Fe-(10,0)-CNT interfaces are spin unpolarised. In spite of the differing structures of interface 1 and 2 (rounded and flat respectively), the average length of the Fe-C bonds is similar being 1.960 Å for interface 1 and 1.924 Å for interface 2. The range of Fe-C bonds lengths is larger for interface 2 than for interface 1, thus the interface structure is less uniform for interface 2. The structure of the B-doped CNT/Fe interface is based on interface 1 and unsurprisingly, the bonding at this interface is very similar to interface 1, with an average bond length of 1.972 Å. In all cases Mulliken population analysis shows that charge is transferred from Fe to the CNT. A larger charge transfer takes place for interface 1 (∼2.1e) than interface 2 (∼1.4e), which is presumably due to the differences in the interface structures.

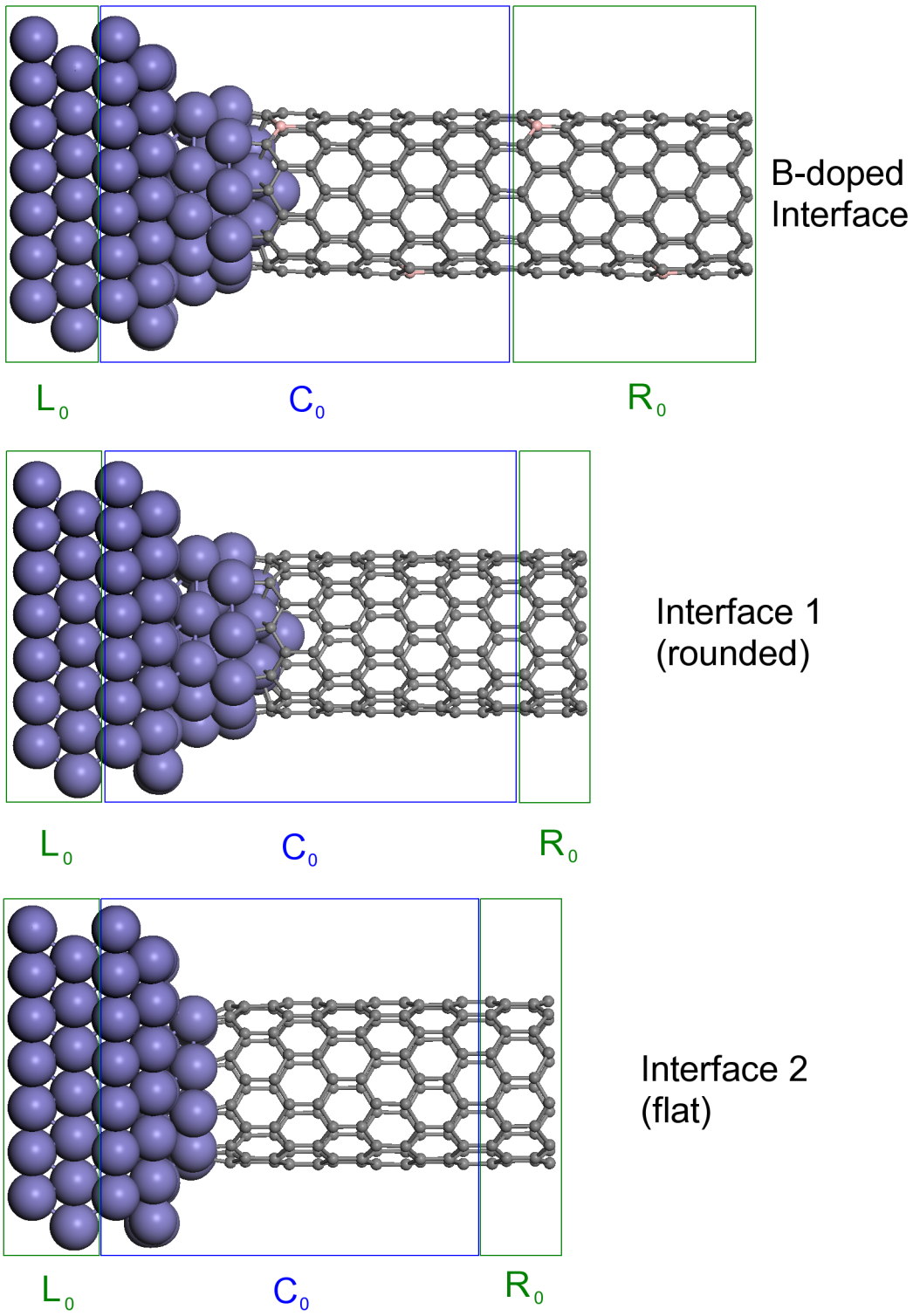


Figure 6.9: Structure of the (10,0)-Fe scattering region, the labelling is as explained in Figure 3.2. The top figure is the B-doped interface. The middle figure is Interface 1 and the bottom figure is Interface 2. Fe is purple, C is grey and B is pink.

Two of the carbon atoms at the interface between the B-doped CNT and Fe also bond to boron, which complicates the charge transfer at this interface, however total charge transfer to the CNT (∼2.2e) is very similar to interface 1, as would expected given the structural similarities.

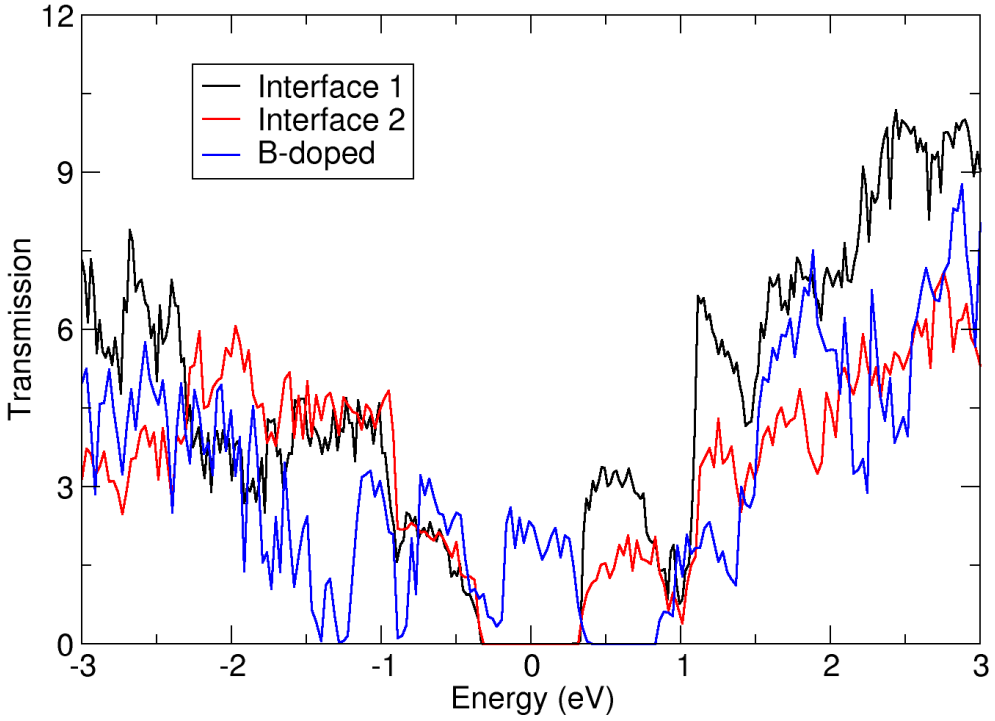


Figure 6.10: Transmission of the (10,0)-FeNW systems. The Fermi energy is 0 eV.

The size of the CNT gap and the position of the Fermi energy appear to be relatively insensitive to the exact structure of the interface. This can be seen in the zero-bias transmissions of interface 1 and interface 2 shown in Figure 6.10, where the gaps in transmission associated with the isolated CNT gap coincide. Up to ∼-2 eV below the Fermi energy, the transmissions for interface 1 and 2 are similar, beyond this point they differ with transmission for interface 1 becoming larger than interface 2 at lower energies. Above the Fermi energy transmission for interface 1 is at the majority of points greater than interface 2. In particular, close to the Fermi energy we see significantly larger transmission for interface 1. This difference in transmission is presumed to be related to the differences in structure

and charge transfer at the interfaces. From this result, it is to be anticipated that structural changes may lead to alteration of the IV characteristics of Fe-CNT devices.

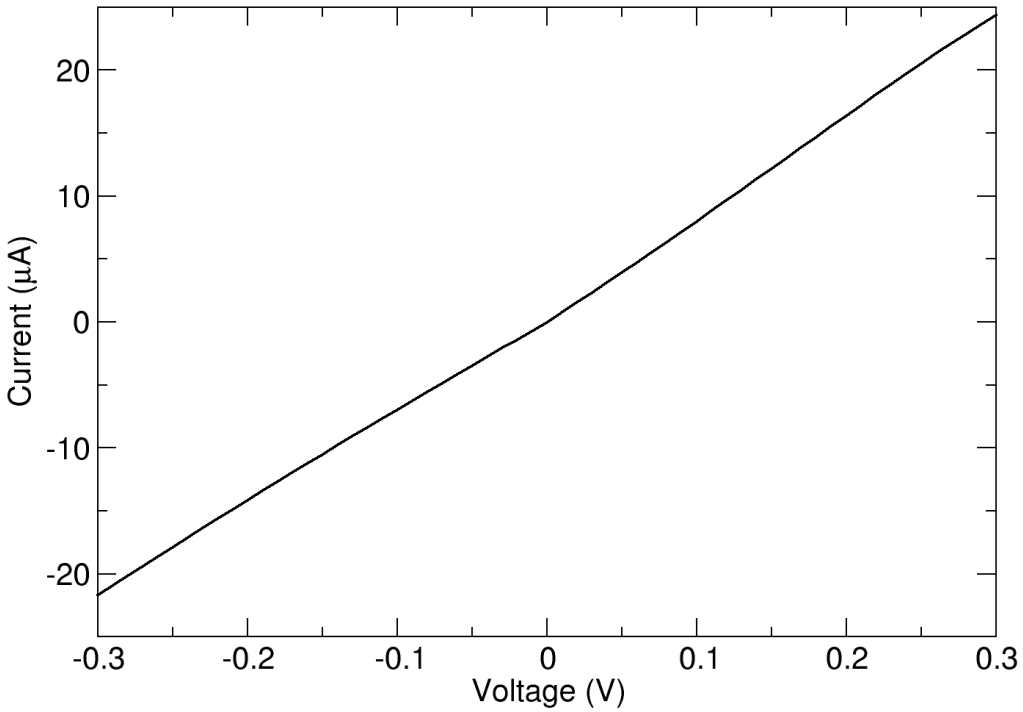


Figure 6.11: Linear Response IV curve for B doped-CNT Fe interface around the Fermi energy (0 eV), corresponding to a resistance of R $\approx$ 6 kΩ

Much like the behaviour of the B-doped (16,0)-CNT in Chapter 5, the B-doped (10,0)-CNT is metallic, with gap of the undoped CNT pushed above the Fermi energy and also reduced slightly in extent, this is reflected in the transmission of the B-doped CNT seen in Figure 6.10. The transmission of the B-doped interface is lower than that of interface 1 through most of the region close to the Fermi energy with the exception of region of zero transmission for interface 1 which results from the CNT band gap. There are no significant differences in the interfacial structures or charge transfer and thus this difference in transmission is caused by the presence of B in the CNT, which acts as a defect in the ideal CNT structure. This reduced transmission on incorporation of a substitutional dopant is consistent with literature reports of poorer electronic properties

of substitutionally doped CNTs [11, 12].

As discussed in Chapter 5, there is a reasonable agreement between NEGF and linear response IV curves. The voltage region found to give reasonable accuracy is in the range of zero transmission for interface 1 and 2 and so the linear response IV is considered for the B-doped CNT/Fe interface only as shown in Figure 6.11. A linear IV curve is obtained which is suggestive of Ohmic contact formation at this interface. Thus, it may indeed be possible to reliably produce Ohmic contacts with CNTs through doping, although further research for doped armchair and chiral CNTs is necessary to establish this point explicitly for a wider range of CNTs chiralities.

6.5 Conclusion

We have found spin polarisation not to be critical for transmission or linear response IV close the the Fermi level for the Fe-CNT junction. The exact structure of the Fe-CNT end contact is found to affect neither the position of the Fermi energy nor the extent of the region of zero transmission for the interfaces studied. However, changes in the structure of the interface are found to impact on the transmission of the Fe-CNT interface. On doping with boron, the (10,0)-CNT is found to become metallic but overall transmission is reduced relative to the undoped CNT. We obtain a linear IV curve for the interface between the boron doped CNT and iron nanowire which demonstrates the formation of an Ohmic contact and at the Fermi level we find a resistance of 6 kΩ.

6.6 References

[1] P. Bai, E. Li, K.T. Lam, O. Kurniawan, and W.S. Koh. Carbon Nanotube Schottky Diode: An Atomic Perspective. *Nanotechnology*, 19:115203, 2008.

[2] C. Santini, A. Volodin, C. Van Haesendonck, S. De Gendt, G. Groeseneken, and P.M. Vereecken. Carbon Nanotube-Carbon Nanotube Contacts as an Alternative towards Low Resistance Horizontal Interconnects. *Carbon*, 49:4004–4012, 2011.

[3] T. Ozaki, K. Nishio, and H. Kino. Efficient Implementation of the Nonequilibrium Green Function Method for Electronic Transport Calculations. *Physical Review B*, 81:035116, 2010.

[4] www.openmx-square org.

[5] J.P. Perdew, K. Burke, and M. Ernzerhof. Generalized Gradient Approximation Made Simple. *Physical Review Letters*, 77:3865–3868, 1996.

[6] I. Morrison, D.M. Bylander, and L. Kleinman. Non-Local Hermitian Norm-Conserving Vanderbilt Pseudopotenial. *Physical Review B*, 47:6728–6731, 1993.

[7] T. Ozaki. Variationally Optimized Atomic Orbitals for Large-Scale Electronic Structures. *Physical Review B*, 67:155108, 2003.

[8] T. Ozaki and H. Kino. Numerical Atomic Basis Orbitals from H to Kr. *Physical Review B*, 69:195113, 2004.

[9] I. Cabria, J. W. Mintmire, and C. T. White. Metallic and Semiconducting Narrow Carbon Nanotubes. *Phys. Rev. B*, 67:121406, 2003.

[10] V. Barone and G.E. Scuseria. Theoretical Study of the Electronic Properties of Narrow Single-Walled Carbon Nanotubes: Beyond the Local Density Approximation. *Journal of Chemical Physics*, 121:10376, 2004.

[11] C.-C. Kaun, B. Larade, H. Mehrez, J. Taylor, and H. Guo. Current-Voltage Characteristics of Carbon Nanotubes with Substitutional Nitrogen. *Physical Review B*, 65:205416, 2002.

[12] S. Latil, S. Roche, D. Mayou, and J.-C. Charlier. Mesoscopic Transport in Chemically Doped Carbon Nanotubes. *Physical Review Letters*, 92:256805, 2004.

Chapter 7

Divacancies in Carbon Nanotubes and their Influence on Electron Scattering

7.1 Introduction

Nanosize materials have received much interest in recent years from both a scientific and technological standpoint. Quasi one-dimensional materials, including carbon nanotubes (CNTs), are an exciting prospect because the large aspect ratios associated with such materials are ideally suited to use in a range of technological applications. In particular, CNTs exhibit ballistic conductance and nearly defect free structures which ideally suits them for use in nanoelectronics, for example as interconnects [1–3]. The low dimensionality responsible for the excellent properties of CNTs is however not without challenges. Dramatic changes in physical and chemical properties can manifest due to the introduction of defects. Additionally, even high quality CNTs have one defect on average every 4 μm [4]. Such changes in properties are not necessarily detrimental. Enhanced surface reactivity is often found in defective CNTs, which has led to interest in their use as gas sensors [5–7]. Defect mediated modification of CNT mechanical strength has also been reported [8–10]. Defects occur during the CNT growth process but can also be

induced during post-processing by ion irradiation and acid treatment and thus CNT properties may be tailored [11] if the effects of defects are well understood.

The low dimensionality of CNTs means propagation occurs almost exclusively along the tube axis because the charge carriers are strongly confined and as a consequence scattering at defects is unavoidable. CNT resistance has been shown to increase exponentially as CNT length increases [12, 13] and occurs when device lengths are a multiple of the mean free path (λ - the average distance travelled by an electron between scattering events). This is a manifestation of the metal-insulator transition due to Anderson Localisation [14], which is due to the effect of disorder on electron transport in low dimensional systems.

Following ion irradation, the most commonly observed defects in CNTs are vacancies [15]. Large vacancies are energetically unstable in CNTs and tend to split into pentagon-heptagon pairs [16] and so we focus in this work on mono-vacancies and divacancies where one or two carbon atoms are missing from the CNT lattice respectively. Mono- and divacancies in small diameter CNTs have been studied in detail within density functional theory (DFT). The divacancy defect has been found to be more stable than two isolated monovacancies [17, 18], which taken with the relatively low barrier to migration of monovacancies [19], suggests a tendency towards monovacancy coalescence. In CNTs and graphene, the monovacancy defect relaxes from an initial twelve-membered ring into a five- and nine-membered ring pair [17, 18, 20, 21]. The divacancy defect can adopt several configurations in CNTs and graphene including the 585 and 555777 structures. Initially, the ruptured CNT sidewall on divacancy formation relaxes to a 585 defect consisting of an octagon bordered by two pentagons. A bond rotation in the 585 defect (similar to the formation of a Stone-Wales defect in a pristine CNT) results in formation of the 555777 defect consisting of a circular motif of alternating pentagons and heptagons. In planar graphene, the 555777 defect is more stable than the 585 [22]. The curvature of the CNT complicates this picture,

with the 585 defect being the more stable for the narrow diameter CNTs previously studied [17]. Using molecular mechanics calculations the 555777 divacancy has been predicted to become more stable than the 585 at diameters above 40 Å for armchair CNTs [17].

In this work, we extend *ab initio* knowledge of vacancy defects in CNTs to large diameter CNTs of up to 40 Å diameter not previously studied within DFT. Formation energies of the defects are calculated and the cross-over in stability of the 585 and 555777 defects is confirmed from first principles to occur at diameters above 40 Å. For these systems, the electronic properties including electron transmission, mean free path and resistance of defects in technologically important large diameter CNTs are calculated.

7.2 Methods

7.2.1 Electronic Structure Calculations

Electronic structure calculations and geometry optimisations are performed using DFT as implemented by the OpenMX package [23]. We use the Ceperley-Alder formulation [24] of the local density approximation (LDA) for the exchange and correlation functional. A numerical pseudo-atom orbital (PAO) [25] basis along with norm-conserving pseudopotentials [26] are used to describe the electrons. Carbon PAOs with a cut-off radius of 5.5 Bohr optimised to the CNT environment are generated for the pristine $(5, 5)$- and $(10, 0)$-CNTs and used for all armchair and zigzag CNTs, respectively. The supercell size was chosen such that the vacuum in the non-periodic directions was at least 1 nm leading to cell cross sections of 18 Å x 18 Å to 53 Å x 53 Å for armchair CNTs and from 21 Å x 21 Å to 37 Å x 37 Å for zigzag CNTs. A 4x1x1 Monkhorst-Pack grid along the CNT axis is used for k-point sampling [27] and geometries are optimised until the maximum force is below 0.005 eV/Å. The armchair CNTs used in this study

are $(5,5)$, $(7,7)$, $(10,10)$, $(20,20)$ and $(30,30)$ and the zigzag CNTs chosen are $(10,0)$, $(20,0)$, $(30,0)$. Defects are introduced by removing the carbon atoms before geometry optimisation and, in the case of the 555777 defect, the atoms at the defect site are also rearranged before geometry optimisation.

7.2.2 Calculation of Transport Properties

The TIMES (Transport In MEsoscopic Systems) [28–30] package is used to calculate transmission in the defective CNTs using the matrix representations of the electronic structures obtained from OpenMX calculations. TIMES uses a Green's function method to calculate the total channel transmission from the quantum mechanical scattering matrix and within the Landauer formalism used, the transmission is the low-bias, low-temperature conductance in units of $2e^2/h$. This conductance can be used to calculate the mean free path (MFP) for defect scattering [30, 31], as described in the Section 7.2.3.

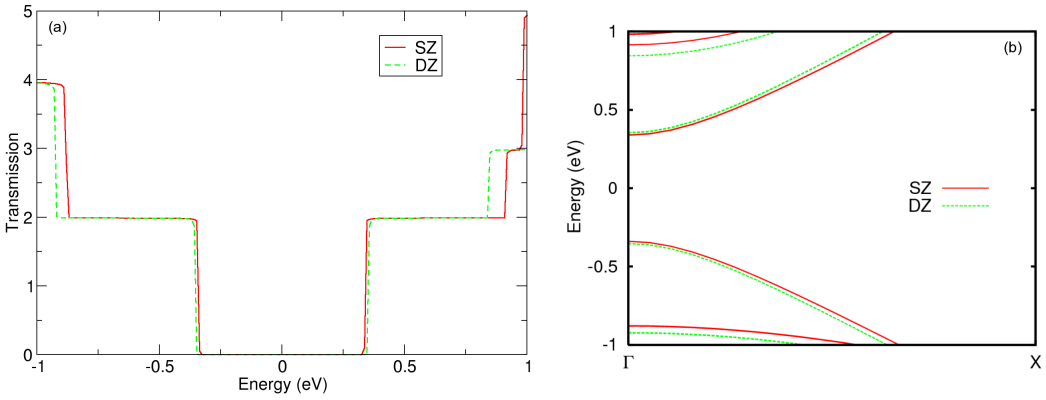


Figure 7.1: Transmission (a) and band structure (b) of the (10,0)-CNT for single and double zeta basis sets

The supercells used in the single point calculations for the $(n,0)$ and (n,n) CNTs to generate the Hamiltonian for TIMES contain 13 CNT units cells when $m \leq 10$ and 7 CNT unit cells when $m \geq 20$, with the defect at centre of the cell. As a result, the full scattering region extends to at least three times the size of

an individual defect. The number of atoms in the simulation cell ranges from less than 500 atoms for the small diameter CNTs to more than 1300 atoms for the largest CNTs considered in this study. Calculations involving the large diameter CNTs are computationally demanding both in terms of memory requirements and runtime. We therefore use a single zeta quality basis set in OpenMX to obtain the matrix representation of the electronic structure for TIMES to reduce the computational overhead of these simulations. To justify the use of the minimal basis set for transport calculations, the transmission and band structure are calculated using single and double zeta basis sets for the (10,0)-CNT with similar results obtained for the basis sets (Figure 7.1). The validity of the approach of using a minimal basis set for transmission calculations while using a larger basis set for geometry optimisation has previously been reported in the literature for CNT/graphene systems [32].

7.2.3 Estimation of Mean Free Path

To calculate the mean free path λ as a function of distance between defects l_d from the electronic transmission T results from individual defects, the method proposed by Markussen and co-workers is followed [33]. The ratio of λ to the length of a conductor L is proportional to T in the diffusive regime. This ratio (to a first approximation) is the transmission probability of each channel and for N_{ch} channels:

$$T = N_{ch}\left(\frac{\lambda}{L}\right) \tag{7.1}$$

when $L >> \lambda$. The resistance of such a conductor (R) is proportional to the inverse of T and

$$R = R_c \left(\frac{L}{\lambda} \right), \tag{7.2}$$

where R_c is the quantum unit of resistance times the number of channels and is given by:

$$R_c = \left(\frac{h}{2e^2} \right) N_{ch}. \tag{7.3}$$

The independent scattering approximation (ISA) assumes that scattering resistances from individual defects can simply be added together classically as per Ohm's Law. Then, if each defect has the same scattering resistance R_s, the total conductor resistance becomes:

$$R = R_c + R_s \left(\frac{L}{l_d} \right) \approx R_s \left(\frac{L}{l_d} \right) \tag{7.4}$$

where L/l_d is the number of defects in the conductor. Finally, comparison of equations 7.2 and 7.4 yields an expression for λ as a function of l_d :

$$\lambda = \left(\frac{R_c}{R_s} \right) l_d \tag{7.5}$$

with

$$R_s = \left(\frac{h}{2e^2} \right) \frac{1}{T} - \left(\frac{h}{2e^2} \right) \frac{1}{N_{ch}}. \tag{7.6}$$

All terms in equations 7.5 can be obtained from *ab initio* electron transport simulations and thus the mean free path as a function of distance between defects can be calculated.

7.3 Defective CNT Structures

7.3.1 Defects in Zig-Zag CNTs

The defects considered in the $(10, 0)$-, $(20, 0)$- and $(30, 0)$-CNTs are the monovacancy (mv) defect and two orientations of the 585 divacancy defect - the lateral divacancy (ldv) and vertical divacancy (vdv). The difference in the two 585 structure is in the location of the two removed carbon atoms. In the lateral divacancy they are adjacent to each other along the tube axis whereas they are adjacent perpendicular to the tube axis in the vertical divacancy as illustrated in Figure 7.2. The rearranged 555777 divacancy defect is not considered for the zig-zag CNTs because it is predicted [17] to become more stable than the 585 defect at diameters above 57 Å in zigzag CNTs and such structures are larger than we can practically study within DFT. In all cases, the zigzag CNT does not deviate strongly from its cylindrical structure on introduction of the vacancy defects studied, although there is a localised reduction in CNT diameter in the vicinity of the vacancy defect. Local diameter reduction due to the presence of vacancy defects has also been reported in the literature for the (5,5) and (10,10) armchair CNTs [34].

The monovacancy defect exhibits a similar pattern of bonding in all three zigzag CNTs - it reconstructs to a 5- and 9-membered ring pair, as illustrated for the (10,0)-CNT in Figure 7.2. The sides of the pentagon are not uniform in length. The side perpendicular to the tube axis, which is also part of the nine-membered ring, is longest and the length of this bond increases as CNT diameter increases. Due to the plane of symmetry passing perpendicular to this bond, all other bonds in both the 5- and 9-membered ring occur in pairs of similar length. The average bond length in the pentagon decreases as CNT diameter increases, while those in the nine-membered ring increase. Bonds between atoms which are part of the defect (marked yellow in Figure 7.2) to the rest of the CNT are

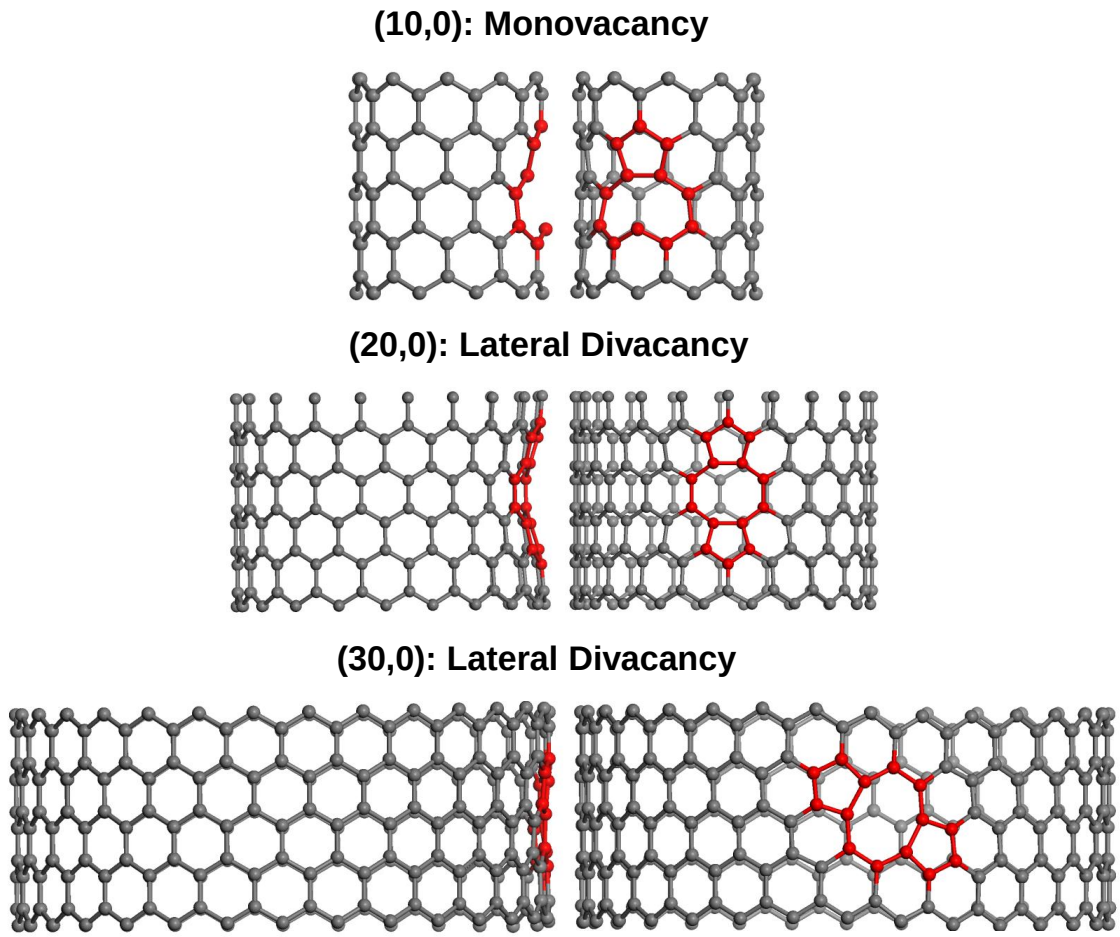


Figure 7.2: Defects in zig-zag CNTs. The monovacancy defect is shown in the $(10, 0)$-CNT, the lateral divacancy in the $(20, 0)$-CNT and the vertical divacancy in the $(30, 0)$-CNT.

broadly similar in all cases and the size of the defect does not vary significantly with CNT diameter.

The lateral divacancy has two planes of symmetry, one passes along its length parallel to the CNT axis and the other passes through the 8-membered ring perpendicular to the CNT axis. For the CNTs studied, the bonding within the defect reflects this symmetry well. Like the monovacancy, the C-C bonds shared by the rings are elongated (although to a lesser degree than in the monovacancy), the average bond length in the 8-membered rings decreases with CNT diameter while that in the 5-membered ring is independent of diameter. Again, the bonds

to atoms outside the defect are similar as is the extent of the defect irrespective of chirality.

The vertical divacancy makes an angle with the CNT axis (as can be seen in Figure 7.2) and as a result the symmetry of the bonds seen in the vertical divacancy is lost. The average bond length in the 5-membered rings this time increases slightly with CNT diameter while that in the 8-membered ring is almost constant. The bonds from atoms in the defect to the rest of the CNT are again much the same for all diameters. Note that the local diameter reduction clearly visible in Figure 7.2 for the lateral divacancy does not occur for the vertical divacancy.

7.3.2 Defects in Armchair CNTs

The monovacancy and all three divacancy - lateral, vertical and 555777 - are studied in the armchair CNTs. Unlike the zig-zag CNTs, the small diameter armchair CNTs are deformed by the addition of the vacancy defect. This is most severe in the $(5, 5)$-CNT with the monovacancy and vertical divacancy as in Figure 7.3, but also occurs for the $(7, 7)$-CNT. However the bonding at the defects remains similar for all chiralities despite this deformation.

Due to its orientation to the CNT axis, the monovacancy loses symmetry unlike in the zig-zag CNTs. As before, the bond shared between the 5- and 9-membered rings is elongated and it lengthens further as CNT diameter increases. The average bond length in both the 5- and 9-membered rings increases as the diameter increases and again the bonds between defect atoms and the rest of the CNT are not strongly influenced by CNT diameter.

The lateral divacancy presents a more complicated picture, the general trend is that bonds in both the 5- and 8-membered ring elongate as the CNT diameter increases. The lengths of the bonds shared with the 8-membered ring also increase with CNT diameter and once again the bonds joining the rest of the CNT are

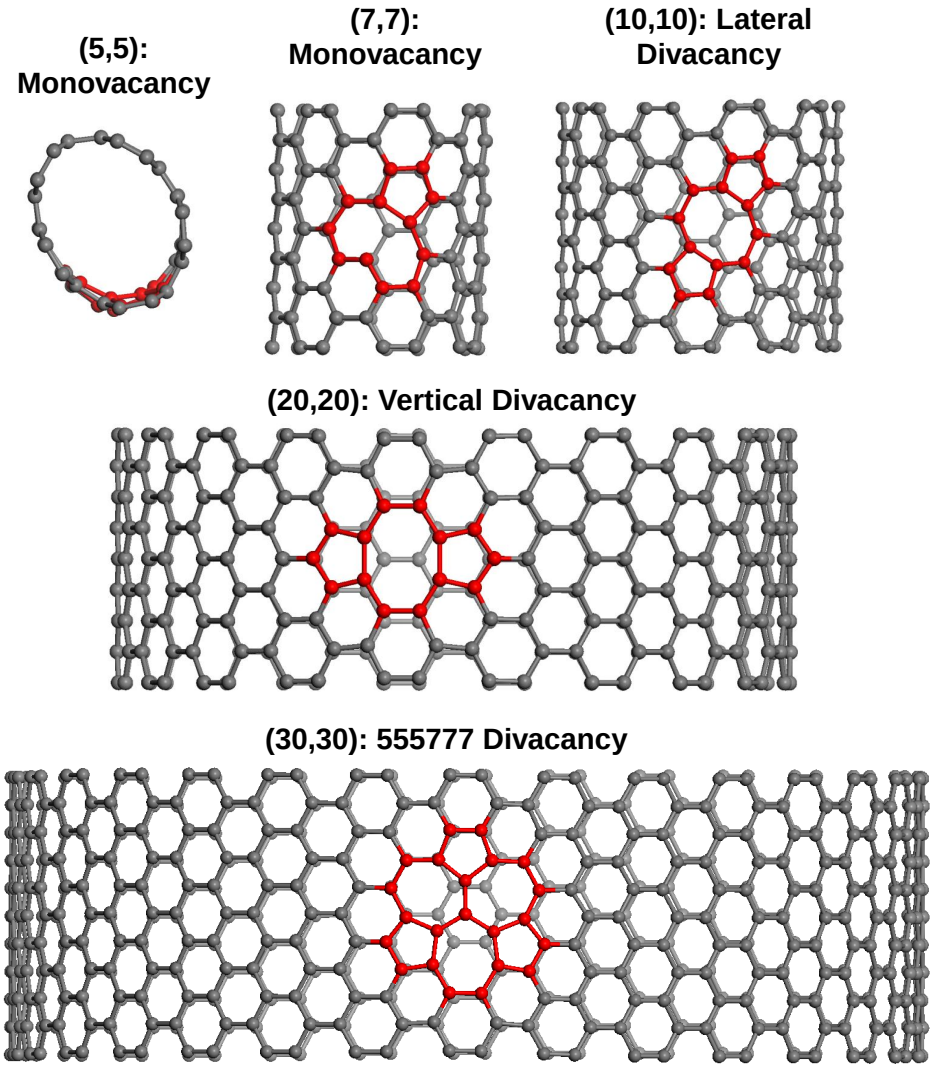


Figure 7.3: Defects in armchair CNTs. The monovacancy defect is shown in the $(5,5)$- and $(7,7)$-CNT, the lateral divacancy in the (10,0)-CNT, the vertical divacancy in the (20,0)-CNT and the 555777 divacancy in the (30,30)-CNT

not influenced by the CNT diameter. Like the lateral divacancy in the zig-zag CNTs, the vertical divacancy has two symmetry planes within the CNT and the structure of the defect is as a result highly symmetric. The average bond lengths within the 5- and 8-membered rings follow a similar pattern; average bond length increases and reaches a maximum for the $(10,10)$-CNT before again decreasing. A similar pattern is seen for the carbon bonds shared by the rings. The unusual bonding pattern is possibly related to the deviation from the ideal cylindrical CNT structure for the $(5,5)$- and $(7,7)$-CNT. The 555777 defect has

similar symmetry within the armchair CNT as the vertical divacancy and, as with previous symmetric defects, exhibits a symmetric bonding pattern.

7.3.3 Defects in Graphene

The monovacancy defect does not reconstruct to the 5- and 9-membered ring seen in the CNTs. TEM imaging has shown this reconstruction does take place in graphene [21]. There are a number of possible reasons why we do not see this reconstruction in our calculations for graphene. The real graphene structure is not completely planar, *i.e.* there are bumps and dips in the structure. It is not possible to include such non-periodic behaviour in our periodic calculations. We use a cell size of 34 Å x 34 Å for all the graphene calculations, this could prevent relaxation of the defect structure by preventing localised "shrinkage" of the graphene near the defect in an analogous fashion to the localised diameter reduction we see for the CNTs. In the planar graphene structure the lateral and vertical divacancies are reduced to a single 585 divacancy. The bonding in this divacancy follows a similar pattern to that seen in the 585 divacancies in the CNTs. The bond lengths within the divacancy are similar to those found in the divacancies in the larger diameter CNTs with the exception of the bonds between the bridgehead carbon atoms, which are consistently shorter in the lateral divacancy than in the vertical divacancy and the 585 divacancy in graphene. The 555777 defect has greater symmetry in the planar graphene structure than in the armchair CNT; the 5- and 7-membered rings are identical by symmetry. As a result the bonding is more symmetric than found in the armchair CNTs, with the greatest differences in bonding unsurprisingly occurring for the high-curvature, small-diameter CNTs.

7.4 Defect Formation Energies

The formation energies of each defect in the CNTs and in graphene are calculated, in addition we calculate the relative stabilities of the various defects. We calculate formation energies in two different ways. Firstly, we calculate the formation energy in the manner used in the literature for armchair CNTs up to (10,10) [17, 18] and zigzag CNTs up to (18,0) [17]. This formation energy (ΔE_C) is found by considering the difference in energy between the pristine CNT and the defective CNT and n carbon atoms where n is 1 for monovacancies and 2 for divacancies:

$$\Delta E_C = |E_{pristine} - (E_{defect} + nE_{carbon})|. \tag{7.7}$$

A smaller formation energy therefore implies that a particular defect is more stable. However the fragmentation process of C_{60} and other larger fullerenes is known to proceed via desorption of a carbon dimer [35]. Thus we also calculate the formation energy ΔE_{C_2} of the divacancy defects using a dissociated state consisting of C_2 and the defective CNT:

$$\Delta E_{C_2} = |E_{pristine} - (E_{defect} + E_{C_2})|. \tag{7.8}$$

While the formation energies of the divacancy defects can be directly compared, comparison of the relative stabilities of the monovacancy and divacancy defects requires an additional step. The formation energy of a single divacancy with respect to two independent monovacancies (Δ) is thus calculated:

$$\Delta = |\Delta E_{divacancy} - 2\Delta E_{monovacancy}|. \tag{7.9}$$

Finally, the difference in the formation energies of the 585 defects ($d\Delta$) is calculated. The formations energies and relative stabilities of the defects are given in

Tables 7.1 and 7.2 for the zig-zag and armchair defects respectively. Information on defect energetics in graphene is included in Table 7.1 for comparison.

Table 7.1: Formation energies of defects in zig-zag CNTs and graphene in eV.

	(10,0)	(20,0)	(30,0)	Graphene
ΔE_{mv} (eV)	18.22	18.98	22.98	25.80
$\Delta E_{ldv,C}$ (eV)	27.58	28.99	36.79	39.83
$\Delta E_{ldv,C_2}$ (eV)	17.60	19.02	26.82	29.86
$\Delta E_{vdv,C}$ (eV)	32.27	32.66	38.36	39.82
$\Delta E_{vdv,C_2}$ (eV)	22.29	22.69	28.38	29.85
ΔE_{555777} (eV)	-	-	-	39.49
$\Delta E_{555777,C_2}$ (eV)	-	-	-	29.51
$\Delta_{ldv,C}$ (eV)	8.85	8.98	9.15	11.78
Δ_{ldv,C_2} (eV)	18.83	18.95	19.13	21.74
$\Delta_{vdv,C}$ (eV)	4.17	5.31	7.59	11.77
Δ_{vdv,C_2} (eV)	14.14	15.28	17.57	21.75
$d\Delta$ (eV)	4.69	3.67	1.56	0.01

Table 7.2: Formation energies of defects in armchair CNTs in eV. Literature values taken from Biel *et al* [18].

	(5,5)	(7,7)	(10,10)	(20,20)	(30,30)
ΔE_{mv} (eV)	17.94	17.99	19.75	20.82	24.39
$\Delta E_{ldv,C}$ (eV)	27.52	30.00	30.85	31.40	37.84
$\Delta E_{ldv,C_2}$ (eV)	17.54	20.03	20.87	21.43	27.86
$\Delta E_{vdv,C}$ (eV)	31.49	33.16	33.22	33.47	39.73
$\Delta E_{vdv,C_2}$ (eV)	21.52	23.19	23.25	23.49	29.75
$\Delta E_{555777,C}$ (eV)	34.10	34.19	34.50	35.02	36.17
$\Delta E_{555777,C_2}$ (eV)	24.12	24.21	24.53	25.04	26.20
$\Delta_{ldv,C}$ (eV)	8.36	5.97	8.65	10.24	10.95
Δ_{ldv,C_2} (eV)	18.33	15.97	18.62	20.22	20.92
$\Delta_{vdv,C}$ (eV)	4.39	2.81	6.27	8.18	9.06
Δ_{vdv,C_2} (eV)	14.36	12.79	16.24	18.15	19.03
$d\Delta$ (eV)	3.97	3.16	2.38	2.06	1.89
Literature $\Delta_{ldv,C}$ (eV)	6.5	6.7	6.7	-	-
Literature $\Delta_{vdv,C}$ (eV)	4.3	4.8	4.2	-	-

The formation energies of lateral divacancies are smaller than that of vertical divacancies for both the zig-zag and armchair CNTs. This difference in relative stabilities of the 585 defects results from shortening of bonds perpendicular to the CNT axis, which is better accommodated by local diameter reduction in

the case of the lateral divacancy. This is particularly evident in the length of the bridgehead bond - the bond is shorter in the lateral divacancy than in the vertical and also the 585 defect in graphene. Both 585 defects are more stable than two isolated monovacancies *i.e.* $\Delta E_{ldv} < \Delta E_{vdv} < 2\Delta E_{mv}$. This result is consistent with previous reports for low diameter CNTs [17, 18]. For the (5,5)-CNT we find the lateral divacancy to be more stable by approximately 4 eV ($d\Delta$ in Table 7.2), which is in good agreement with the value 3.5 eV reported in the literature by Amorim *et al* [17]. The $d\Delta$ value can also be calculated from the work of Biel and co-workers [18] with the required values are reproduced in Table 7.2 and a value of 2.2 eV obtained, which is lower than values obtained by us and also Amorim *et al*. As the CNT diameter increases, the difference in $d\Delta$ is reduced, this reduction in $d\Delta$ was anticipated given the two 585 defects are identical in graphene and CNT curvature reduces with diameter. Such a trend in $d\Delta$ values does not appear in Biel's work, however the CNT size at which the lateral and vertical 585-divacancies become energetically indistinguishable is larger than those considered by their study.

The formation of the 555777 defect is found to be more favourable than the 585 defect in graphene, as already reported in the literature. Amorim *et al* [17] have reported the 555777 defects become more stable than the 585 defects for (30,30) armchair CNTs and (117,0) zigzag CNTs. However, these results were obtained from molecular mechanics calculations. Using *ab initio* DFT, we confirm that the 555777 defect is indeed more stable than the 585 defect in the (30,30)-CNT, while the 585 defect is found to be more stable for the smaller diameter armchair CNTs.

7.5 Electronic Transport Properties

The transmission spectra for the large diameter zigzag and armchair CNTs are shown in Figures 7.5 and 7.6. The introduction of vacancy defects does not affect the size of the CNT band gap in the semi-conducting CNTs studied and does not open up a band gap in the metallic CNTs. In all cases as anticipated, the introduction of a defect results in a reduction in transmission relative to the pristine, defect-free CNT. The monovacancy and 585-divacancies exhibit a similar suppression of transmission, while a more marked reduction in transmission occurs for the 555777 divacancy defect. In particular, the transmission spectra for the 555777 defect shows a trough where transmission drops to 0.1 close to the Fermi level at -0.15 eV and -0.11 eV for the (20,20) and (30,30) CNTs, respectively.

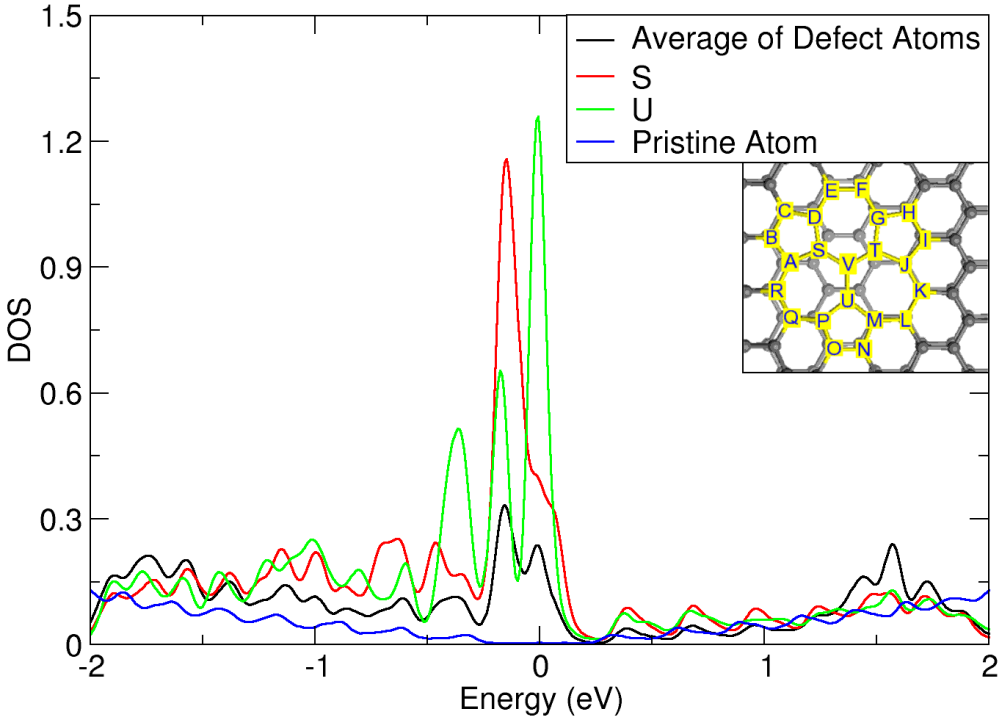


Figure 7.4: Average LDOS in 555777 defect, and LDOS of atoms S and U compared to LDOS of defect free CNT for the (30,30)-CNT. Inset: Labels of the defect atoms. Note that atoms S and T are equivalent by symmetry and therefore have the same LDOS.

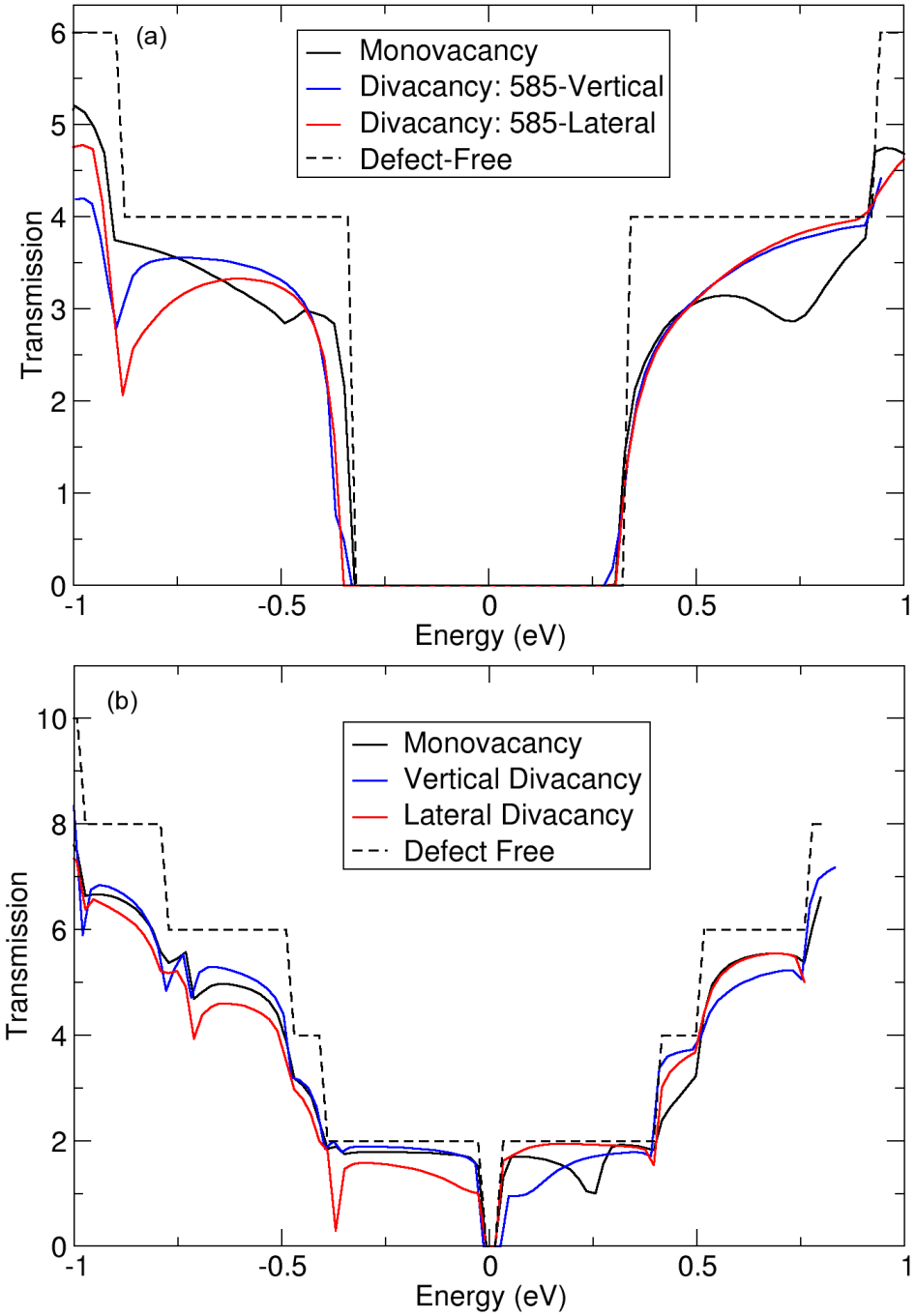


Figure 7.5: Transmission spectra for the (20,0)-CNT (a) and (30,0)-CNT (b). The monovacancy and both the divacancy defects reduce transmission by a similar amount compared to the pristine, defect free CNT.

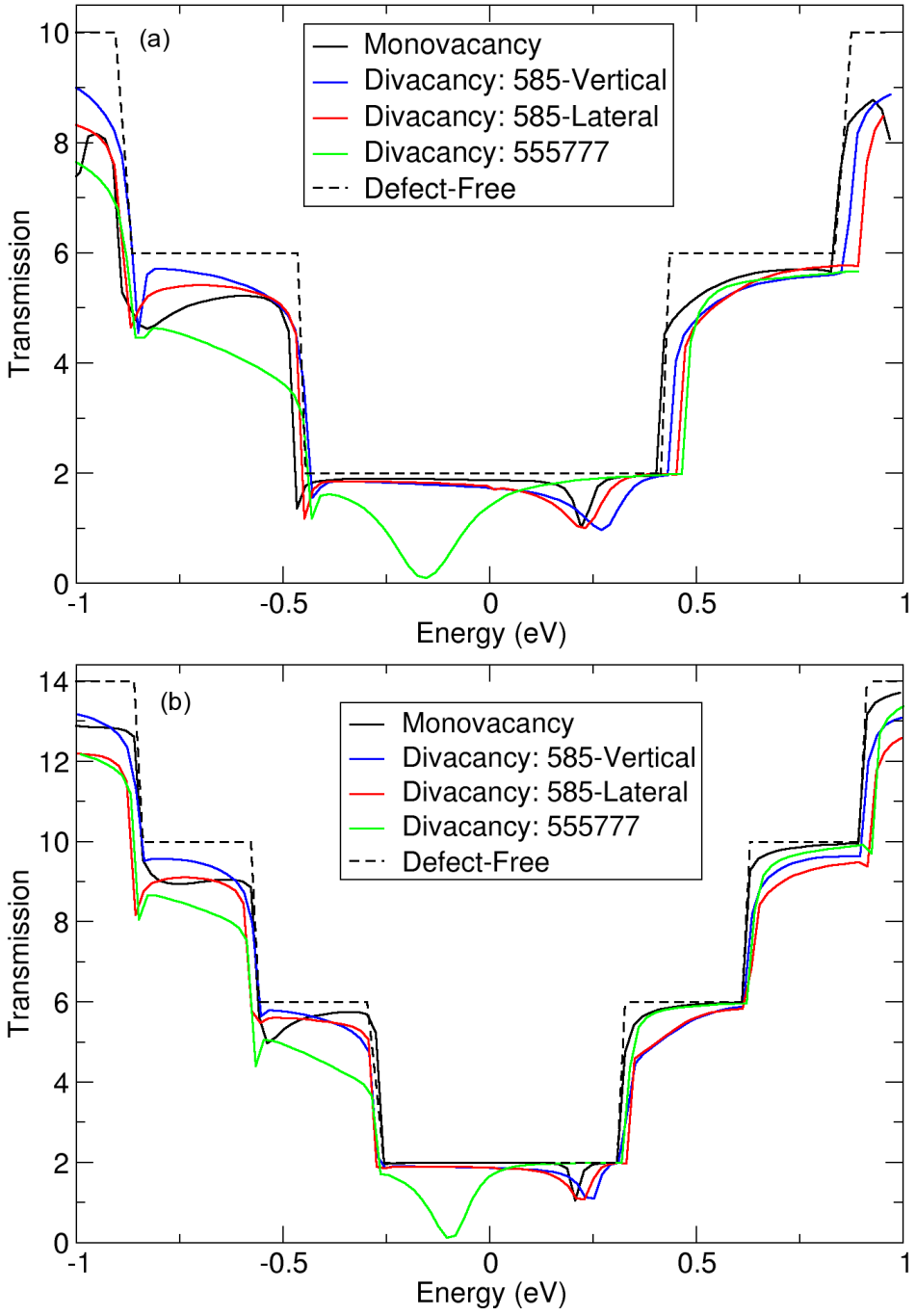


Figure 7.6: Transmission spectra for the (20,20)-CNT (a) and (30,30)-CNT (b). Similar transmissions are obtained for the monovacancy and 585-divacancies. The 555777 defect results in a more marked reduction in transmission relative to the pristine CNT than the monovacancy and 585 divacancies.

This pronounced dip in transmission on the introduction of a 555777 defect has a number of important consequences. The first implication is that localised electronic states are formed at the 555777 defect; such localised states should be observable experimentally making it possible to distinguish 555777 defects from other vacancy defects. The local density of states (LDOS) of atoms in the 555777 defect show that a peak in DOS occurs at the same energy as the dip in transmission; see Figure 7.4 for the (30,30)-CNT. These states are localised on atoms S, T and U close to the centre of the defect, for which there is a substantial increase in DOS close to the Fermi level relative to both the average of the defect atoms and a carbon atom in a pristine (30,30)-CNT. In addition, the substantial scattering from the 555777 defect needs to be considered when using large diameter CNTs in applications, since this defect becomes more stable than the 585 defects in such CNTs. Large diameter CNTs in particular are being considered as a replacement for copper interconnects because at large diameters the band gaps of even ostensibly semi-conducting CNTs become vanishingly small [36].

A zone-folding picture of CNT electronic properties predicts that the (30,0)-CNT is metallic because $\frac{(n-m)}{3}$ is an integer. As can be seen in the transmission results in Figure 7.5, a small band gap of $\sim$30 meV opens up for all (30,0)-CNTs we study. Most likely this is because the simple zone-folding picture does not take account of the CNT curvature and resultant π-σ hybridisation [37–40]. This finite gap in the (30,0)-CNT was found by us to persist in plane waves calculations using Quantum Espresso [41], confirming that this gap is not caused by the small basis set size used in our transport studies.

As a starting point, the independent scattering approximation (ISA), described in Section 7.2.3 is used to estimate mean free path λ. This approximation results in a linear relationship between λ and the separation between defects l_d, as given by Equation 7.5. This relationship between λ and l_d is plotted in Figure

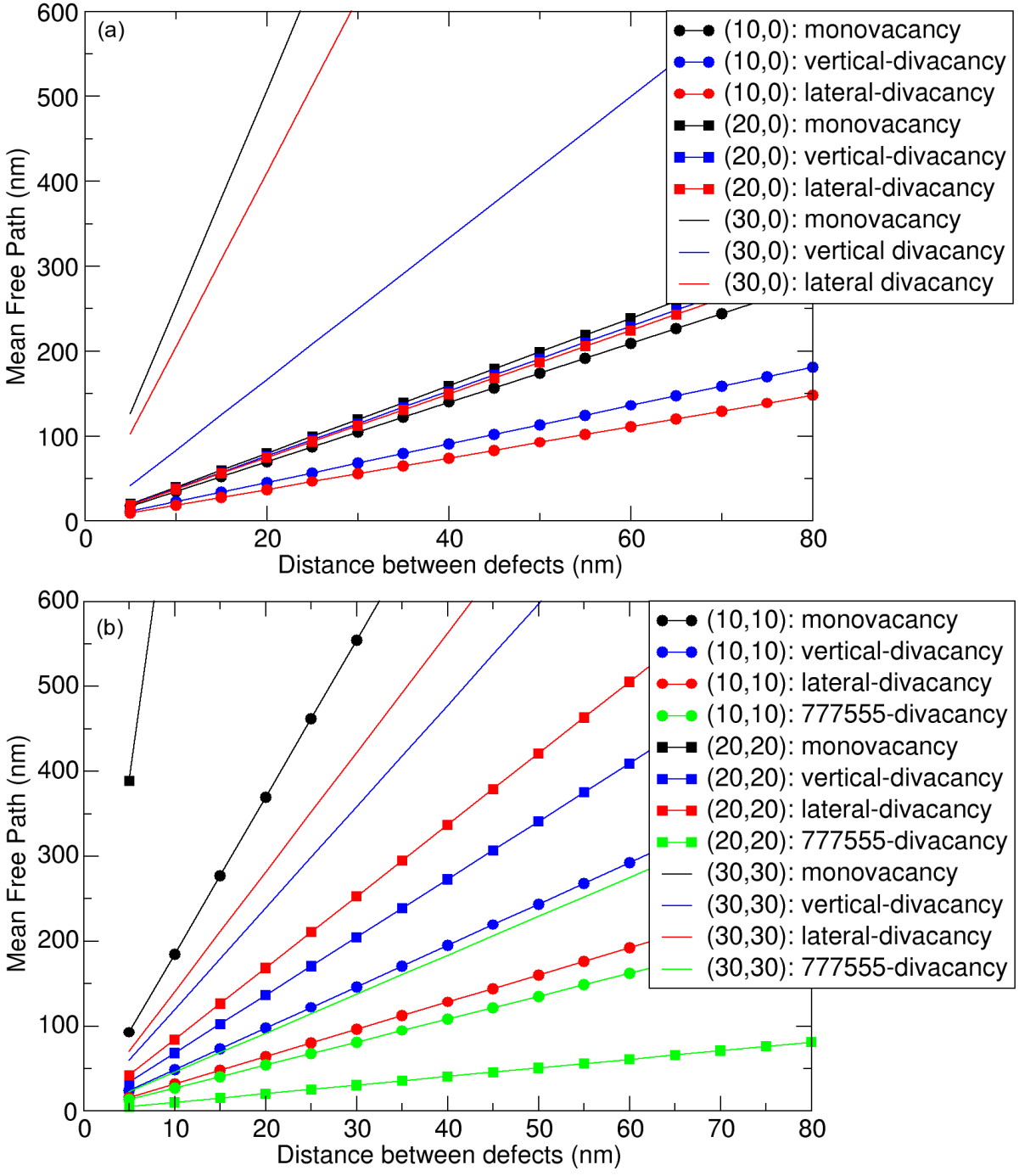


Figure 7.7: The mean free path as a function of defect separation for zigzag (a) and armchair (b) CNTs.

7.7 for the armchair and zigzag CNTs. Beenakker [31] has previously shown that the localisation length ξ in quasi-one-dimensional systems can be approximated by:

$$\xi = (N_{ch} + 1)\lambda = (N_{ch} + 1)\left(\frac{R_c}{R_s}\right) l_d. \tag{7.10}$$

Using more elaborate approaches which account for the interference effects which result from scattering between defects has also resulted in a linear relationship between ξ and l_d [13, 42]. The calculated values of $(N_{ch} + 1)\lambda$ for each defect in the CNTs studied are given in Table 7.3.

Table 7.3: Proportionality constant between localisation length ξ and the distance between defects l_d in the relation $\xi = const$ x l_d

	$(N_{ch} + 1)^{R_C}/_{R_S}$			
	mv	vdv	ldv	555777
(10,0)	10.44	6.79	5.54	-
(20,0)	19.88	19.10	18.69	-
(30,0)	75.97	24.96	61.49	-
(5,5)	9.03	3.11	3.40	1.88
(7,7)	24.44	4.27	6.78	3.41
(10,10)	55.42	14.61	9.61	8.10
(20,20)	388.70	34.09	42.10	5.07
(30,30)	9995	70.30	59.68	22.90

The ratio of ξ to l_d has been reported in the literature from theory as 5.2, 6.4 and 8.4 for the lateral divacancy in the (5,5), (7,7) and (10,10) CNTs respectively [13], while experimental values of 5.1 and 4.1 have been reported respectively for the (5,5) and (10,10) CNTs, again for the lateral divacancy [13, 42]. We obtain values of 3.4, 6.8 and 9.6 for the value of ξ for the lateral divacancies in (5,5), (7,7) and (10,10) CNTs. These results are in reasonable agreement with the literature results and justify our use of the ISA, furthermore interference effects between defects are expected to be less important in larger diameter CNTs with similar defect concentrations. Use of the ISA enables analysis of λ to be extended to larger diameter CNTs than have been previously studied.

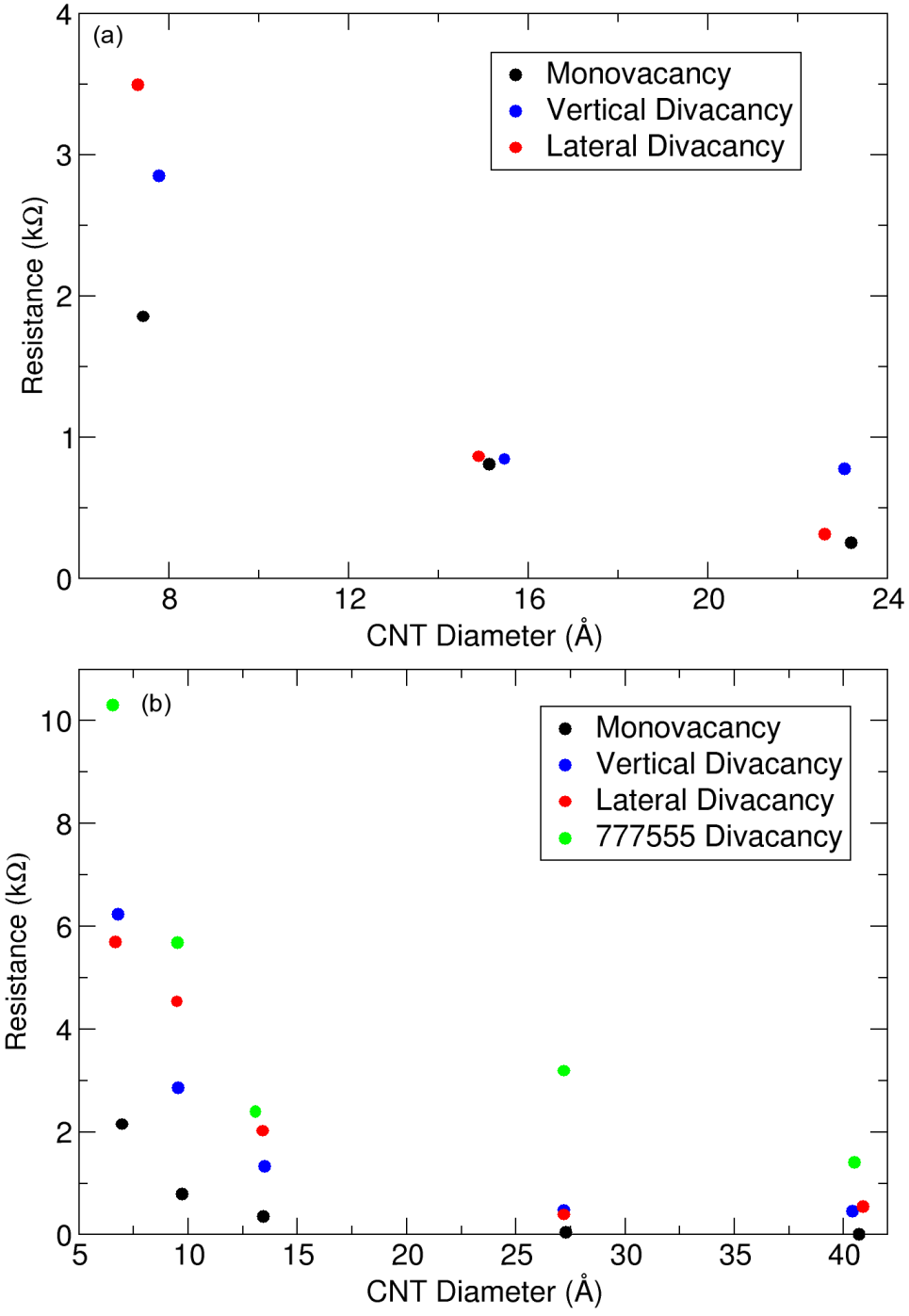


Figure 7.8: The defect resistance as a function of CNT diameter for zigzag (a) and armchair (b) CNTs.

As can be seen in Figure 7.7, as CNT tube diameter increases, mean free path extends significantly at fixed defect separations. We attribute this effect to diminished defect scattering resistance as relatively, the defect takes up a smaller proportion of the CNT side wall as tube diameter increases. The effect of monovacancies and divacancies on scattering depends on the electronic properties of the CNTs. Monovacancies have a much smaller impact on λ in metallic CNTs than divacancies, while a similar effect is seen for both monovacancies and divacancies in semi-conducting CNTs. This result is consistent with reports that monovacancies show little scattering at the Fermi level [12, 18]. The 555777 defect has the greatest impact on the mean free path for all the armchair CNTs, which is expected given the greater depression of transmission and the formation of localised states close the the Fermi level. Figure 7.8 shows the resistance of each defect as a function of CNT diameter.

As CNT diameter increases, the defect resistance decreases in almost all cases (the notable outlier is the 555777 defect in (20,20), which is larger than in (10,10)). In addition, the differences between the resistances of the monovacancy and divacancy defects for a specific diameter also decreases for larger CNTs, this is particularly evident for zigzag CNTs, which already for the (20,0) CNT has almost identical resistances for all the defects. For the armchair CNTs, the largest defect resistance occurs in all cases for the 555777 defect which is expected given the results already discussed and even at 40 Å diameter, is significantly larger than the 585 divacancy defects.

7.6 Conclusion

It is confirmed that the 585 lateral divacancy defect is more stable than the 585 vertical divacancy and the monovacancy defect in armchair and zigzag CNTs. In addition, the 555777 defect is found from first principles calculations to be-

come more stable than both 585 defect at an armchair CNT diameter of 40 Å. The independent scattering approximation has been validated by comparison to experimental results and transport calculations which used a more rigorous scattering formalism. Adoption of the independent scattering approximation has enabled localisation length to be studied in large diameter CNTs. The localisation length increases with CNT diameter, however strong scattering is observed from the 555777 defect configuration, which may have implications for the use of large diameter CNTs in electronic applications.

7.7 References

[1] P. Avouris, Z.H. Chen, and V. Perebeinos. Carbon-Based Electronics. *Nature Nanotechnology*, 2:605–615, 2007.

[2] G.F. Close, S. Yasuda, B. Paul, S. Fujita, and H.S.P. Wong. A 1 GHz Integrated Circuit with Carbon Nanotube Interconnects and Silicon Transistors. *Nano Letters*, 8:706–709, 2008.

[3] F. Kreupl, A.P. Graham, G.S. Duesburg, W. Steinhögl, M. Liebau, E. Unger, and W. Hönlein. Carbon Nanotubes in Interconnect Applications. *Microelectronic Engineering*, 64:399–408, 2002.

[4] Y. Fan, B.R. Goldsmith, and P.G. Collins. Identifying and Counting Point Defects in Carbon Nanotubes. *Nature Materials*, 4:906–911, 2005.

[5] L. Valentini, F. Mercuri, I. Armentano, C. Cantalini, S. Picozzi, L. Lozzi, S. Santucci, A. Sgamellotti, and J.M. Kenny. Role of Defects on the Gas Sensing Properties of Carbon Nanotube Thin Films: Experiment and Theory. *Chemical Physics Letters*, 367:356–361, 2004.

[6] Z. Zanolli and J.C. Charlier. Defective Carbon Nanotubes for Single-Molecule Sensing. *Physical Review B*, 80:155447, 2009.

[7] J. Kong, N.R. Franklin, C. Zhou, M.G. Chapline, S. Peng, K. Cho, and H. Dai. Nanotube Molecular Wires as Chemical Sensors. *Science*, 287:622–625, 2000.

[8] M. Sammalkorpi, A. Krasheninnikov, A. Kuronen, L. Nordlund, and K Kaski. Mechanical Properties of Carbon Nanotubes with Vacancies and Related Defects. *Physical Review B*, 70:245416, 2004.

[9] A. Kis, G. Csányi, J.-P. Salvelet, T.-N. Lee, E. Couteau, A.J. Kulik, W. Benoit, J. Brugger, and L. Forró. Reinforcement of Single-Walled Carbon Nanotube Bundles by Intertube Bridging. *Nature Materials*, 3:153–157, 2004.

[10] S. Zhang, S.L. Mielke, R. Khare, D. Troya, R.S. Ruoff, G.C. Schatz, and T. Belytschko. Mechanics of Defects in Carbon Nanotubes: Atomistic and Multiscale Simulations. *Physical Review B*, 71:115403, 2005.

[11] J.C. Charlier. Defects in Carbon Nanotubes. *Accounts of Chemical Research*, 35:1063–1069, 2002.

[12] B. Biel, F.J. Garcia-Vidal, A. Rubio, and F. Flores. Anderson Localization in Carbon Nanotubes: Defect Density and Temperature Effects. *Physical Review Letters*, 95:266801, 2005.

[13] F. Flores, B. Biel, A. Rubio, F.J. Garcia-Vidal, C. Gomez-Navarro, P. de Pablo, and J. Gomez-Herrero. Anderson Localization Regime in Carbon Nanotubes: Size Dependent Properties. *Journal of Physics-Condensed Matter*, 20:304211, 2008.

[14] C.W. Marquardt, S. Dehm, A. Vihayaraghavan, S. Blatt, F. Hennrich, and R. Krupke. Reversible Metal-Insulator Transitions in Metallic Single-Walled Carbon Nanotubes. *Nano Letters*, 8:2767–2772, 2008.

[15] A.V. Krasheninnikov, K. Nordlund, and J. Keinonen. Production of Defects in Supported Carbon Nanotubes under Ion Irradiation. *Physical Review B*, 65:165423, 2002.

[16] H. Zeng, J.-P. Leburton, H. Hu, and J. Wei. Vacancy Cluster-Limited Electronic Transport in Metallic Carbon Nanotubes. *Solid State Communications*, 151:9–12, 2011.

[17] R.G. Amorim, A. Fazzio, A. Antonelli, F.D. Novaes, and A.J.R. da Silva. Divacancies in Graphene and Carbon Nanotubes. *Nano Letters*, 7:2459–2462, 2007.

[18] B. Biel, F.J. Garcia-Vidal, A. Rubio, and F. Flores. *Ab initio* Study of Transport Properties in Defected Carbon Nanotubes: An O(N) Approach. *Journal of Physics-Condensed Matter*, 20:294214, 2008.

[19] A.V. Krasheninnikov, P.O. Lehtinen, A.S. Foster, and R.M. Nieminen. Bending the rules: Contrasting vacancy energetics and migration in graphite and carbon nanotubes. *Chemical Physics Letters*, 418:132 – 136, 2006.

[20] S . Berber and A. Oshiyama. Atomic and Electronic Structures of Divacancies in Carbon Nanotubes. *Physical Review B*, 77:165405, 2008.

[21] J.C. Meyer, C. Kisielowski, R. Erni, M.D. Rossell, M.F. Crommie, and A. Zettl. Direct Imaging of Lattice Atoms and Topological Defects in Graphene Membranes. *Nano Letters*, 8:3582–3586, 2008.

[22] G.-D. Lee, C.Z. Wang, E. Yoon, N.-M. Hwang, D.-Y. Kim, and K.M. Ho. Diffusion, Coalescence, and Reconstruction of Vacancy Defects in Graphene Layers. *Physical Review Letters*, 95:205501, 2005.

[23] www.openmx-square org.

[24] D.M. Ceperley and B.J. Alder. Ground State of the Electron Gas by a Stochastic Method. *Physical Review Letters*, 45:566–569, 1980.

[25] T. Ozaki and H. Kino. Numerical Atomic Basis Orbitals from H to Kr. *Physical Review B*, 69:195113, 2004.

[26] I. Morrison, D.M. Bylander, and L. Kleinman. Non-Local Hermitian Norm-Conserving Vanderbilt Pseudopotenial. *Physical Review B*, 47:6728–6731, 1993.

[27] H.J. Monkhorst and J.D. Pack. Special Points for Brillouin Zone Integrations. *Physical Review B*, 13:5188–5192, 1976.

[28] R. Gutierrez, G. Fagas, G. Cuniberti, F. Grossmann, R. Schmidt, and K. Richter. Theory of an All-Carbon Molecular Switch. *Physical Review B*, 65:113410, 2002.

[29] R. Gutierrez, G. Fagas, K. Richter, F. Grossmann, and R. Schmidt. Conductance of a Molecular Junction mediated by unconventional Metal-Induced Gap States. *Europhysics Letters*, 62:90–96, 2003.

[30] G. Fagas and J.C. Greer. Ballistic Conductance in Oxidised Si Nanowires. *Nano Letters*, 9:1856–1860, 2009.

[31] C.W.J Beenakker. Random Matrix Theory of Quantum Transport. *Reviews of Modern Physics*, 69:731–808, 1997.

[32] M. Ohfuchi, T. Ozaki, and C. Kaneta. Large-Scale Electronic Transport Calculations of Finite-Length Carbon Nanotubes Bridged between Graphene Electrodes with Lithium-Intercalated Contacts. *Applied Physics Express*, 4:095101, 2011.

[33] T. Markussen, R. Rurali, A.-P. Jauho, and M. Brandbyge. Scaling Theory Put into Practice: First-Principles Modeling of Transport in Doped Silicon Nanowires. *Physical Review Letters*, 99:076803, 2007.

[34] J. Kotakoski, A.V. Krasheninnikov, and K. Nordlund. Energetics, Structure, and Long-Range Interaction of Vacancy-Type Defects in Carbon Nanotubes: Atomistic Simulations. *Physical Review B*, 74:245420, 2006.

[35] K.R. Lykke and P. Wurz. Direct Detection of Neutral Products from Photodissociated C_{60}. *Journal of Physical Chemistry*, 98:3191, 1992.

[36] Y. Chai, Z. Xiao, and P.C.H. Chan. Horizontally Aligned Carbon Nanotube Bundles for Interconnect Application: Diameter-Dependent Contact Resistance and Mean Free Path. *Nanotechnology*, 21:235705, 2012.

[37] X. Blase, L.X. Benedict, E.L. Shirley, and S.G. Louie. Hybridization Effects and Metallicity in Small Radius Carbon Nanotubes. *Physical Review Letters*, 72:1878–1881, 1994.

[38] O. Gülseren, T. Yildirim, and S. Ciraci. Systematic *ab initio* Study of Curvature Effects in Carbon Nanotubes. *Physical Review B*, 65:153405, 2002.

[39] V. Zólyomi and J. Kürti. First-Principles Calculations for the Electronic Band Structures of Small Diameter Single-Wall Carbon Nanotubes. *Physical Review B*, 70:085403, 2004.

[40] X. Lu and Z. Chen. Curved Pi-Conjugation, Aromaticity, and the Related Chemistry of Small Fullerenes ($<C_{60}$) and Single-Walled Carbon Nanotubes. *Chemical Reviews*, 105:3643–3696, 2005.

[41] P. Giannzonni, S. Baroni, N. Bonini, M. Calandra, P. Car, D. Cavazzoni, C.Ceresoli, G. L. Chiarotti, M. Cococcioni, I. Dabo, S. Dal Corso, A.and de Gironcoli, S. Fabris, R. Fratesi, G.Gebauer, U. Gerstmann, C. Gougoussis, A. Kokalj, M. Lazzeri, L. Martin-Samos, N. Marzari, F. Mauri, R. Mazzarello, S. Paolini, A. Pasquarello, L. Paulatto, C. Sbraccia, S. Scandolo, G. Sclauzero, A.P. Seitsonen, A. Smogunov, P. Umari, and R. M. Wentzcovitch. QUANTUM ESPRESSO: A Modular and Open-Source Software Project for Quantum Simulations of Materials. *Journal of Physics-Condensed Matter*, 21:395502, 2009.

[42] G. Gómez-Navarro, P.J. de Pablo, J. Gómez-Herrero, B. Biel, F.J. Garcia-Vidal, A. Rubio, and F. Flores. Tuning the Conductance of Single-Walled Carbon Nanotubes by Ion Irradiation in the Anderson Localization Regime. *Nature Materials*, 4:534–539, 2005.

Chapter 8

Conclusion

In Chapter 4 the reasons behind the characteristic defective structure of N-doped CNTs were explained through the results of our DFT calculations, the experimental work of our collaborators and consideration of *in situ* TEM studies. The nitrogen-cobalt bond was found to be stronger than the carbon-cobalt bond through DFT calculations and it is this difference in binding strength at the nanoparticle catalyst that leads to the formation of bamboo CNTs. The CVD growth of CNTs follows a three stage process, as has been observed in *in situ* TEM studies [1, 2]. First, the carbon source is cracked by the nanoparticle catalyst, where it deposits forming a graphitic flake. Next as carbon is continuously deposited at the flake the catalyst particle elongates until its surface energy is larger than its stabilisation due to interaction with the growing CNT sidewalls at which point it contracts to a more spherical shape. Finally, further carbon is added to the CNT growth edge, increasing the CNT length and forming a hollow CNT. In the case of nitrogen doped CNTs, this last growth stage is not attained and instead the first and second stages repeat continuously because the stronger nitrogen-cobalt bond results in repeated elongation of the catalyst particle.

Chapter 5 is concerned with the IV characteristics of contacts between Al and CNTs. Contacting the (16,0) CNT to Al results in shifting of the Fermi energy towards the CNT conduction band edge, resulting in an asymmetric IV curve. No

current occurs at low biases because of the CNT band gap. Boron and nitrogen dopants make the semi-conducting (16,0)-CNT metallic and these doped CNTs form Ohmic contacts with Al, however the dopant atoms behave as defects in the CNT structure which results in significant scattering and non-linear IV at larger bias voltages. While this result suggests that substitutional doped CNTs may be suited to generating reliably metallic CNTs which form Ohmic contacts with metal, the scattering at larger bias is problematic as it negates one of the primary advantages of CNTs for electronic applications *i.e.* ballistic transport. As a result, we consider the endohedral dopant TTF, which dopes the CNT without affecting the CNT sidewall structure and find it to alter the position of the Fermi energy without significant scattering.

Chapter 6 also considers metal-CNT interfaces, in this case the interface between Fe and (10,0)-CNT and the focus of the research is shifted to study of the effect of interfacial structure on electronic properties. Two interface structures are studied, in the first structure there is a raised metal dock, the tip of which is inside hollow CNT while the second structure presents a flat Fe surface for the contact. Neither the CNT band gap nor the position of the Fermi energy is sensitive to the structure, however the exact structure of Fe at the interface does effect the transmission, with a larger transmission occurring for the interface with the dock. Additionally, we study a boron doped CNT in contact with Fe, as in the work of the previous chapter, the CNT becomes metallic and an Ohmic contact is formed.

Finally, in Chapter 7 vacancy defects are studied in CNTs for a range of chiralities. The order of stability of vacancy defects in small diameter CNTs is confirmed to occur as previously reported in the literature *i.e.* divacancies are more stable than two isolated monovacancies and the 585-divacancy is more stable than the 555777 divacancy [3, 4]. We extend this work to larger diamater CNTs and from first principles confirm that the 555777 defect becomes more stable than the 585

defects for the (30,30)-CNT, as predicted by molecular mechanics calculations [3]. All defects cause electron scattering, with the most severe scattering occurring for the 555777 defect near the Fermi energy, which is due to highly localised states in this defect. Use of large diameter CNTs in electronics applications (*e.g.* interconnects) would have to consider this affect, as it is in precisely such CNTs that this defect is stable. The independent scattering approximation is successfully validated with reference to more rigorous approaches for small diameter CNTs and thus we can calculate mean free path in larger CNTs than have previously been considered. Mean free path extends with CNT diameter for fixed defect separation and shortest mean free paths occur for the 555777 defect.

This thesis has shown that substitutional doped zigzag CNTs become metallic at dopant concentrations as low as 1 at. % and form Ohmic contacts with Al and Fe metal. Potentially, substitutional doping of CNTs may offer a path to reliably Ohmic metal-CNT contacts; further research into armchair, chiral and metallic zigzag CNTs is needed to confirm that substitutionally doped CNTs in general form Ohmic contacts. Additionally, further work is needed to explore the properties of interfaces using other endohedral dopants, particularly p-type dopants such as tetracyano-p-quinodimethane (TCNQ). The interfacial structure of the metal-CNT end contact is found to affect transmission and therefore is expected to impact on IV characteristics, future work could consider additional interface structures to expand our understanding of the relationship between contact structure and electronic properties.

8.1 References

[1] S. Helveg, C. López-Cartes, J. Sehested, P.L. Hansen, B.S. Clausen, J.R. Rostrup-Nielsen, A. Abild-Pedersen, and J.K. Nørskov. Atomic-scale imaging of Carbon Nanofibre Growth. *Nature*, 427:426–429, 2004.

[2] S. Hofmann, R. Sharma, C. Ducati, G. Du, C. Mattevi, C. Cepek, M. Cantoro, S. Pisana, A. Parvez, F. Cervantes-Sodi, A.C. Ferrari, R. Dunin-Borkowski, S. Lizzit, L. Petaccia, A. Goldoni, and J. Robertson. *In situ* Observations of Catalyst Dynamics during Surface-Bound Carbon Nanotube Nucleation. *Nano Letters*, 7:602–608, 2007.

[3] R.G. Amorim, A. Fazzio, A. Antonelli, F.D. Novaes, and A.J.R. da Silva. Divacancies in Graphene and Carbon Nanotubes. *Nano Letters*, 7:2459–2462, 2007.

[4] B. Biel, F.J. Garcia-Vidal, A. Rubio, and F. Flores. *Ab initio* Study of Transport Properties in Defected Carbon Nanotubes: An O(N) Approach. *Journal of Physics-Condensed Matter*, 20:294214, 2008.

Appendix A

A.1 Acronyms

AO - Atomic Orbital
BCNT - Bamboo Carbon Nanotube
CG - Conjugate Gradient
CMOS - Complementary Metal Oxide Semiconductor
CNT - Carbon Nanotube
(C)CVD - (Catalytic) Chemical Vapour Deposition
DFT - Density Functional Theory
DOS - Density of States
DFTB - Density Functional Tight Binding
EA - Electron Affinity
ELF - Electron Localisation Function
FET - Field Effect Transistor
GEA - Generalised Expansion Approximation
GGA - Generalised Gradient Approximation
GTO - Gaussian Type Orbital
HOMO - Highest Occupied Molecular Orbital
IE - Ionisation Energy
ISA - Independent Scattering Approximation
IV - Current-Voltage
KS - Kohn-Sham
LDA - Linear Density Approximation
LDOS - Local Density of States
ldv - Lateral Divacancy
LUMO - Lowest Unoccupied Molecular Orbital
MD - Molecular Dynamics
MFP - Mean Free Path
MIGS - Metal Induced Gap States
mv - Monovacancy

MWNT - Multi-Walled Carbon Nanotube
NEGF - Non-Equilibrium Green's Function
NR - Newton-Raphson
NT - Nanotube
NW - Nanowire
PES - Potential Energy Surface
PAW - Projector Augmented Wave
PAO - Pseudo Atomic Orbital
PP - Pseudopotential
SCF - Self Consistent Field
SD - Steepest Descent
STO - Slater Type Orbital
SWNT - Single-Walled Carbon Nanotube
TBMC - Tight Binding Monte Carlo
TCNQ - Tetracyano-p-quinodimethane
(HR)TEM - (High Resolution) Transmission Electron Microscopy
TIM - Thermal Interface Material
TTF - Tetrathiafulvalene
vdv - Vertical Divacancy
VLS - Vapour-Liquid-Solid